UNICA

UNIVERSITÀ
DEGLI STUDI
DI CAGLIARI

Ph.D. DEGREE IN
Earth and Environmental Sciences and Technologies
Cycle XXXVIII

TITLE OF THE Ph.D. THESIS

High-frequency Quaternary climate changes: a key to understanding present and future coastal scenarios

Scientific Disciplinary Sector(s)

GEO/02

Ph.D. Student: Giovanni Fantini

Supervisor Maria Teresa Melis

Co-Supervisor Stefano Andreucci

Final exam. Academic Year 2024/2025
Thesis defence session: July 2026

TABLE OF CONTENTS

Introduction

Scientific background, knowledge gaps, and research aims

Throughout geological time, the Earth system and its climate have undergone continuous changes. The onset of the Quaternary, at 2.58 Ma, coincides with a major reorganization of Earth's climate, marked by the intensification of Northern Hemisphere glaciation and increasingly pronounced glacial–interglacial variability (e.g., Gibbard et al., 2009). These climatic variations depend on the solar radiation flux, which varies cyclically, paced mainly by Earth's orbital-forced parameters (eccentricity, obliquity, and precession) with periodicities of approximately 100, 40, and 20 kyr (Milankovitch cycles). Alternating warm (interglacial) and cold (glacial) periods, identified from variations in oxygen isotope ratios ($^{18}O/^{16}O$) in marine sediments that reflect changes in global ice volume and ocean temperature, are grouped into the Marine Isotopic Stage (MIS) stratigraphy. Moreover, coastlines reached about 120–140 m below present sea level during the glacial periods, whereas during warmer interglacials were within 10 m above present sea level (e.g., Waelbroeck et al., 2002; Lisiecki and Raymo, 2005; Grant et al., 2014).

One of the major consequences of these glacial-interglacial alternations has been the growth and decay of ice sheets, resulting in fluctuations in oceans and marginal sea levels (e.g. Mediterranean basin), accompanied by isostatic adjustment of the Earth's crust. In addition to controlling coastline positions, sea-level fluctuations have strongly influenced weathering rates, the stability of coastal plains, river incision, sediment by-pass and deposition, as well as wind, wave, tide, and current-driven processes along coastlines. These have affected sediment erosion, production and transport, thereby driving the evolution of depositional environments through time and space (Masselink & Gehrels, 2015).

Coastal sedimentary sequences and biogenic structures represent key archives of sea-level fluctuations and associated environmental changes. However, their architecture, composition, and preservation are themselves strongly influenced by these same processes (Camoin and Webster, 2015). Therefore, integrated sedimentological and stratigraphic analysis of coastal deposits, ultimately reveals their evolution in response to climate change and sea level fluctuation. Moreover, detailed stratigraphic correlations supported by a robust chronological control, based on radiocarbon, U/Th, AAR, and luminescence dating methods, provide new insights into the timing and amplitude of Late Quaternary sea-level changes across a wide range of temporal scales, from hundreds of thousands of years to centuries. Despite sea-level fluctuation and coastal response being relatively well defined at the Milankovitch frequencies (100, 40, and 20 kyr) this, at millennial- to centennial-timescales remain much less constrained, both in terms of timing and magnitude. This gap limits our understanding of how coastal systems respond to high-frequency climate variability, which is particularly relevant given that these timescales are comparable to those of ongoing human-driven climate change.

Ongoing global warming is significantly impacting natural and human systems worldwide. Greenhouse gas concentrations continue to increase at an unprecedented rate in historical record, driven largely by unsustainable energy use, land-use change, and widespread production and consumption patterns across regions and countries (IPCC, 2023). As a consequence, processes associated with global warming, together with ocean acidification and related stressors, are driving profound long-term alterations of coastal systems and ocean circulation, leading to substantial biodiversity loss in coastal environments. In this scenario, improving our understanding of the processes governing the interaction between climate change and coastal evolution is increasingly critical.

Sardinia island represents an ideal site for this research, as its central Mediterranean setting exposes its coastlines to intense wind and wave regimes. Combined with its geological and geomorphological heterogeneity, this results in a wide variety of coastal depositional environments and sedimentary archives.

This thesis investigates three distinct Pleistocene-Holocene coastal sedimentary successions, each recording sedimentary sequences across different timescales and driven by distinct forcing mechanisms, such as climate, eustasy and tectonic activity. The case studies focus on Quaternary marine terrace successions, coastal-pond deposits, and algal bioconstructions, which respectively document sea-level and environmental changes at Middle to late Pleistocene, Holocene, and last-millennium timescales. Together, these archives provide complementary perspectives on coastal evolution across a broad temporal range.

Therefore, the aims of this thesis are to: (i) investigate coastal depositional archives and their response to Quaternary climate change; and (ii) provide new quantitative constraints on sea-level fluctuations across a wide range of temporal scales, from hundreds of thousands of years to centuries. A long-term perspective on coastal evolution, preserved in sedimentary sequences, is essential for developing analogues to better understand ongoing and future coastal processes under different climate and eustatic scenarios. In this way, the study integrates stratigraphic evidence from multiple archives and timescales in Sardinia to improve our understanding of coastal response to climate and sea-level change at a Mediterranean scale.

Importantly, this approach enables direct comparison of processes operating across different timescales within a single regional framework, offering new insights into the controls on coastal system variability under changing climatic conditions. To achieve this, the thesis is structured into three main chapters, each focusing on different study sites along Sardinia coasts, distinct sedimentary sequences and different time windows within the last 200.000 years. Finally, these chapters consist of three scientific papers that have been submitted or are ready for submission to international peer-reviewed journals.

Chapter 1

Composite marine terrace as indicators of sea-level fluctuations and differential uplift in tectonically segmented continental margin: insights from southern Sardinia (Mediterranean Sea)

Giovanni Fantini[1], Daniele Sechi[1], Giulia Cossu[2], Toru Tamura[3], Marta Lai[4], Vincenzo Pascucci[4], Stefano Andreucci[1]

[1]*Department of Chemical and Geological Sciences, University of Cagliari, 09042 Monserrato. Italy*

[2]*Department of Chemical, Physical, Mathematical and Natural Sciences. University of Sassari, 07100 Sassari. Italy*

[3]*Geological Survey of Japan, AIST, Tsukuba, Japan*

[4]*Department of Architecture, Design and Urban Planning, University of Sassari, 07041 Alghero. Italy*

Ready to be submitted to a peer-review scientific journal.

Composite marine terrace as indicators of sea-level fluctuations and differential uplift in tectonically segmented continental margin: insights from southern Sardinia (Mediterranean Sea)

Giovanni Fantini[1], Daniele Sechi[1], Giulia Cossu[2], Toru Tamura[3], Marta Lai[4], Vincenzo Pascucci[4], Stefano Andreucci[1]

[1]*Department of Chemical and Geological Sciences, University of Cagliari, 09042 Monserrato. Italy*

[2]*Department of Chemical, Physical, Mathematical and Natural Sciences. University of Sassari, 07100 Sassari. Italy*

[3]*Geological Survey of Japan, AIST, Tsukuba, Japan*

[4]*Department of Architecture, Design and Urban Planning, University of Sassari, 07041 Alghero. Italy*

Abstract

Quaternary marine terraces provide key archives for reconstructing the interplay between sea-level change and tectonic processes along active coastal margins. However, the extent to which terrace stacking patterns reflect eustatic forcing versus uniform/variable uplift remains difficult to assess. In this study, we investigate the Middle-late Pleistocene sedimentary sequence on three sites along the south Sardinia coast. Five unconformity-bounded units are identified and correlated with MIS7, MIS5e and MIS5c highstands documenting repeated phases of marine transgression, shallow-marine system progradation, and regression. The three study areas display contrasting stacking patterns, including composite marine terrace sequences, with superposition of multiple highstand deposits separated by erosional surfaces or a single marine terrace unit.

The elevations of MIS7 and MIS5c shallow-marine units relative to present sea level deviate significantly from global eustatic benchmarks, with mismatches of up to 15–20 m that cannot be explained by glacio-eustatic fluctuations or Mediterranean-scale glacio-isostatic adjustment alone. Instead, the data point to a dominant tectonic control. We propose a model in which southern Sardinia is segmented into distinct crustal blocks experiencing spatially and temporally variable uplift since at least the Pleistocene. The distribution of marine terrace sequences further suggests differential vertical motions and a possible eastward migration of uplift across the south Sardinia.

These findings demonstrate that composite marine terraces represent a key stratigraphic expression of the interaction between tectonics and sea-level fluctuations. More broadly, this study highlights that even in regions characterised by relatively low but variable uplift rates, tectonic segmentation can significantly influence coastal stratigraphy, promoting re-occupation processes and the development of composite marine terrace sequences rather than a staircase of single terraces.

Composite marine terraces thus provide a robust framework for identifying subtle tectonic signals in continental margins often regarded as stable or slowly uplifting.

Key words: *Mediterranean Sea, shallow-marine deposits, coastal sequences, MIS5, MIS7, Quaternary tectonic, sea level change*

1. Introduction

Quaternary marine terrace staircases are widely recognized worldwide as records of the interplay between active tectonics and eustatic fluctuations (e.g., Pedoja et al., 2014; Dorsey et al., 2026; Muhs et al., 2026). Typically, individual marine terraces formed by bedrock wave erosion are commonly interpreted as having formed during single sea-level highstands. Thus, the so-called "staircase of uplifted marine terraces" originates from multiple glacio-eustatic sea-level cycles acting on an unfaulted crustal block undergoing uniform uplift (Robertson et al., 2020). Marine terraces and their associated sea-level markers are, therefore, widely used not only to constrain local relative sea level (RSL) estimates, but also, more broadly, to derive uplift rates along tectonically active margins (e.g. Rovere et al., 2016a; Ferranti et al., 2021; de Gelder et al., 2022; Tamura et al., 2022; Muhs et al., 2026).

However, an increasing number of studies on marine terrace staircases have applied numerical forward models to highlight that a single marine terrace may result from multiple episodes of sea reoccupation and that the assumption of steady uplift over time for the entire sequence is highly questionable (i.e Malatesta et al., 2022; Crosetto et al., 2024). Field-based evidence supporting this interpretation remains scarce, and conceptual stratigraphic models are incipient, but a few studies have revealed that shallow-marine bodies of different ages may reoccupy the same wave-cut platform, producing composite marine terrace sequences (Nalin et al., 2007; Zecchin et al., 2011; Sechi et al., 2022). Moreover, tectonic fragmentation and variable uplift rates may complicate the morphological expression of originally formed coastal deposits (e.g., Robertson et al., 2020; Dorsey et al., 2026).

These complexities are particularly relevant in the Mediterranean region, where interactions among different lithospheric dynamics and glacio-eustatic sea-level changes have produced diverse coastal stratigraphic architectures during the Quaternary. Sardinia has long been considered a relatively stable or slightly subsiding margin (e.g., Ferranti et al., 2006; Lambeck et al., 2011), and its marine sequences have often been interpreted primarily as driven by eustatic forcing. However, recent studies suggest that the island may be affected by subtle but significant tectonic processes, including regional uplift and crustal segmentation linked to the broader geodynamic evolution of the western Mediterranean (Cocco et al., 2019, 2024; Casini et al., 2020). In this context, the occurrence, distribution, and internal architecture of marine terraces in southern Sardinia remain poorly constrained.

This study investigates three key sites along the southern Sardinian coast (West Mediterranean Sea), exposing Quaternary successions through a combination of field observations, stratigraphic analysis, and luminescence geochronology. The aims are to: (i) characterize the stratigraphic architecture and stacking pattern of marine sequences; (ii) assess their relationship with global eustatic sea-level fluctuations; (iii) evaluate the role of tectonic processes in controlling their development and (iv) provide a conceptual stratigraphic model for marine terraces formed on small embayments.

2. Geological setting and study sites

Sardinia is the second-largest island in the Mediterranean Sea, extending from 38° to 41° N and from 8° to 10° E (Fig. 1a) and forms part of the Corsica-Sardinia lithospheric block (C-S block).

During the Oligocene–early Miocene, the eastward migration of the Apennines subduction zone, in conjuction with the opening of the Balearic-Provençal Basin, led to major rifting of the C-S block, which detached from the Provençal–Catalan margin and drifted to its present position in the central western Mediterranean (Fig. 1a; Doglioni et al., 1998). Subsequently the island experienced further segmentation due to the extensional regime associated with the opening of the southern Tyrrhenian basin during Plio-Quaternary times (Casula et al., 2001).

This geodynamic evolution led to the development of the Campidano basin, a NW–SE oriented lithospheric-scale depression that dominates the structural setting of the southern sector of the island (Fig. 1a, b). The Campidano basin accommodated more than 1,000 m of Plio-Pleistocene syn-tectonic deposits in its subsurface (Cocco et al., 2013). Since the Middle Pleistocene (post 700 ka), it has been regarded as stable, having entered a post-rift stage (Cherchi, Marini, Murru, & Ulzega, 1978a; Cherchi et al., 2008). However, geomorphic and structural evidence indicates moderate Pleistocene to Holocene tectonic activity, mainly linked to the reactivation strike-slip faults as normal faults and local uplift (e.g., Cocco et al., 2019, 2024; Casini et al., 2020; Sechi et al., 2022).

Nowadays, Sardinia is located between the Algero/Balearic-Provençal and the active Tyrrhenian back-arc basins. Low-magnitude earthquakes ($M < 4.5$) have been recorded both onshore and offshore, with few small events concentrated along the western margin of the Campidano system (Rovida et al., 2020). Geophysical modelling further suggests that the Corsica-Sardinia Block cannot be regarded as fully stable, and that Pleistocene-to-present regional uplift, where documented, may be enhanced by a lower-crustal mass deficit (Cocco et al., 2024). Furthermore, geophysical constraints and kinematic models, based on GPS-data, indicate that Africa is still moving towards stable Europe yielding to average N-S velocities between 3 to 15 mm/year (Fig. 1; Faccenna et al., 2001; Serpelloni et al., 2007).

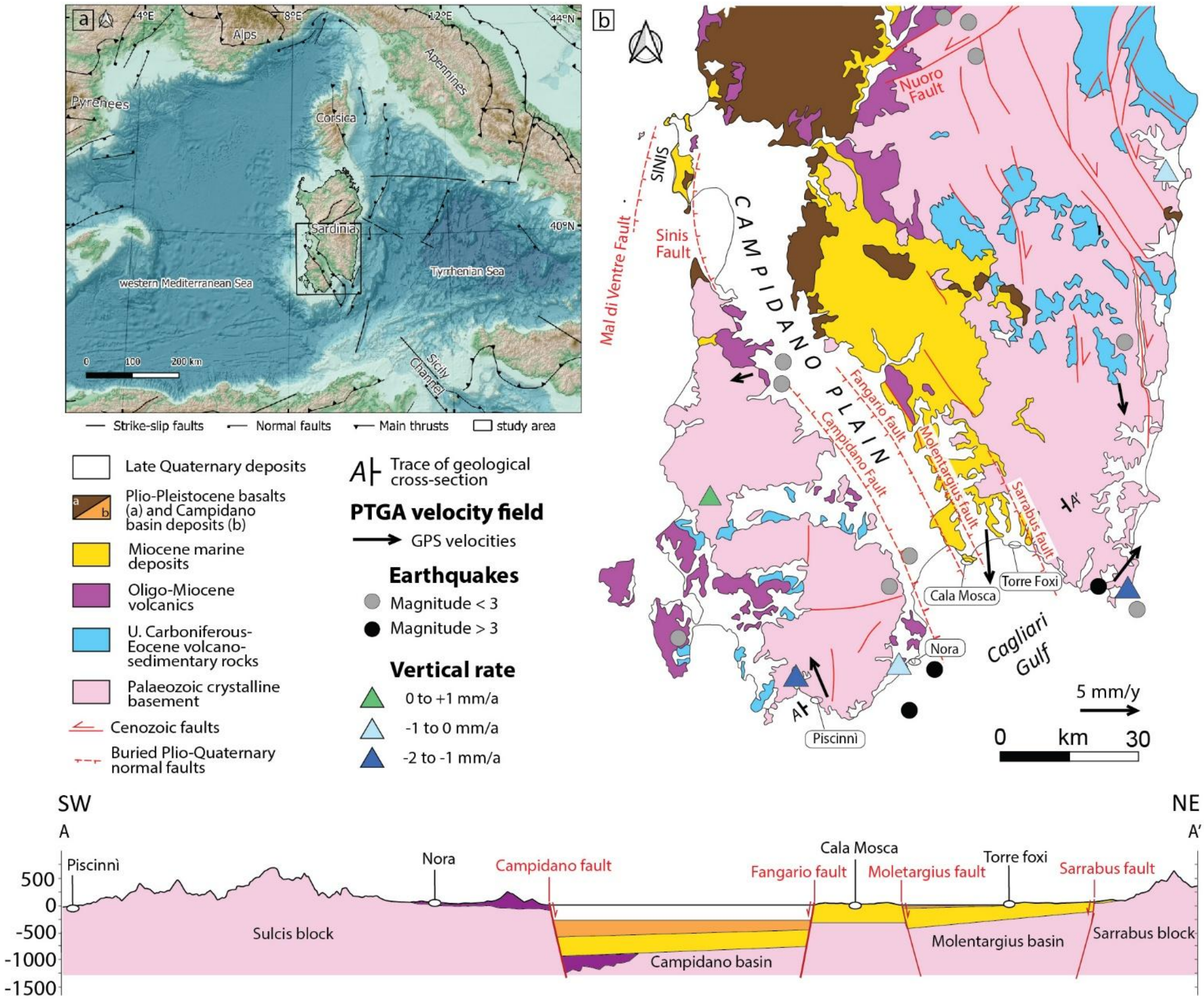

Figure 1. *(a) Present position of the Corsica–Sardinia block in the tectonic framework of the western Mediterranean, modified from Cocco et al. (2024). The black square indicates the panel b area. (b) Geological map of south Sardinia, modified from Carmignani et al. (2016). The Peri-Tyrrhenian Geodetic Array (PTGA) velocity field is from Ferranti et al. (2008); the location and magnitude of seismic events are from INGV (2018); absolute vertical land-motion rates are from Antonioli et al. (2017) and Serpelloni et al. (2013).*

Within this scenario, recent studies have proposed the occurrence of buried Plio-Quaternary normal faults bounding the Campidano system and contributing to the present structural setting of southern Sardinia (Carmignani et al., 2016; Cocco et al., 2019). For these reasons, the key study sites investigated here are distributed across distinct sectors of the southern Sardinian margin (Fig. 1a, b).

Piscinnì is located in the south-western sector of Sardinia, within the Sulcis domain (Fig. 1b). The modern morphology consists of a ~200 m wide southwest-facing headland-bay beach, backed by an incipient vegetated dune system and a small lagoon within the coastal valley. The studied outcrops occur along the flanks of the embayment and are bounded by steep slopes curved into the Paleozoic metamorphic basement.

Nora is located at the transition between the western margin of the Campidano Basin and the Sulcis domain (Fig. 1b). It consists of a volcanic peninsula flanked by two south-facing embayments and bordered to the north-west by the Nora lagoon. The main study outcrops occur along the southern lagoon margin, with additional exposures on the eastern side of the peninsula (Fig. 1b).

Torre Foxi is located on the eastern side of the Gulf of Cagliari, at the transition between the Molentargius Basin and the Sarrabus domain (Fig. 1b). The present-day coast is characterized by south-facing low cliffs, up to 5 m high, exposing the study succession and bounded at their base by a narrow modern gravel beach (Fig. 1b).

3. Methods

3.1 Facies analysis and stratigraphy

A total of 13 lithofacies were identified within the Pleistocene successions cropping out along the southern coast of Sardinia (Table 1; Figs. 2, 3, 4). Lithofacies were distinguished based on sedimentary features (lithology, grain size and sedimentary structures) and macrofossil content. The facies nomenclature follows the main lithology (G = conglomerate, S = sandstone), as along with main textural and structural features (b = boulders to cobbles, c = cobbles to pebbles, d = pebbles to granules, e = medium- to very coarse-grained sand, w = reddish silty matrix, l = laminated, p = planar cross-bedded, t = trough cross-bedded, u = low-angle cross-bedded, m = massive, f = highly fossiliferous, r = root traces, i = imbricated). Their depositional interpretation follows the criteria proposed by Pascucci et al., (2009), Andreucci et al., (2009, 2014) and Sechi et al., (2020, 2022). The lateral and vertical distribution of these facies enabled the definition of six facies associations, including four shallow-marine and two coastal–continental, described in detail below and summarized in Table 1.

Unconformity-Bounded Stratigraphic Units (UBSUs) were measured and correlated in the field based on sedimentary body lithologies and geometries (facies association architecture), as well as on the recognition of visible unconformities and abrupt facies changes. Five UBSUs were identified and named U0, U1, U3a, U3b, and U4, following the nomenclature of Pascucci et al. (2014).

Facies Associations	Facies	Description	Process	Interpretation	Photo
Tl	Gem	Poorly organized, openwork, clast-supported conglomerate. It contains sub-rounded boulders to cobbles with abundant shell fragments within a gravel- to coarse-grained sand matrix.	Marine wave and/or longshore currents	Conglomerate lag deposits	
	Bef	Highly fossiliferous carbonate deposits composed hexacorals, crustose coralline algae, and bivalves, with sandy sediments containing rounded granules and pebbles of mixed bioclastic and siliciclastic origin.	*C. caespitosa* build up with sporadic longshore currents sediment imput	Hexacorals dominated Reef deposits	
Mb	Sdt	Medium- to coarse-grained trough cross-bedded sandstone intercalated with layers of rounded cobbles to pebbles and marine shells	Marine waves and/or longshore currents, bars and trough	Upper shoreface deposits	
	Sdu	Medium- to coarse-grained, low-angle cross-bedded sandstone, gently dipping seaward and containing aligned quartz-rounded pebbles to granules and shell fragments.	Waves swash and backwash	Foreshore deposits	
Sb	Sedt	Medium- to coarse-grained trough cross-bedded sandstone with scattered rounded Qz granules and marine shells	Marine waves and/or longshore currents, bars and trough	Upper shoreface deposits	
	Seu	Medium- to coarse-grained, low-angle cross-bedded sandstone, gently dipping seaward and containing aligned quartz-rounded clasts and shell fragments.	Waves swash and backwash	Foreshore deposits	
	Seur	Low-angle cross-bedded, medium-grained, well-sorted sandstone, variously fossiliferous and bioturbated by roots at the top.	storm waves washover, wind and vegetations	backshore deposits	
Gb	Gci	Matrix-supported conglomerate composed of sub-rounded disc-shaped pebbles, imbricated landward, within a poorly sorted sandy matrix with alligned rounded granules.	Marine waves washing up on foreshore	Beachface, sand trap zone	
	Gcoi	Openwork, clast-supported conglomerate, composed of rounded and disc-shaped cobbles and pebbles, commonly imbricated landward and dipping seaward.	Marine waves washing up inland during major storms	Beachface, imbricated zone	
E	Sept	Pale yellowish, well-sorted, medium- to coarse-grained, planar, high-angle cross-bedded sandstone, in sets up to 1 m thick.	Aeolian sediment transport	Aeolian sand dune deposits	
	Semr	Pale yellowish, well-sorted, medium- to coarse-grained,massive sandstone, in sets up to 1 m thick. Root traces are widespread.	Aeolian sediment transport	Aeolian sand dune deposits	
C	Sew	Reddish sandy-sitly deposit with dispersed angular, poorly sorted granules to pebbles.	gravity-flow	colluvial deposits	
	Gwc	Reddish, sandy-silty, matrix-supported conglomerate with angular boulders to pebbles	gravity-flow	debris flow deposits	

Table 1. *Brief description of the observed facies at the study areas. Facies labels are based on the following nomenclature: G = conglomerate, S = sandstone, b = boulders to cobbles, c = cobbles to pebbles, d = pebbles to granules, e = medium to very coarse-grained sand, w = reddish silty matrix, l = laminated, p = planar cross-bedded, t = trough cross-bedded, u = low-angle cross-bedded, m = massive, f = highly fossiliferous, r = root traces, i = imbricated.*

Luminescence dating of shallow-marine deposits, together with U/Th analyses on coral boundstone bodies, were employed to provide a robust chronological framework for the studied sequences (Table 2).

3.2 Luminescence dating

Two samples for each study site (PX1, PX2, NOR1, NOR3, TFX1 and TFX2; Table 2; Fig. X) were collected from the beach deposits for luminescence dating as light-protected blocks (~50 × 50 × 40 cm) and treated at the University of Sassari Luminescence Dating Laboratory during winter 2024. In the laboratory, under subdued red light, the outer part of the blocks (up to 10 cm) was chiseled off from all sides removing potential light-exposed part; this material was subsequently used to determine water content and total dose rate. The inner part of each sample was gently crushed and chemically treated with 40% HCl and 40% H_2O_2 to remove carbonate cements and organic matter and obtain the siliciclastic fraction. The material was subsequently sieved, and the most abundant fraction (see Tab. 2) selected to isolate quartz and K-feldspar crystals by density using a heavy liquid solution. Quartz and K-feldspar grains were etched with HF (etch depth ~10 μm) to remove the external alpha-irradiated rim.

Sample	GS μm	(n)	OD (%)	De pIRIR225 (Gy)	Rd (Gy)	g_{2days} (%/decade)	Dr (Gy/ka)	Age (ka)	Unit	MIS
PX1	212 - 250	9	6.7	399 ± 10.4	7.0 ± 1.2	1.46 ± 0.10	2.07 ± 0.06	193 ± 14	U1	7
PX2	212 - 250	9	5.0	231 ± 4.0	6.4 ± 0.2	1.71 ± 0.09	1.71 ± 0.08	135 ± 11	U3a	5e
NOR1	90 - 180	9	2.3	490 ± 10.7	12.2 ± 2.6	1.59 ± 0.14	3.86 ± 0.03	127 ± 5	U3a	5e
NOR3	125 - 180	9	7.7	406 ± 11.3	9.7 ± 0.6	1.81 ± 0.11	2.83 ± 0.04	143 ± 7	U3a	5e
TFX1	212 - 250	9	3.6	519 ± 6.0	8.6 ± 0.1	2.07 ± 0.10	3.84 ± 0.03	135 ± 6	U3a	5e
TFX2	212 - 250	9	1.3	613 ± 4.4	9.0 ± 1.2	2.01 ± 0.10	5.96 ± 0.02	103 ± 3	U3b	5c

Table 2. *Summary of pIRIR225 luminescence dating results; sample code, (GS) Grainsize of the measured sample, (n) the number of reliable aliquots used for dating, (OD; %) overdispersion of De expressed in percentage; K-feldspar $pIRIR_{225}$ doses, (RD) residual dose; (g_{2days}) fading rate; and (Dr) total dose rate (Gy/ka). Estimated ages in ka, related Unit and MIS (marine isotope stage). For more details of determination of ages and dose rates, see the Supplemental Material (Supplementary Table SM1).*

Luminescence measurements were performed at the luminescence laboratory of the Geological Survey of Japan (Tsukuba) using a TL/OSL DA-20 Risø reader equipped with a calibrated $^{90}Sr/^{90}Y$ beta source for laboratory irradiation. OSL signal from quartz was detected with blue LEDs (450-475 nm) and UV filter Hoya U-340, while for the signal from K-feldspar infrared (IR) LEDs centred at 850 nm for stimulation and a combination of Schott BG3, BG39 and GG400 filters were used. SAR OSL and pIRIR protocols were adopted for quartz and K-feldspar, respectively.

Preliminary measurements showed quartz OSL signals close to saturation, whereas K-feldspar exhibited stable and reproducible luminescence behavior; therefore, De determination was performed on K-feldspar using the pIRIR225 protocol. The modified single-aliquot regenerative-dose pIRIR225 protocol (Thomsen et al., 2008; Buylaert et al., 2009; Reimann and Tsukamoto, 2012; Tamura et al., 2022) was adopted because stimulation at 225 °C provides a thermally more stable signal and reliable laboratory behavior in comparable coastal deposits (Thiel et al., 2010, 2015; Sechi et al., 2022). Standard SAR criteria of recycling (within 0.9 and 1.1) and recuperation (not above 5% of natural) were used to reject unreliable aliquots.

The protocol included a preheat at 255 °C for 60 s, followed by an IR stimulation at 50 °C to remove the unstable low-temperature IRSL component and a subsequent stimulation at 225 °C (pIRIR225) to measure the more thermally stable signal. The net signal was derived from the integral of the first 2.0 s after subtracting the background estimated from the last 50 s of the signal. Fading rates ($g_2$days) were determined following Auclair et al. (2003). A dose recovery experiment was carried out on 3 bleached aliquots per sample to evaluate the accuracy of the protocol in recovering a known laboratory-given dose. Nine medium-sized aliquots (6 mm) per sample were measured and used for De calculation (Table 2). Overdispersion values are low (1.3–7.7%), indicating internally consistent De distributions. Residual doses were measured on 3 naturally bleached aliquots per sample (Tab. 2).

Environmental gamma and beta dose rates were determined by direct measurement using a combined approach with a Risø NaI (Tl) scintillation gamma spectrometry system (Bu et al., 2021) and a low-level gas-flow beta counter a GM-25-5 (GMBC; Bøtter-Jensen and Mejdahl, 1988). For both gamma spectrometry and low-level beta counting, the samples were embedded in wax according to the protocols described by Murray et al. (2018) and Cunningham et al. (2018), respectively. The prepared casts were subsequently stored for 20 days prior to measurement to ensure re-establishment of radioactive equilibrium within the decay chains. The activity concentrations derived from gamma spectrometry were used as prior values for the calculation of the beta dose rate. K, U and Th radionuclide activities were converted to dry dose rates following Guèrin et al. (2011) and Cresswell et al. (2018). Internal dose contribution (Tab. SM1) for K-rich feldspar was considered, assuming ^{40}K and ^{87}Rb concentrations based on Huntley and Baril (1997) and Readhead (2002). The dry dose rates were corrected for moisture content following Sechi et al. (2020) and the cosmic contribution was based on the geographical position, altitude, and the measured sample burial depth following Prescott and Hutton (1994). Dose rate results are summarized in Table SM1.

3.3 U-series method

Two samples of *Cladocora caespitosa* coral branches in living position (TFX1_U1 and TFX1_U2) were collected and sent to Isobar Science laboratory (Miami, FL, USA) for U–Th dating. Surface of the sample was cleaned by means of abrasion followed by multiple rounds of sonication in MilliQ water (18 mΩ). Subsequently, samples were rinsed with MilliQ water and dried at 40°C. Around 20 mg of homogenized sample was dissolved in 0.45 M HNO_3 to minimize leaching of uranium and thorium from detrital materials.

sample	Lab ID	U (ppm)	$^{234}U/^{238}U$	2σ (%)	$^{230}Th/^{234}U$	2σ (%)	$^{230}Th/^{232}Th$	2σ (%)	Age (ka)	Initial $^{234}U/^{238}U^{a}$	Corrected age (ka)	MIS
$TFX1\_U_1$	IS-1589	3.357	1.1279 ± 0.0070	0.62	0.8455 ± 0.0138	1.63	77.28 ± 1.33	1.72	144.8 ± 4.9	1.128 ± 0.007	142.6 ± 4.8	5e
$TFX1\_U_2$	IS-1590	3.427	1.1330 ± 0.0061	0.54	0.8411 ± 0.0161	1.91	12.58 ± 0.24	1.94	141.8 ± 5.4	1.133 ± 0.006	129.2 ± 6.2	5e

[a] Data deriving from $^{230}Th/^{234}U$ ratio.

Table 3. *Summary of Uranium concentration, U/Th ratios, row and corrected ages. Uncertainties represent two standard error (2σ).*

Isolation of uranium and thorium from each sample was achieved by extraction chromatography using *Eichrom* UTEVA resin following the methods of Pourmand et al., 2013 and Pourmand and Dauphas, 2010. High precision uranium and thorium isotope analysis was performed on a Thermo Fisher Neptune Plus^{TM} MC-ICP-MS with an Apex-Q desolvation nebulizer. Each sample measurement was bracketed with measurements of two wash solutions and two certified reference materials (CRM-112A and IRMM-035 for uranium and thorium respectively). Uncertainties on the U-Th ages are reported at the 95% confidence interval (CI) and include propagation of systematic and random uncertainties by Monte Carlo simulation of measured analytical uncertainties on isotope ratios, and those associated with U and Th isotope decay constants. Age calculation and propagation of uncertainties were performed by using Monte Carlo simulation (Pourmand et al., 2013) and by taking into account the measured isotopic ratios of U and Th derived along with other variables such as the spike mass and concentration, sample mass, the decay constants of U and Th isotopes along with their associated uncertainties. The average initial $^{230}Th/^{232}Th$ activity ratio of 0.6±0.2 is used to correct for contribution of the detrital fraction to ^{230}Th. Analytical results are given in Table 3.

3.4 Calculation of paleo relative sea level (RSL)

Field measurements and elevation data were collected during surveys at Piscinnì, Torre Foxi, and Nora (southern Sardinia). At each site, the elevation (*E*) of the dated sample or the corresponding stratigraphic level was measured relative to the instantaneous sea surface using a metric tape or handheld GPS. Given the microtidal regime along the Sardinian coast (ca. 0.3 m), the observed sea level was assumed to approximate the mean sea level (MSL) within ±0.15 m. This value was incorporated into the total vertical uncertainty of the elevation data. Measured elevations (*E*) were converted into paleo–relative sea-level (RSL) values following the facies-based approach of Rovere et al. (2016; Tab. 4). For each sea-level marker, the depositional environment and its indicative meaning were quantified using two parameters: the indicative range (IR) and the reference water level (RWL). The IR represents the total vertical interval, bounded by an upper and lower limit within a given facies typically forms with respect to the contemporary mean sea level.

Site	Environment (facies code)	Sample	Unit	Age (ka)	E (m)	IR (m)	RWL (m)	RSL (m)	MIS
Piscinnì	Upper-shoreface (Sdt)	PX1	U1	193 ± 14	1.0 ± 0.2	3	−2.5	3.5 ± 1.5	7a
Piscinnì	Foreshore (Seu)	PX2	U3a	135 ± 11	1.4 ± 0.2	2.5	0.8	0.7 ± 1.3	5e
Nora	Upper-shoreface (Sdt)	NOR1	U3a	127 ± 5	0.8 ± 0.2	5	−3.5	4.3 ± 2.5	5e
Nora	Upper-shoreface (Sdt)	NOR3	U3a	143 ± 7	1.5 ± 0.2	5	−3.5	5.0 ± 2.5	5e
Torre Foxi	Reef-proximal (Bef)	TFX1	U3a	135 ± 6	0.8 ± 0.2	4	−4.0	5.0 ± 2.0	5e
Torre Foxi	Reef-proximal (Bef)	TFX1_U	U3a	137 ± 4	0.4 ± 0.2	4	−4.0	4.5 ± 2.0	5e
Torre Foxi	Foreshore (Gci)	TFX2	U3b	103 ± 3	2.0 ± 0.2	2.5	0.8	1.3 ± 1.3	5c

Table 4. *Elevation measurements and paleo–relative sea-level (RSL) estimates for the studied coastal site. Site: sampling locality; Environment (facies code): depositional setting used to define the indicative meaning; Unit: stratigraphic unit; Sample: dated specimen; Age (ka): luminescence or U/Th age (1σ uncertainty); MIS: Marine Isotope Stage; E: elevation of the sampled point above present mean sea level; IR: indicative range, i.e. vertical interval over which the corresponding facies typically develops, based on modern analogs; RWL: reference water level, i.e. central elevation of the indicative range; RSL: calculated paleo–relative sea level (propagated 1σ uncertainty). All elevations are given relative to present mean sea level.*

The reference water level (RWL) corresponds to the midpoint between the upper and lower limits of the indicative range and represents the average elevation at which the facies most likely formed relative to mean sea level. Both IR and RWL values were defined from modern analogs of comparable coastal environments (Table S2), allowing the conversion of measured elevations into paleo–RSL estimates that are directly comparable across sites and facies types. Uncertainties in RSL (δRSL) combine the instrumental precision and half of the indicative range. All parameters were calculated using equations of Rovere et al. (2016). Derived values are summarized in Table 4, whereas the full dataset, including indicative meaning parameters and propagated uncertainties, is provided in Supplementary Tables SM2.

4. Results

4.1 Facies analysis

Thirteen depositional facies (Gem, Bef, Sdt, Sdu, Sedt, Seu, Seur, Gci, Gcoi, Sept, Semr, Sew, Gwc; Table 1) have been recognized in the studied coastal successions. These are grouped into four shallow-marine (Tl, Mb, Sb, and Gb) and two coastal–continental (E, C) facies associations which are described below.

4.1.1 Facies association Tl – Transgressive deposits

The transgressive deposits (facies association Tl) is subdivided into two facies (Gem and Bef) The medium to coarse sand grains are mixed of both marine bioclastic material (bivalves, red algae, mollusks, echinoids, benthic foraminifera, and bryozoans) and siliciclastic components (quartz, feldspar, and metamorphic/volcanic rock fragments) whereas conglomerates (mainly pebbles) reflect the local bedrock. unconformable overlying the Paleozoic bedrock and/or strata of facies associations Mb and C (mixed beach and colluvial facies associations; Figs. 2, 3, 4).

Facies Gem (Figs. 2, 3, 4) consists of massive to poorly organized, clast-supported coarse sandy conglomerates forming strata up to 50 cm thick. Clasts are sub-rounded to rounded, range in size from boulders to cobbles reflecting the local bedrock compositions. The interstices are filled with medium- to coarse-grained mixed bioclastic and siliciclastic sands with few broken marine shells. This facies can occur as matrix-supported forming mixed coarse sandy conglomerate to mixed sandstone with aligned pebbles in strata up to 30 cm-thick. Locally, pebbles are dominated by rounded to subrounded rodoliths (Fig. 3). Facies Gem unconformable rests on a well-developed erosive surface filling depressions carved on the bedrock and/or strata of facies associations Mb and C (mixed beach and colluvial facies associations; Figs. 2, 3, 4).

Facies Bef consists of a metre-thick, decametre-long hexacoral (*Cladocora caespitosa*) boundstone preserved in growth position (Fig. 4). The coral colonies form pillow-shaped structures densely encrusted by crustose coralline algae, creating a rigid framework. This framework is surrounded by mixed bioclastic and siliciclastic sand containing scattered rounded granules to pebbles and fragmented to disarticulated marine shells. Facies Bef conformable rests on gravelly strata of facies Gem.

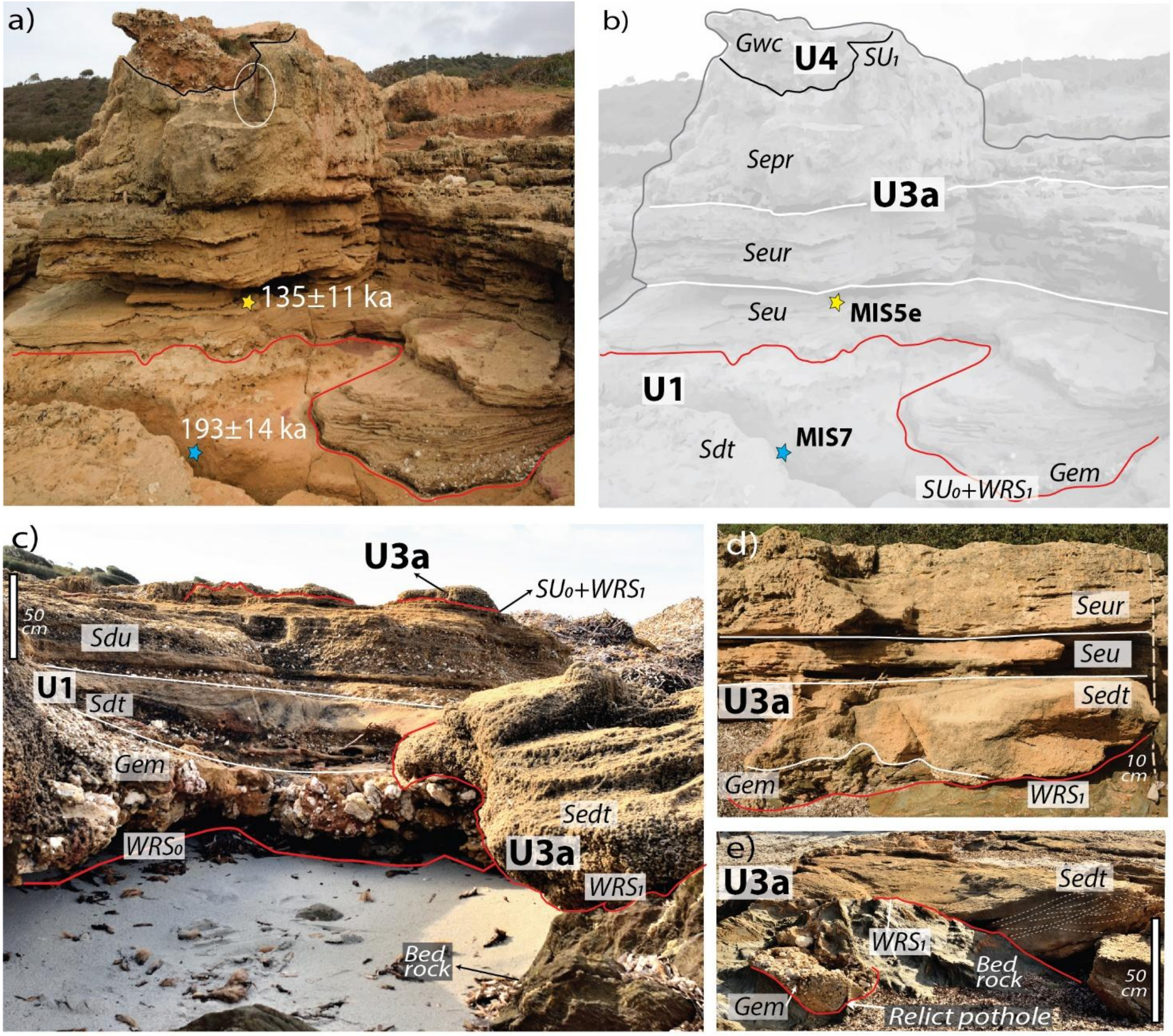

Figure 2. *Piscinnì study site. (a) Superposed beach deposits of units U1 and U3a with the position of dated samples. The red line outlines the main unconformity between the two units; hammer in the white circle for scale. (b) Stratigraphic interpretation of panel (a), showing the facies architecture of U1 and U3a, their chronostratigraphic attribution to MIS 7 and MIS 5e, and the erosional surface formed by subaerial exposure and wave-ravinement surfaces (SU0 + WRS1, respectively). (c) Outcrop view of unit U1, from the transgressive lag deposit Gem above transgressive surface WRS0 to the prograding beach deposits in facies Sdt and Sdu. (d, e) Outcrop details of SU0 + WRS1 overlying the bedrock and directly bounding the MIS 5e sandy beach of* unit U3a; (e) shows *a pothole carved into the bedrock and the cross-stratification of facies Sedt. The white line marks the facies boundary.*

Interpretation of Tl facies association

The basal unconformity records wave erosion associated with shoreline retreat during the transgressive phase (Massari and Parea, 1988). In particular, along cliffed coasts, this erosional surface corresponds to the wave-cut platform developed in the intertidal to shallow subtidal zones of a marine terrace (Postma and Nemec, 1990; Sechi et al., 2022). Facies Gem drapes the wave-cut platform, locally infilling depressions and potholes (*sensu* Sechi et al., 2022) with a discontinuous veneer of subtidal, gravelly transgressive-lag deposits (Massari and Parea, 1988; Zecchin et al., 2019). Rodolith-bearing strata within Facies Gem are interpreted as transgressive shell lags formed under relatively high-energy conditions and very shallow water conditions filling depressions carved the bedrock and/or within narrow submerged palaeotopographic lows (*sensu* Basso et al., 2009; Nalin et al., 2008). The hexacoral boundstone of facies Bef developed as patch reefs above the submerged rocky substrate or conglomeratic lag (Gem) deposits. Facies Bef preferentially developed areas with limited sediment supply during the late transgressive phase (Nalin and Massari, 2009).

4.1.2 Facies association Mb – Mixed sandy-gravelly beach deposits

The mixed sandy–gravelly beach deposits (facies association Mb) comprise sandstone bodies interbedded with thin conglomerate layers (Figs. 2, 4). The sand is medium- to coarse-grained and contains mixed marine bioclastic material (bivalves, red algae, mollusks, echinoids, benthic foraminifera, and bryozoans) and siliciclastic components (quartz, feldspar, and metamorphic to volcanic rock fragments). The conglomerates, composed mainly of pebbles, reflect the composition of the local bedrock. Facies association Mb includes two facies (Sdt and Sdu) and, conformably overlies the conglomeratic lag deposits of facies Gem.

Facies Sdt consists of medium- to coarse-grained, granule- to pebbly sandstone with trough cross-beds forming bodies up to 1 m thick (Table 1; Fig. 2, 4). Rounded granules and pebbles are aligned along the bases of the trough cross-sets, and their composition reflects the local bedrock. Locally, pebbly fossil-rich sandstones forming 10–20 cm thick strata developed on a sharp erosive surface. Facies Sdt conformably overlies the gravelly strata of facies Gem.

Facies Sdu comprises medium- to coarse-grained sandstone forming decimetre-thick beds with low-angle, seaward-dipping cross-stratification. Thin (5–10 cm) layers of low-angle cross-stratified, granule- to pebbly sandstone commonly occur within the sandstone bodies. Facies Sdu conformably overlies the pebbly sandstone strata of facies Sdt.

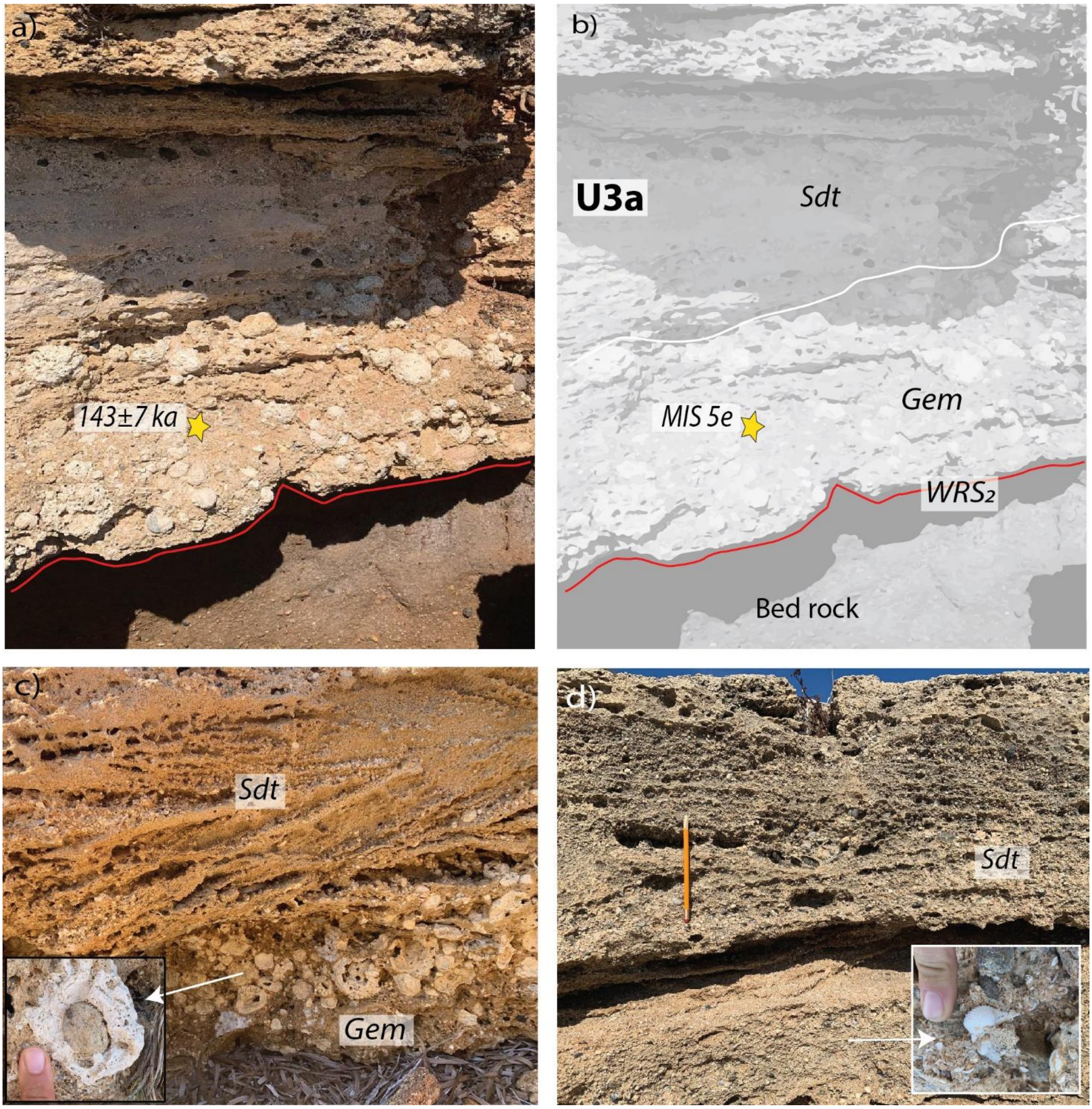

Figure 3. *Nora study site. (a) Outcrop detail of unit U3a with the position of dated samples; the red line outlines the main unconformity surface. (b) Stratigraphic interpretation of panel (a), showing unit U3a in facies Gem and Sdt lying above WRS1. (c) Detail of subrounded rhodoliths in facies Gem. (d) Detail of cross-stratification of sandstone in facies Sdt.*

Interpretation of Mb facies association

The Mb facies association represents a mixed sandy–gravelly, wave-dominated beach system (Postma and Nemec, 1990). Facies Sdt, characterized by trough cross-bedding, records the development of submerged bars in the upper shoreface, formed by longshore currents or fair-weather wave breaks (Isla et al., 2020). In contrast, thin pebbly, fossil-rich strata mark major storm events. Facies Sdu, dominated by low-angle cross-stratification, represents foreshore deposits formed by wave swash and backwash processes. Overall, the Mb facies association records a shallowing-upward trend from subtidal upper shoreface to foreshore environments, reflecting a prograding (normal regression) phase of a mixed sandy–gravelly beach system.

4.1.3 Facies association Sb – Sandy beach deposits

Facies association Sb consists of well-stratified sandstones forming bodies up to 1 m thick (Fig. 2). The sand is medium- to coarse-grained and composed of mixed marine bioclastic material (red algae, bivalves, molluscs, echinoids, benthic foraminifera, and bryozoans) and siliciclastic components (quartz, feldspar, and metamorphic to volcanic rock fragments). Fragmented and disarticulated marine shells are common and typically aligned at the base of beds. Facies association Sb includes three facies (Sedt, Seu, and Seur) and, unconformable overlies the mixed sandy–gravelly deposits of facies association Mb.

Facies Sedt comprises trough cross-bedded sandstone forming strata up to 40 cm thick (Figs. 2e-d). Locally, it also contains massive, very coarse sand lenses rich in marine shells.

Facies Seu consists of well-sorted, low-angle cross-bedded sandstone, with laminae gently dipping seaward in beds up to 60 cm thick (Figs. 2a-b-d). Alternations of millimetre-thick dark (heavy mineral-rich) and light (bioclastic-rich) laminae are common.

Facies Seur is composed of metre-thick sandstone units with decimetre-thick strata showing faint, sub-horizontal to low-angle cross-stratification, and pervasive root bioturbation towards the top (Figs. 2a-b-d).

Interpretation of Sb facies association

Facies association Sb is interpreted as representing a wave-dominated sandy beach system (Postma and Nemec, 1990). The bar and trough sandstones of facies Sedt indicate upper shoreface deposition influenced by wave action and longshore currents (Isla et al., 2020). The low-angle cross-bedded strata of facies Seu reflect foreshore deposits formed by swash and backwash processes. The highly bioturbated sandstone bodies of facies Seur represent backshore environments, where pervasive root traces progressively obliterated the stratification. Overall, facies association Sb records a shallowing-upward trend from the submerged to the subaerial vegetated zone, reflecting the progradation (normal regression) of a sandy beach system.

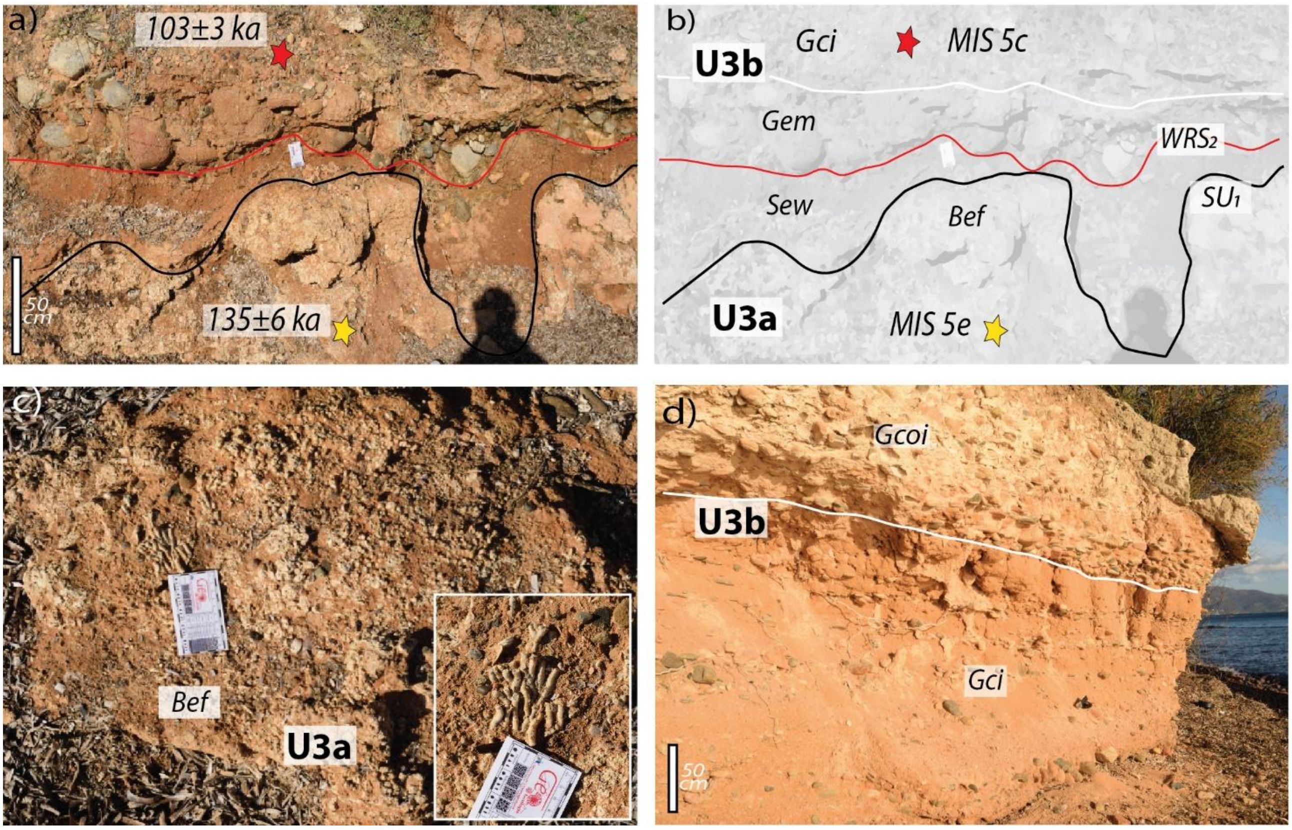

Figure 4. *Torre Foxi study site. (a) Superposed beach deposits of units U3a and U3b with the position of dated samples. The red line outlines the main unconformity between the two units, and the black line marks the subaerial exposure surface. (b) Stratigraphic interpretation of panel (a), showing the facies architecture of U3a and U3b, their chronostratigraphic attribution to MIS 5e and MIS 5c, respectively, and the erosional surfaces SU1 and WRS2. (c) Outcrop view of unit U3a in facies Bef, with detail of Cladocora caespitosa branches. (d) Outcrop view of unit U3b, passing upward from facies Gci to Gcoi. The white line marks the facies boundary.*

4.1.4 Facies association Gb – Gravelly beach deposits

Facies association Gb comprises sub-rounded to rounded, pebbly to bouldery conglomerates forming bodies up to 2-metre thick. Facies association Gb is subdivided into facies Gci and facies Gcoi and unconformably overlies the reddish sandy-silty deposits of facies association C (Table 1, Fig. 4).

Facies Gci is characterized by an alternation of clast-supported conglomerate beds and sandy layers forming deposits up to 2-m thick (Fig. 4c-d). The conglomerate beds, up to 20 cm-thick consist of moderately to well sorted, sub-rounded to discoidal pebbles imbricated landward, with pore spaces filled by a coarse sandy matrix containing sparse rounded granules (Fig. 4c-d). The sandy layers are lenses up to 50 cm thick and decametric long interbedded with the conglomerate bodies. sands are well-sorted, medium grained and contain few marine shell fragments.

Facies Gcoi is composed of openwork, clast-supported conglomerates consisting of rounded to discoidal cobbles and pebbles, commonly showing landward imbrication within decimetre-thick, seaward-dipping strata (Fig. 4b). In places, these deposits include sparse, disarticulated and broken marine shells as well as granule-rich lenses.

Interpretation of Gb facies association

Facies association Gb represents the beachface zones of a gravelly beach system (Fig. ; Pascucci et al., 2008). Facies **Gci** is interpreted as the seaward part of the beachface, characterized by alternating gravel berms and associated sand-trap deposits (Sechi et al., 2022). Facies Gcoi, in contrast, records the storm berms likely formed in the more landward portion of the beachface (imbricated zone), corresponding to supratidal gravel berms sensu Pascucci et al. (2008). Overall, facies association Gb record a minor progradation of a gravelly beach system.

4.1.5 Facies association E – Aeolian deposits

Facies association E consists of medium sandy bodies up to 1-m thick subdivided into two facies (Sept, Semr; Fig. 2). The sand grains are mostly composed of marine bioclastic material (red algae, mollusks, echinoids, benthic foraminifera, and bryozoans), with minor siliciclastic components. Facies association E rests conformable on sandy beach deposits of facies association Sb.

Facies Sept consists of well-sorted, medium- to coarse-grained, high-angle cross-bedded sandstone in sets up to 1 m thick (Fig. 2). Foresets dip 15–30°, generally toward SE or S. Rare root traces and terrestrial gastropods occur.

Facies Semr consists of well-sorted, medium- to coarse-grained sandstone in strata up to 1 m thick (Fig. 2). Root traces are widespread and almost completely obliterate stratification.

Interpretation of E facies association

Facies association E represents a coastal aeolian dune system. The dominance of high-angle cross-beds dipping SE to S of facies Sept most likely records active coastal dune system probably related to prevailing W–NW winds. Facies Semr, instead represents highly vegetated aeolian sand-sheet deposits (Andreucci et al., 2010).

4.1.6 Facies association C – Colluvial deposits

Facies association C consists of reddish, matrix-supported conglomerates (Gwc) and sandy–silty layers with dispersed angular clasts (Sew; Fig. 2-4). This facies association unconformably overlies the patchy coral reefs of facies association Tl and the dune sandstones of facies association E.

Facies **Gwc** consists of decimetre-thick, reddish, silty, matrix-supported conglomerate lenses containing angular pebbles to boulders reflecting the local bedrock lithologies. These deposits drape and fill small-scale depressions (up to 50 cm wide and 20 cm deep) carved into the underlying strata (Fig. 2a-b).

Facies **Sew** (Fig. 4c-d) comprises 20–50 cm-thick strata of reddish sandy–silty material containing dispersed or aligned, angular, poorly sorted granules to pebbles that reflect the local bedrock composition. Occasional boulders and cobbles of facies Bef occur. The sand fraction is dominated by marine bioclastic components (red algae, molluscs, echinoids, benthic foraminifera, and bryozoans), with minor siliciclastic material.

Interpretation of C facies association

Facies association C is interpreted as representing colluvial slope deposits. Facies Sew corresponds to mud-like flow deposits dominated by gravity processes with minor running water influence. The occurrence of coral-derived boulders indicates local reworking and incision into the underlying marine units. Facies Gwc records silty to sandy debris-flow deposits emplaced by gravity-driven flows that filled shallow gullies in the more distal portion of alluvial-fan systems (Andreucci et al., 2014).

4.2 Chronology

The studied shallow marine deposits along the southern Sardinian coast have been dated with a total of six luminescence (pIRIR225) on k-feldspar grains and two U/Th on coral samples (Tables 2, 3).

Luminescence properties of the analyzed samples are overall good, with signals well-fitting on the Dose response curves. Recycling ratios were within 10% of unity, and recuperation remained below 5% of the natural signal. Dose recovery ratios were close to unity, confirming the ability of the $pIRIR_{225}$ protocol to accurately recover a given laboratory dose. Residual doses range between 6.4 ± 0.9 Gy and 12.2 ± 1.5 Gy and were subtracted from the average De (Table 2). Fading rates ($g_2$days) yielded low values ranging between 1.46 and 2.07 %/decade (Table 2). Given the low fading values and the overall good laboratory performance of the pIRIR225 signal, no fading correction was applied to the final ages. This is also consistent with what is often found for high temperature pIRIR protocols and with previously published Sardinian luminescence samples (Thomsen et al., 2008; Buylaert et al., 2009; Sechi et al., 2022). The pIRIR225 ages derived for the specific sites are summarized in Table 2 and briefly described below from west to east.

At the Piscinnì site, equivalent dose (De) values decrease significantly from the base to the top of the successions, as expected (Table 2). Sample PX1 (Log 3 of Fig. 5) from the upper shoreface deposits (facies Sdt) of a mixed sandy-gravelly beach systems, has an age of 193 ± 14 ka (Fig. 5). Sample PX2, instead, taken from the overlying foreshore deposits (facies Seu) of a sandy beach system, has an age of 135 ± 11 ka (Fig. 5).

At the Nora site, samples NOR1 and NOR3 (Log 1 and 3 of Fig. 6) were collected from the same upper shoreface deposits of a mixed sandy-gravelly beach system cropping out at the easternmost and westernmost sides of the study area, respectively. The unexpected great variability of De values within the two samples is possibly driven by Dose rate heterogeneity, due to the local concentration of volcanic clasts (rich in ^{40}K) aligned at the base of the beds. The derived ages of 143 ± 7 ka and 127 ± 5 ka show an acceptable consistency between each other within the error (Fig. 6).

At Torre Foxi site, sample TFX1 was collected from the *hexacoral* dominated boundstone (facies Bef) and sample TFX 2 from the overlying beachface deposits of gravelly beach system (Fig. 7). The great variability of De and Dr values within the two samples is most likely associated with the common presence of volcanic pebbles and cobbles rich in radioactive Potassium (40K) derived from the volcanic bedrock in the gravelly beach system. Thus, TFX1 has an age of 135 ± 5 ka and TFX2 of 103 ± 3 ka. It is worth noting that the U/Th ages of 143 ± 5 ka and 129 ± 6 (Tab. 3; average 137 ± 4 ka) collected from the *Cladocora caespitosa* coral boundstone (in living position TFX1_U) at the base of the sedimentary succession show an excellent agreement with the luminescence-derived data (135 ± 5 ka, fig. 7).

4.3 Stratigraphy

Log correlation of various sedimentary bodies (facies associations) and key discontinuities across the different study areas outlines a total of five unconformity-bounded stratigraphic units (UBSUs): U0, U1, U3a, U3b, and U4 (following the terminology proposed by Pascucci et al., 2014). A description of the sequence cropping out along the study sites is provided below, from west to east.

4.3.1 Piscinnì

The studied 4 m thick maximum sequence rests unconformably on the Paleozoic bedrock, and is subdivided into four UBSUs: U0, U1, U3a, and U4.

The lower unit U0 consists of debris flow and colluvial deposits sharply overlain by a highly vegetated aeolian sandstone bodies (facies association C and E; Fig. 5). The basal unconformity (SU_x) is carved on the bedrock and most likely represents a period of subaerial exposure. Unit U1 comprises a gravelly lag overlain by a mixed sandy–gravelly beach system showing a well-defined prograding trend from upper-shoreface to foreshore deposits (facies associations Tl, Mb; Fig. XX). The basal erosive surface (WRS_0), cut on the bedrock or on deposits of unit U0, represents a wave ravinement developed during the sea transgression (*sensu* Zecchin et al., 2019).

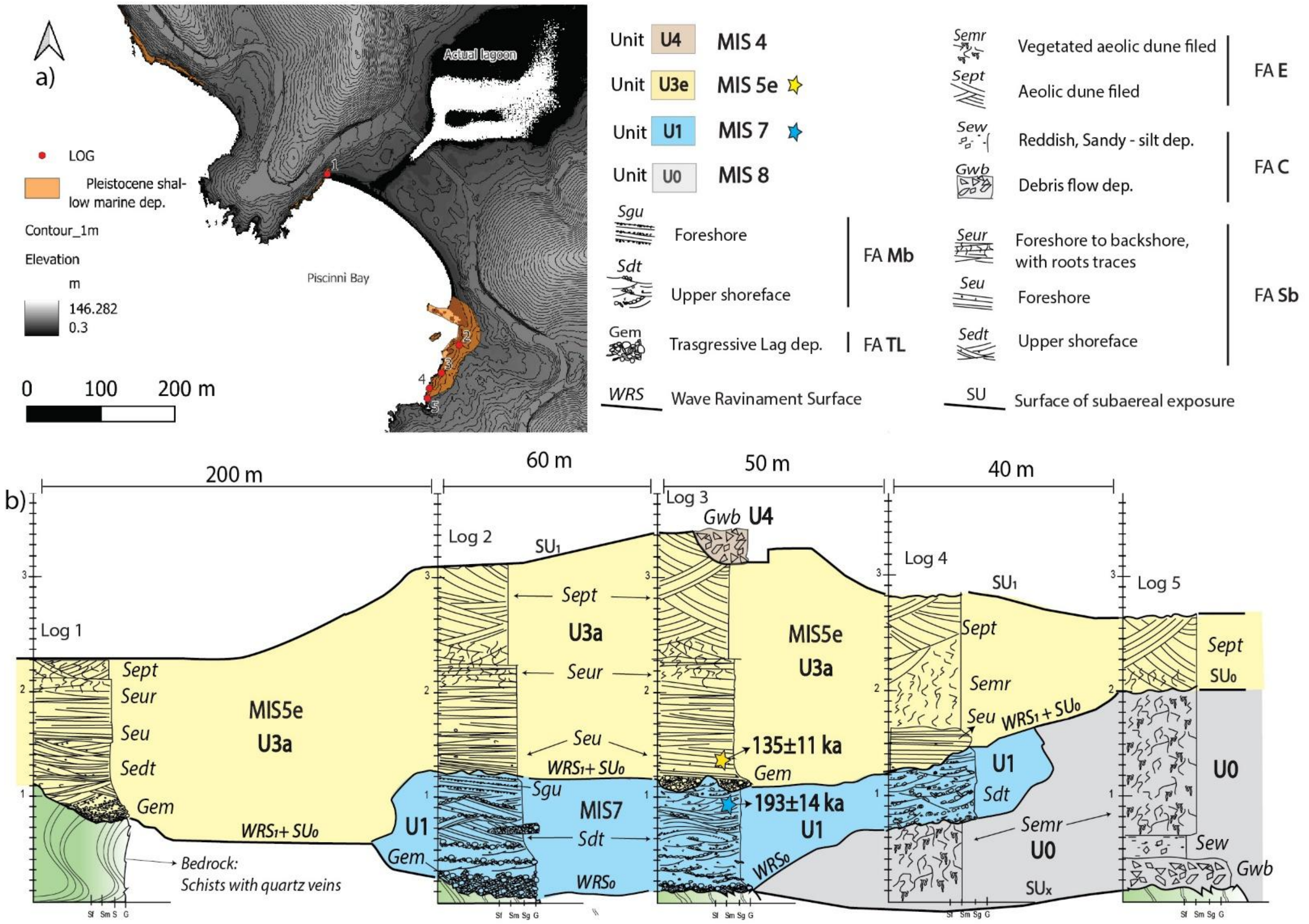

Figure 5. *(a) Map of the Piscinnì area showing the position of measured logs within the studied Quaternary deposits. (b) Measured field logs with stratigraphic correlations. Stars indicate the position of dated samples, and bold numbers their ages. Italic letters indicate the facies described in the text, Table 1 and Figure 2.*

Finally, the luminescence age of 193 ± 14 ka allows to refer U1 to the interglacial Marine Isotopic Stage MIS7 (245–190 ka). Unit U3a crops out along most of the bay and is dominated by a discontinuous basal sandy-conglomerate transgressive lag that grades into a shallowing-upward sandy beach system (from upper-shoreface to coastal dunes; facies associations TL, Sb, E, Fig. 5). The basal unconformity (WRS_1+ SU_0) cuts the bedrock U1 and/or U0 bodies, representing the interplay between two subsequent erosional surfaces triggered by different mechanisms. In particular, the SU_0 erosional surface bounds two different dune complexes referred to units U0 and U3a, marking a prolonged phase of subaerial exposure associated with sea regression (*sensu* Zecchin et al., 2019). On the contrary, the WRS_1 surface unconformably bounds marine deposits of units U1 and U3a. Thus, WRS_1 represents a wave ravinement developed during a sea transgression (*sensu* Zecchin et al., 2019). Overall, basal unconformity (WRS_1+ SU_0) is interpreted as a composite surface (*sensu* Nalin et al., 2007; Sechi et al., 2022). Finally, U3a, based on the luminescence age (135 ± 11 ka), is associated with the last interglacial stage MIS 5e (136-116 ka).

The sedimentological differences between the U1 and U3a beach systems highlight a marked shift in sediment budget, with greater sand availability during MIS 5e, likely driven by enhanced biogenic carbonate production.

The uppermost unit (U4) consists of thin debris-flow deposits and is bounded at the base by an erosive surface (SU_1) deeply cut through the underlying U3a. Surface SU_1 is interpreted as a subaerial exposure associated with a sea regression that occurred possibly during the last glacial periods (MIS 4-2; post 80 ka).

4.3.2 Nora

The studied sequence unconformably rests on the bedrock and is represented by a single unconformity-bounded unit U3a (Fig. 6). Unit U3a reaches a maximum thickness of ca. 4 meters and consists of a discontinuous conglomeratic transgressive lag strata overlain by a well-developed upper-shoreface deposits of the mixed sandy-gravelly beach system (facies associations TL and Mb; Fig. XX). The surface WRS_1 unconformably separating the bedrock and the shallow marine strata of unit U3a is interpreted to represent a wave ravinement developed during a sea transgression (*sensu* Zecchin et al., 2019). Finally, the luminescence ages of 143 ± 7 ka and 127 ± 5 ka (average 135 ± 8 ka) allow to refer Unit U3a to the interglacial stage MIS 5e (136-116 ka, Fig. 6; Tab. 2). The conglomeratic component is dominated by *rhodolith* cobbles to granules, with a minor amount of rounded volcanic clasts. The occurrence of *rhodoliths* within bar and trough cross-stratification indicates longshore currents and *rhodolith* input reworked by wave action. The *rhodoliths,* together with the high fossiliferous content, again highlight enhanced biogenic carbonate productivity during MIS 5e interglacial.

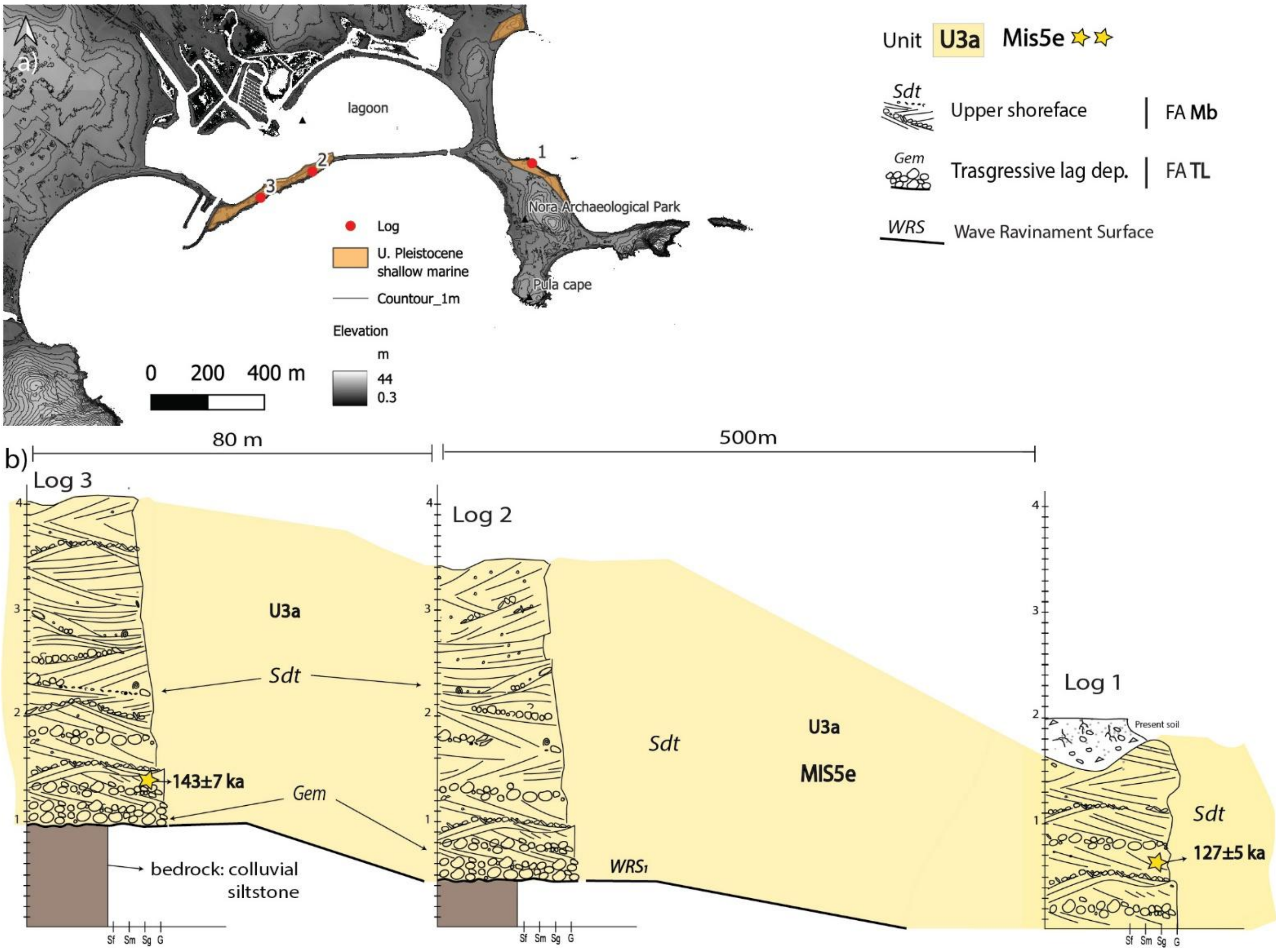

Figure 6. *(a) Map of the Nora area showing the position of measured logs within the studied Quaternary deposits. (b) Measured field logs with stratigraphic correlations. Stars indicate the position of dated samples, and bold numbers their ages. Italic letters indicate the facies described in the text, Table 1 and Figure 3.*

4.3.3 Torre Foxi

The complete coastal sequence crops out for about 500 m and are grouped into three UBSUs: U3a, U3a$_1$ and U3b (Fig. 7). The lower Unit U3a consists of a 1.5 m thick maximum coral *Cladocora caespitosa (scleractinian, hexacoral)* boundstone resting on a cobbly-pebbly transgressive lag deposit (facies association TL, Fig. XX). At the top unit U3a is occasionally eroded (SU$_1$) and mantled by a colluvial/soil deposit dominated by boulders of fragmented coral boundstone. Thus, the erosive surface SU$_1$ is interpreted to represent an important phase of subaerial exposure. Unit U3a, based on the luminescence (135 ± 5 ka) and U/Th ages (143 ± 5 and 129 ± 6 ka), is referred to the interglacial stage MIS 5e (136–116 ka; Tab. 2). The occurrence of coarse sand and pebbles within these deposits indicates intermittent terrigenous input during reef development. Reef growth also involved abundant crustose coralline algal binders (Fig. 7).

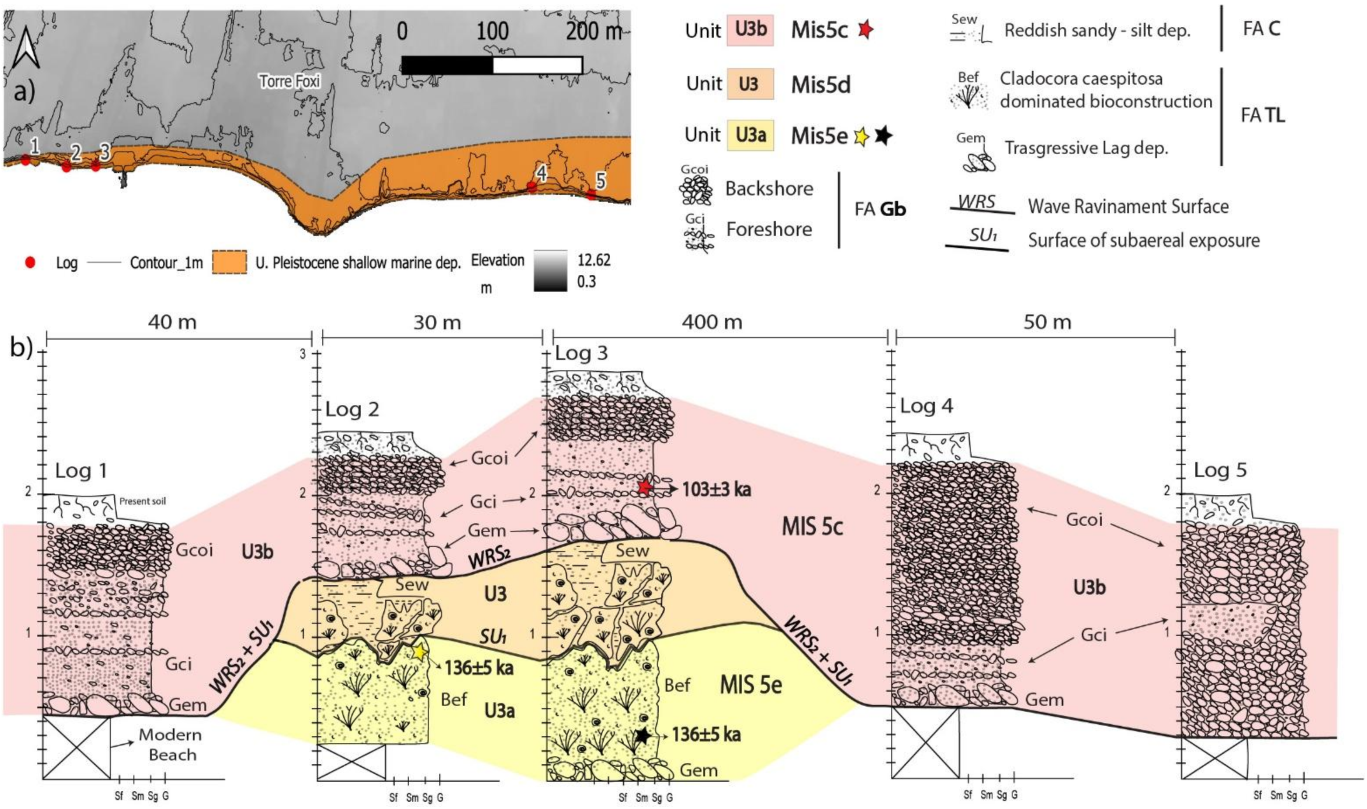

Figure 7. *(a) Map of the Torre Foxi area showing the position of measured logs within the studied Quaternary deposits. (b) Measured field logs with stratigraphic correlations. Stars indicate the position of dated samples (black one indicating U/Th age), and bold numbers their ages. Italic letters indicate the facies described in the text, Table 1 and Figure 4.*

The overlying Unit U3b, reaching a maximum thickness of 2.5 m, comprises a transgressive conglomeratic lag grading into a gravelly beach system succession (Facies Association TL and Gb, Fig. 7). The erosive surface (WRS_1), cut on deposits of unit U3a, represents a wave ravinement developed during the sea transgression (*sensu* Zecchin et al., 2019). The gravelly beach deposits grade upward from the dipping seaward sandy-pebbly layer of the foreshore to massive imbricated conglomeratic backshore deposits (ordinary and storm berms, respectively; sensu Pascucci et al., 2008). Finally, U3b, based on the luminescence age of 103 ± 3 ka is correlated with the MIS 5c (105-95 ka; Fig. 7).

4.4 Paleo relative sea-level (RSL) estimates

RSL estimates for Quaternary coastal deposits have been widely reported in the literature on the basis of geomorphic, sedimentary and biological sea-level indicators (e.g., Camoin & Webster, 2015; Rovere et al., 2016a; Vacchi et al., 2016; Muhs, 2022). Here, they are presented for the study sites without direct correction for glacial isostatic adjustment (GIA) and compared with previously published data from Sardinia. The derived RSL elevation for MIS 7 marine deposit at the study area is 3.5 ± 1.5 m above present sea level (apsl), which is similar, even slightly higher than the sea marker reported for W and NW Sardinia (0.6 ± 1 m, 2.9 ± 0.2 m; Cocco et al., 2019; Casini et al., 2020).

The MIS 5e sea level markers for the study sites are 0.7 ± 1.3 m apsl (Piscinnì), 4.7 ± 2.5 m apsl (Nora) and 4.6 ± 2.0 m apsl (Torre Foxi). The MIS 5e sea level marker derived RSLs from the central and west side of the study area (Nora, Torre Foxi) are in perfect agreement with previous data derived for S Sardinia (cala Mosca; 5 ± 1 m) and similar, even though slightly higher than the average of W/NW Sardinia (3.3 ± 0.6 m); whereas the MIS 5e data at the easternmost study site (Piscinnì) is clearly lower than expected (Sechi et al 2022).

Finally, the MIS 5c sea level marker is present only at the easternmost study site (Torre Foxi) with a derived RSL value of 1.3 ± 1.3 m apsl, which is slightly lower than the average sea level marker reported for W/NW (2.15 ± 0.9 m) and clearly lower for Cala Mosca (S Sardinia; 5.8 ± 1 m; Sechi et al., 2022).

5. Discussion

5.1 Tectonic implications of composite marine terraces

The sedimentary successions studied along the southern Sardinian coasts are characterized by five unconformity-bounded units (U1, U2, U3a, U3b and U4), recording repeated phases of marine transgression, beach-system progradation and sea regression during the middle-Late Pleistocene. The stratigraphic architecture documents the superposition of distinct shallow-marine units separated by complex erosive surfaces associated with transgression (ravinement) and subaerial exposure, forming composite marine terrace sequences, *sensu* Sechi et al. (2022). At the Piscinnì site, units U1 and U3a form a composite marine terrace developed on Palaeozoic bedrock, recording the MIS7 (245–190 ka) and MIS 5e (136–116 ka) highstands. At Torre Foxi site, units U3a and U3b define a composite marine terrace associated with the MIS 5e highstand (136–116 ka) and the subsequent MIS 5c stillstand (105-95 ka). In contrast, at Nora site, a single shallow marine unit corresponding to the MIS 5e (136–116 ka) highstand is preserved.

Composite marine terraces formed by MIS 5c gravelly, mixed, and sandy beach deposits that overlie MIS 5e shallow-marine units are widely documented along the Sardinian coast (Andreucci et al., 2010; Pascucci et al., 2014; Sechi et al., 2018, 2020, 2022; Zucca et al., 2014). Conversely, MIS 7 marine deposits preserved above present sea level are rarely reported in Sardinian sedimentary successions (Andreucci et al., 2009; Casini et al., 2020). Notably, to our knowledge, this study identified, for the first time, a composite marine terrace formed by the superposition of MIS 7 and MIS 5e marine deposits. These findings indicate that composite marine terraces are not isolated occurrences but represent a recurrent feature along the Sardinian coast. The elevations of the studied shallow-marine units relative to the present-day sea level (RSL) do not match the worldwide accepted eustatic sea-level estimates (MIS 7 −20 to −10 m below sea-level; MIS 5e +6 to +9 m above sea-level, and MIS 5c −25 to −15 m below sea-level; Spratt & Lisiecki, 2016; updated to 2025; Tab. 4; Fig. 8). In particular, the observed elevations of MIS7 (3.5 ± 1.5 m apsl) and MIS5c (1.3 ± 1.3 m apsl) beach deposits cannot be explained solely by late Quaternary sea-level fluctuations, as a tectonically stable, slightly subsiding area such as Sardinia has often been assumed to be (i.e. Ferranti et al., 2006; Lambeck et al., 2011). Multiple mechanisms may account for this discrepancy, such as poorly defined MIS7 and MIS5c elevations at the global scale, or the contribution of glacial isostatic adjustment (GIA) in the Mediterranean region. Although uncertainties persist in global eustatic curves, errors of this magnitude (15-20 m) are highly unlikely given the overall consistency among available reconstructions (e.g., Waelbroeck et al., 2002; Dutton and Lambeck, 2012; Spratt & Lisiecki, 2016; Creveling et al., 2017; Muhs et al., 2026). Likewise, although GIA may have influenced sea level since the Middle–Late Pleistocene, its total contribution remains uncertain (Rovere et al., 2016; Vacchi et al., 2018). The maximum GIA effect estimated for a far-field area such as Sardinia is only ~2–2.5 m during the Last Interglacial (Stocchi et al., 2018), markedly smaller than the 15-20 m mismatches observed in southern Sardinia between the reconstructed relative sea level (RSL) and the eustatic benchmarks. Our data show that, even within the full range of sea-level uncertainties, no model based on constant vertical motion and accepted eustatic benchmarks can satisfactorily reproduce the observed elevations of shallow-marine deposits along the Sardinian coast. These discrepancies, therefore, point to a dominant tectonic control rather than a purely eustatic or GIA-driven signal, implying uplift of southern Sardinia crustal blocks since at least the Pleistocene (Tab. 4; Fig. 8). This interpretation is also consistent with a recent geophysical model suggesting regional uplift of the Corsica–Sardinia Block since the Pleistocene, likely enhanced by a lower-crustal mass deficit (Cocco et al., 2024).

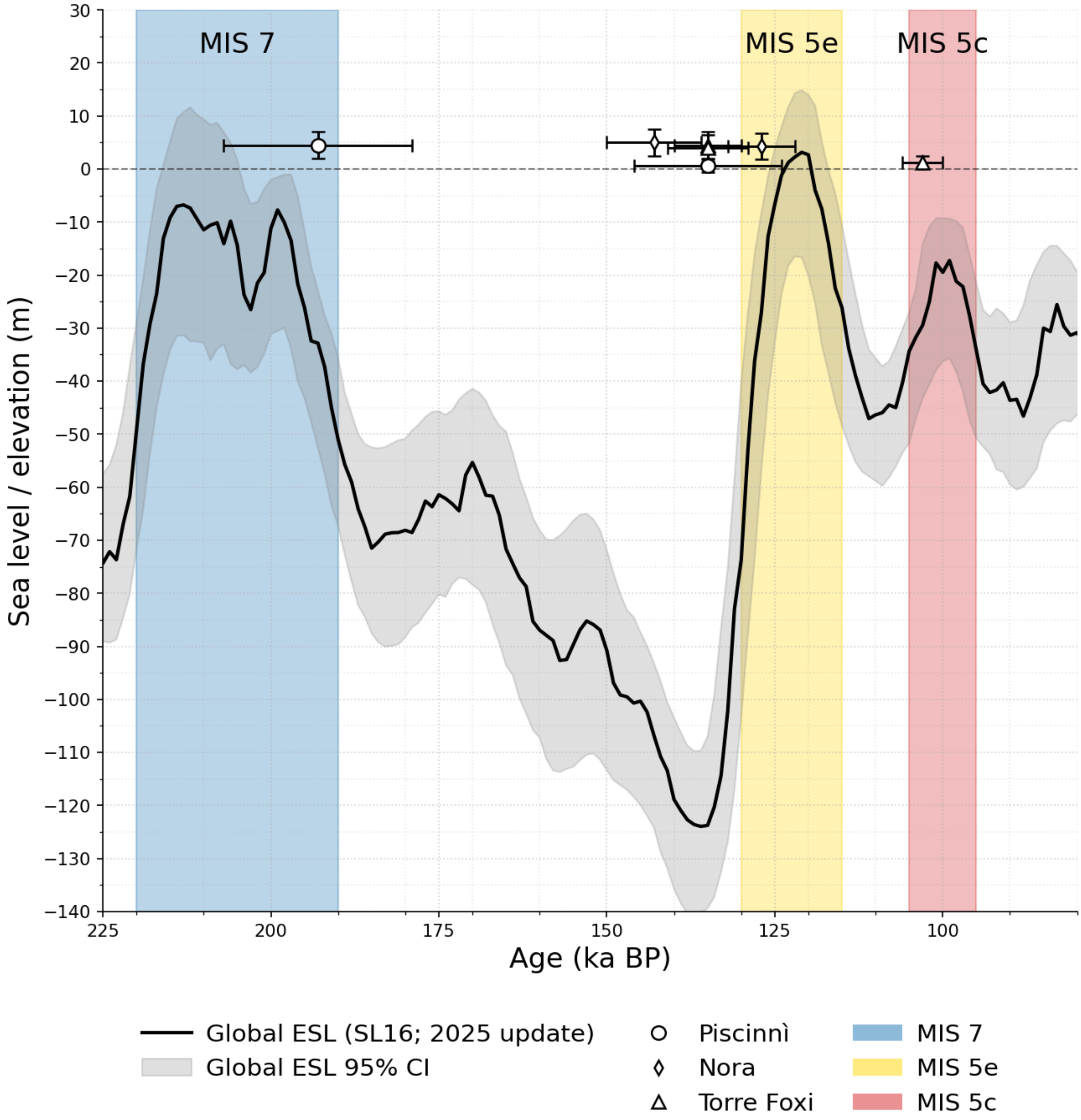

Figure 8. *Global eustatic sea-level (ESL) curve from the Spratt and Lisiecki stack (2016; 2025 update, short PC1) with 95% confidence interval, compared with reconstructed relative sea-level (RSL) markers from the southern Sardinian coast. Error bars on local markers represent age uncertainty (x-axis) and elevation uncertainty (y-axis). Shaded vertical bands indicate the time windows of MIS 7, MIS 5e, and MIS 5c. Different symbols denote the three study sites (Piscinnì, Nora, and Torre Foxi), highlighting the mismatch between globally inferred ESL positions and the present elevations of the shallow-marine deposits.*

However, whether regional uplift rates are uniform or variable in time and space remains difficult to assess, most likely because, previous studies were based on isolated Quaternary successions from individual coastal sectors without a regionally integrated stratigraphic framework (Andreucci et al., 2009, 2010a; Buttau et al., 2011; Pascucci et al., 2014; Cocco et al., 2019; Casini et al., 2020; Sechi et al., 2022). This study presents, for the first time, a stratigraphic correlation at regional scale across a 50-km-long study area of marine terraces formed over the last ~200 ka. Stratigraphic architecture varies markedly between studied sectors, with both composite and non-composite marine terraces of different ages (Table 2; Figs. 5, 6, 7). Together with the contrasting RSL elevations, this stratigraphic variability indicates that the margin did not evolve as a single tectonically coherent block during the Late Quaternary. The distribution of these marine units above present-day sea level provides clear evidence of crustal segmentation and differential vertical uplift rates among adjacent coastal blocks in southern Sardinia (Figs. 1, 8). In particular, five adjacent main fault-bounded blocks can be identified along the study areas (see figure 1b for block locations and names). The presence of the youngest preserved shallow-marine unit (U3b, MIS5c) on the Molentargius block, may suggest a progressive eastward migration of uplift through time.

Overall, these observations suggest that the classic model of marine terrace staircase development under uniform uplift of unfaulted crustal blocks is the exception rather than the rule. Instead, the data support a model of multiple fault-bounded blocks dominated by spatially and temporally variable uplift rates, generating differential accommodation space and complex stratal stacking patterns. In this context, the interaction between differential uplift rates and Quaternary sea-level fluctuations promotes the "re-occupation" phenomenon, whereby younger shallow-marine sequences may superpose older ones, leading to the development of composite marine terrace sequences.

6. Conclusions

The investigated coastal successions of southern Sardinia record repeated phases of marine transgression, beach-system progradation, and regression within unconformity-bounded stratigraphic units correlated with the highstands of MIS 7, MIS 5e, and MIS 5c. The three study sites display contrasting stacking patterns: the Piscinnì site preserves a MIS 7/MIS 5e composite marine terrace sequence; Nora records only the MIS 5e upper shoreface unit; and Torre Foxi preserves a MIS 5e/MIS 5c composite marine terrace sequence. These observations indicate that composite marine terraces are a recurrent feature along the south Sardinian coast. The spatial distribution of these composite and non-composite marine terrace sequences cannot be explained solely by glacio-eustatic sea-level fluctuations and instead points to a dominant tectonic control. Specifically, the data support a model in which southern Sardinia is segmented into distinct crustal blocks affected by spatially and temporally variable uplift since at least the Middle–Late Pleistocene. In such tectonically segmented settings, even modest uplift rates can generate complex depositional architectures, in which successive highstand units are separated by unconformities and re-occupation processes, rather than forming simple staircase sequences tied to individual uniform uplifting blocks.

Composite marine terrace sequences, when analysed within an integrated stratigraphic and chronological framework, represent a powerful tool for reconstructing the interaction between sea-level fluctuations and vertical crustal movements, thereby providing a robust framework to decipher subtle tectonic signals in regions traditionally considered tectonically stable.

Chapter 2

Field trip guide to the geological evolution of the Sal'e Porcus saline pond (northern Sinis Peninsula, western Sardinia)

Giovanni Fantini[1], Ilaria Nobile[1], Stefano Andreucci[1], Maria Teresa Melis[1]

[1]*Department of Chemical and Geological Sciences, University of Cagliari, 09042 Monserrato. Italy*

To be submitted to the peer-reviewed journal *Geological Field Trips and Maps*.

Field trip guide to the geological evolution of the Sal'e Porcus saline pond (northern Sinis Peninsula, western Sardinia)

Giovanni Fantini[1], Ilaria Nobile[1], Maria Teresa Melis[1], Stefano Andreucci[1]

[1]*Department of Chemical and Geological Sciences, University of Cagliari, 09042 Monserrato. Italy*

1. Introduction to the field trip

Sal'e Porcus pond is the largest natural salt flat in Europe, located on the central-western coast of Sardinia (Fig. 1), and covers an area of about 3.3 km². This coastal basin records a complex evolution that reflects the combined effects of regional tectonic activity, sea-level fluctuations and coastal sedimentary processes. The surrounding sedimentary succession spans from the Oligo-Miocene, including deposits related to the Messinian Salinity Crisis (MSC), through the Pliocene transgression and up to Pleistocene and Holocene coastal deposits.

This field trip retraces the main stages of the geological evolution of the northern Sinis Peninsula in order to understand the key processes that led to the development of the Sal'e Porcus basin. Particular attention is given to the sedimentary infill of the basin, which is most likely related to Holocene sea-level rise. Evidence from the Sal'e Porcus core provides important insight into its final closure and present-day configuration which appear to have been controlled mainly by Late Holocene coastal dynamics, including sediment supply, high-frequency sea-level fluctuations, and wind- and wave-driven sediment transport. These features make Sal'e Porcus an excellent natural archive for reconstructing the long-term interaction between sea-level change, tectonics, and coastal morphodynamic evolution.

2. Geological setting of the Sinis Peninsula

Sardinia is the largest island in the western Mediterranean basin, and its present-day position is the result of a late Cenozoic geodynamic evolution. The Oligocene–early Miocene eastward migration of the Apennines subduction zone induced an important rifting phase affecting the Corsica-Sardinia lithospheric block (ca. 24–15 Ma; Fig. 1a), which drifted from the southern Europe continental margin to its present-day position in the central western Mediterranean Sea (Doglioni et al., 1998). During the Plio–Quaternary, Sardinia experienced a further tectonic segmentation due to an extensional regime associated with the opening of the southern Tyrrhenian basin (Casula et al., 2001; Cocco et al., 2013). This tectonic activity led to the development of the Campidano Basin, a NW–SE oriented lithospheric-scale depression filled by more than 1500 m of Miocene to Quaternary volcanosedimentary succession (Murru, & Ulzega, 1978a; Cherchi & Montadert, 1982; Cherchi et al., 2008). Subsequently, the island experienced widespread volcanic activity and regional tectonic uplift, which persisted until the late Pleistocene (post 70 ka BP; Carmignani et al., 2016; Cocco et al., 2019; Sechi et al., 2022).

The Sinis Peninsula, located on the central-western coast of the island, represents the north-western shoulder of the Campidano Basin and is detached from it by the Sinis fault (Fig. 1b). Indeed, the Sinis block is a structural high bounded by two Pliocene normal faults roughly E-dipping, that separate it from the Mal di Ventre and Catalano islands to the west and the Campidano Basin to the east (Fais, Klingele, & Lecca, 1996; Lecca, 2000; Casula et al., 2001; Cocco, Funedda, Patacca, & Scandone, 2013; Cocco et al., 2019). Nowadays, Sardinia is a semi-stable low-seismicity continental fragment with clear evidence of slight late Pleistocene–Holocene tectonic activity, as normal faults and local uplift highlighted (Cocco et al. 2019; Casini et al. 2020; Sechi et al., 2022). Together, all these processes have shaped the present-day geomorphological and structural framework of Sardinia, including the Sinis Peninsula.

3. Lithostratigraphic units around Sal’e Porcus saline pond

The Sinis area is characterized by ten sedimentary lithostratigraphic units (formations) with distinct paleoenvironmental and structural significance (Fig. 2). In the northern sector of the peninsula, around the Sal’e Porcus saline pond, seven of these formations are observable, dominated by marine to coastal carbonate and siliciclastic deposits spanning in time from middle Miocene to Holocene (Fig. 2, 3; Cherchi et al., 1978; Cherchi & Martini, 1981). The basal Miocene (Tortonian–Messinian) succession comprises, from base to the top, the Capo San Marco Formation (SMR), the Calcari Laminati del Sinis Formation (Sinis Laminated limestones; CLS), and the Calcari di Torre del Sevo Formation (Torre del Sevo limestones; CTS) (Fig. 3; Cherchi, Marini, Murru & Robba, 1978b). This sedimentary sequence consists of alternating marlstones, sandstones, and limestones, reflecting variable depositional environments within a shallow-marine ramp-to-platform system.
At the end of the Miocene, the Mediterranean basin was affected by a severe phase of subaerial exposure associated with the so-called Messinian Salinity Crisis (MSC). The MSC was driven by a severe water budget deficit linked to the closure of connections with the Atlantic Ocean on the west and with the Paratethys to the east around 5.97 Ma (Vasiliev et al., 2017). This enigmatic event lasted about 600 kyr (5.97 to 5.33 Ma) and resulted in the deposition of evaporites (gypsum and halite) up to 2 km thick across the Mediterranean basin, possibly associated with a sea-level drop of about 1500 m. However, the paleoenvironmental conditions and the final desiccation phase remains debated

(Vasiliev et al., 2017). The unconformity associated with this subaerial exposure is regionally expressed at the Mediterranean scale and is also clearly observable in the Sinis Peninsula, where a widespread erosive surface truncates the Miocene shallow-marine succession.
A marine transgression following the MSC led, at the onset of the Pliocene, to the widespread deposition of a shallow-marine to platform sequence across the Mediterranean basin. In the northern Sinis Peninsula, the Pliocene sedimentary sequence is characterized by foraminifera-rich coastal sandy limestones of the Calcari di Mandriola Formation (Mandriola limestones; CM), overlain by the thick aeolian sandstones of the Capo Mannu Formation (CMU; Fig. 3), which possibly extend into the Pleistocene.

The Quaternary sedimentary sequence of the Sinis area consists of shallow-marine sandstones, coastal dunes and colluvial deposits spanning from MIS 7 (~190 ka) to MIS 4 (~75 ka; Andreucci et al., 2009). Shallow-marine sandstones, occurring at elevations between 0 and 9 m above present sea level, are widely cropping out along the coastlines and are most likely associated with Marine Isotope Stage (MIS) 5e (ca. 125 ka), recording the Last Interglacial, when sea level was approximately 7 m above the present. In particular, along the coast surrounding the Sal'e Porcus saline pond, well-developed high-angle cross-stratified dunes grade laterally and vertically into multiple generations of variably reddened aeolian sandstones, weakly cemented marsh silts bearing pulmonated gastropods, as well as calcareous crusts of evaporitic origin and pedogenic calcretes (Carboni et al., 2002). Together, these deposits record alternations of coastal and continental depositional processes active during the Pleistocene.

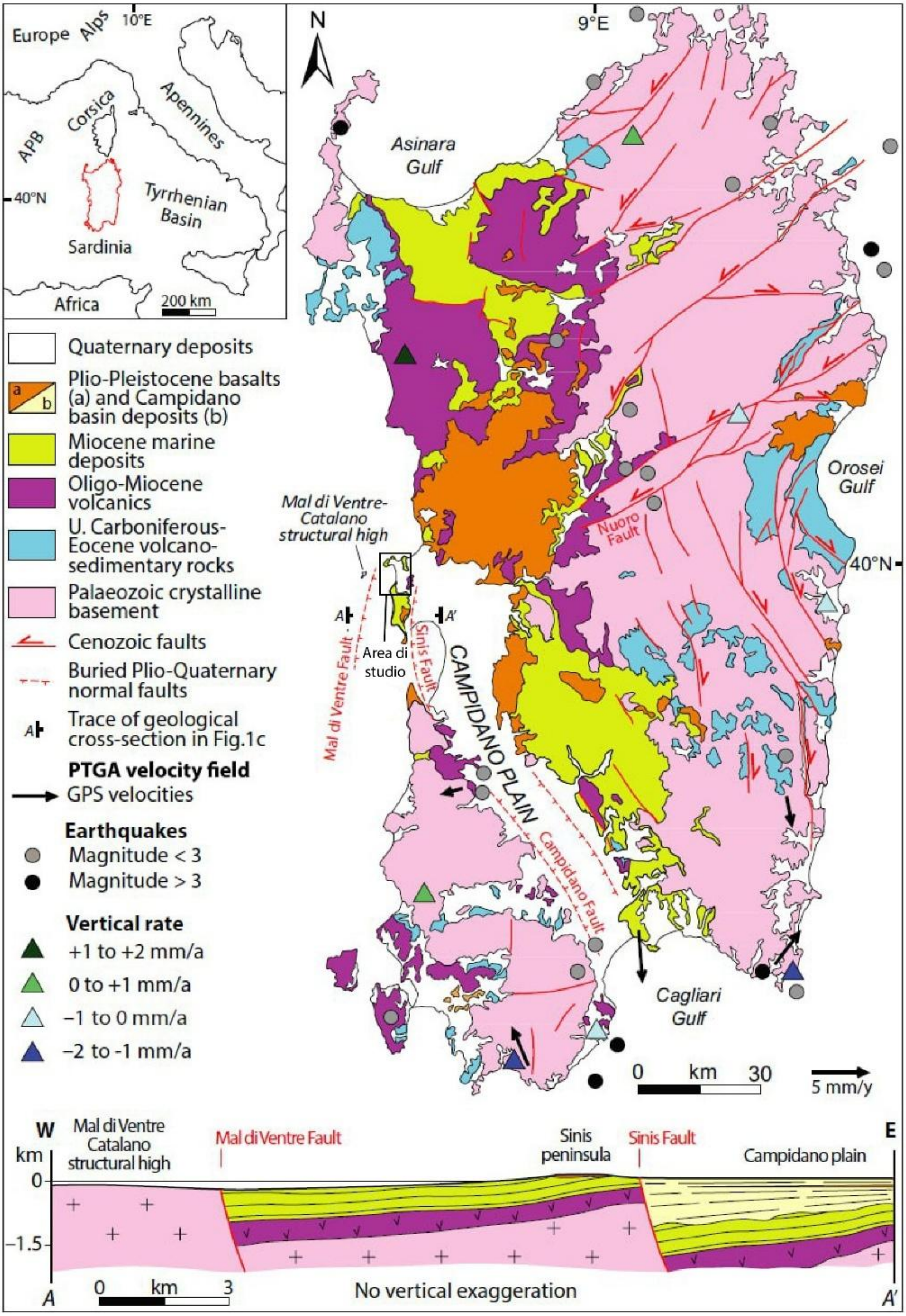

Figure 1. *Geological map of Sardinia modified from Cocco et al., 2019.*

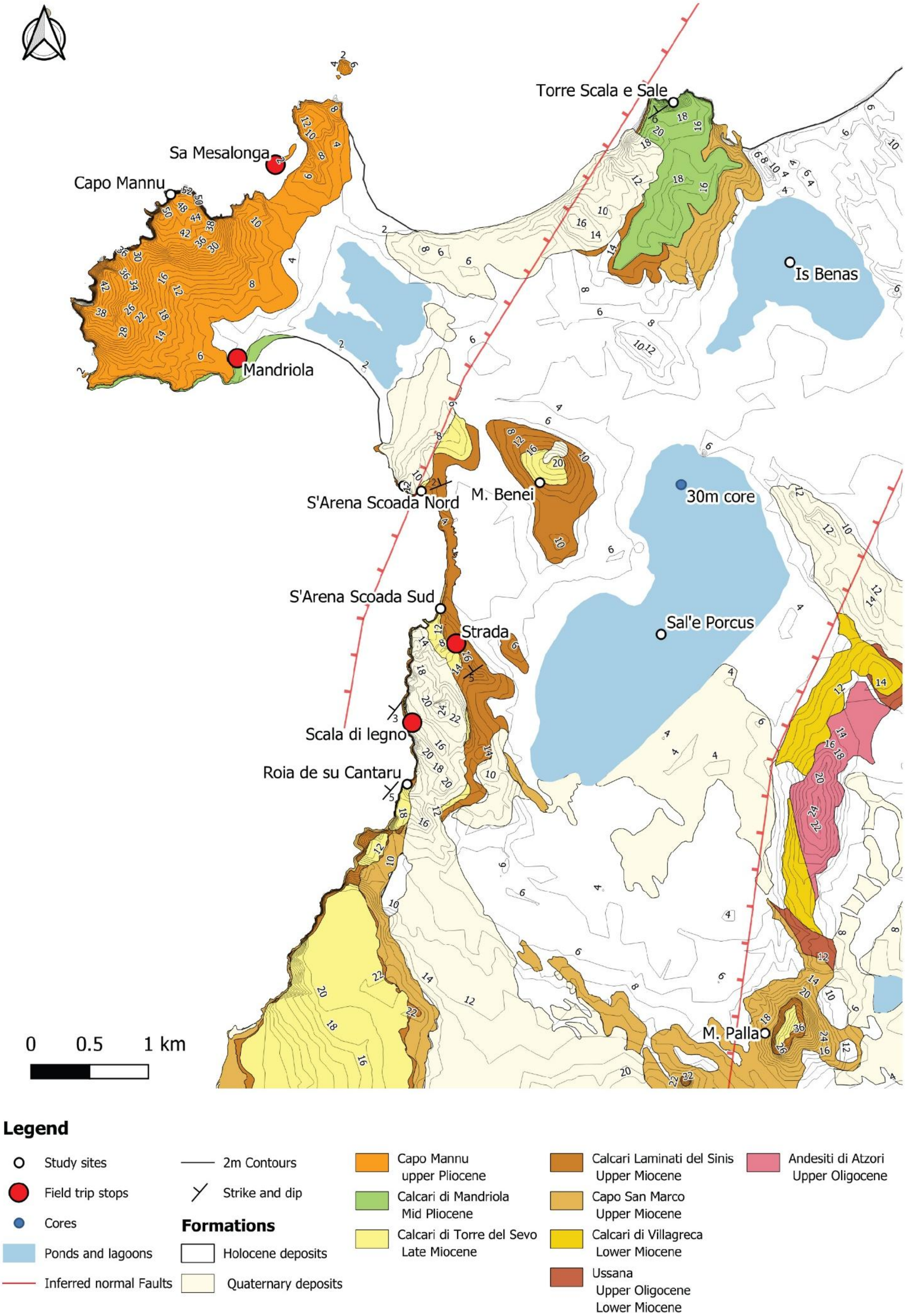

Figure 2. *Geological sketch map of the northern Sinis peninsula.*

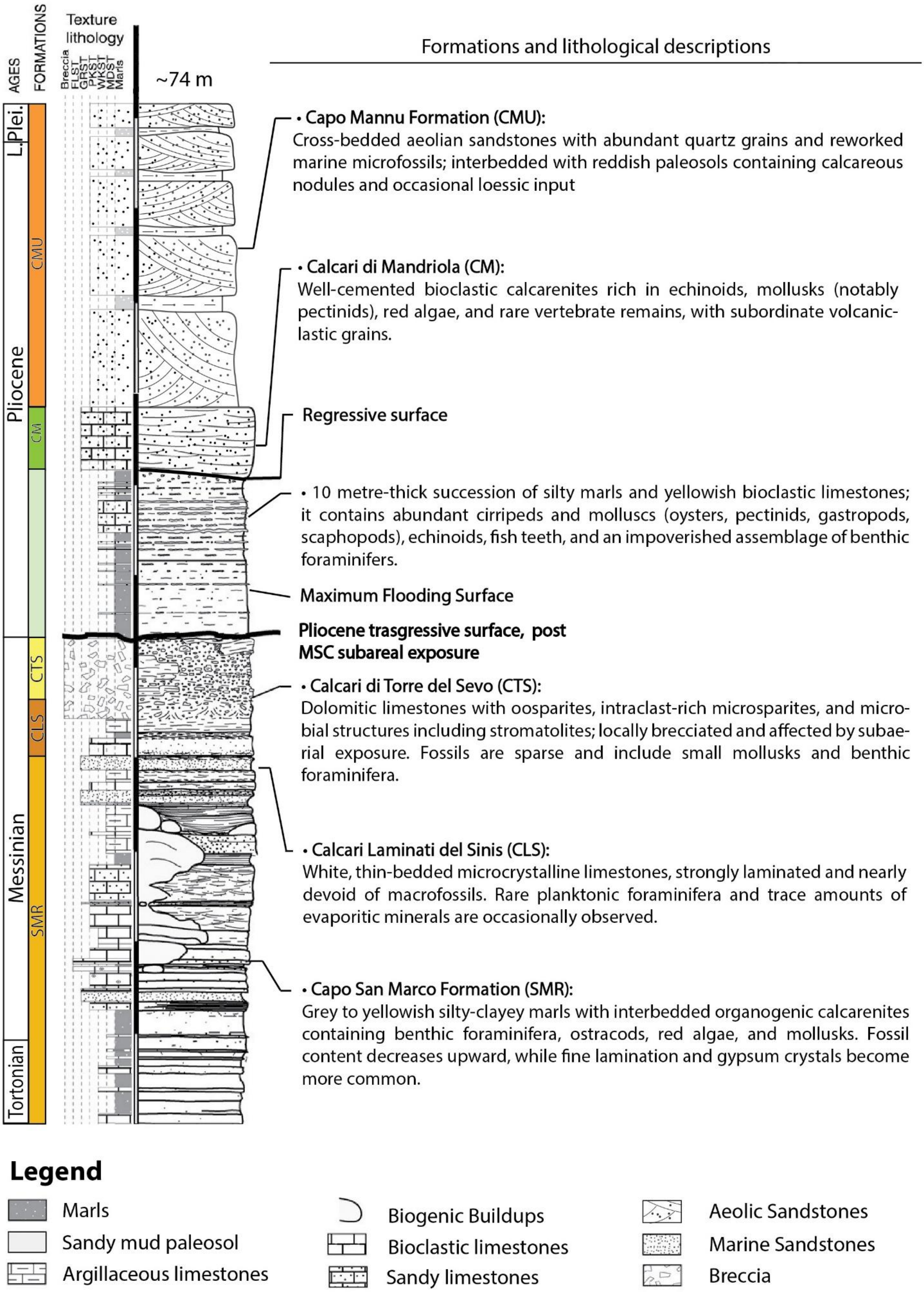

Figure 3. *Comprehensive Upper Miocene to Pleistocene sedimentary succession of the northern Sinis Peninsula; modified from Cornèe et al., 2008.*

4. Field trip study sites

Stop 1 – Roja de Su Càntaru (La Scala)

Panoramic view of the Upper Miocene sedimentary sequence. Overall, this site highlights the gradual shift from a sublittoral, open-marine environment to progressively more restricted lagoonal and marginal-marine settings during the Tortonian-Messinian. At the base, the Capo San Marco Formation (SMR) marly strata reflect low-energy, subtidal marine conditions with normal salinity. These are overlain by the CLS limestones (Calcari Laminati del Sinis Formation), most likely developed in a restricted, hypersaline, shallow-marine or large lagoonal setting with limited connection to the open sea. The CTS limestones (Calcari di Torre del Sevo Formation) record a shift to a shallow, periodically emergent peritidal environment typical of a coastal flat, where episodic marine ingressions alternated with phases of subaerial exposure. This upward evolution reflects a regressive trend and increasing environmental restriction, culminating in the subaerial exposure at the onset of the Messinian Salinity Crisis (MSC).

Figure 4. *Upper Miocene (Tortonian-Messinian, 10-5.9 Ma) sedimentary succession along the western coast of the Sinis peninsula; note SMR formation thin bedded gray basal marls; colored lines mark the boundaries between formations.*

Stop 2 – La Strada

At this stop, the previously Messinian succession can be observed in detail. In particular, CLS limestones are dominated by inner-carbonate-shelf or paralic deposits linked to reduced circulation and/or limited marine connectivity. The CLS strata display better-developed laminations and lack significant faunal content. The overlying CTS bodies exhibit a stronger diagenetic overprint, including dolomitization, as well as clear evidence of subaerial exposure, such as brecciation and pedogenic alteration. The transition from the CLS strata to the CTS bodies reflects an evolution from chemically precipitated inner shelf or lagoonal carbonates to bioclastic shoals and microbialites, punctuated by multiple subaerial exposure. The occurrence of ooid-rich facies within the CTS suggests episodic marine ingressions that provide the hydrodynamic conditions necessary for ooid formation in temporarily reconnected shallow-marine settings. The progressive shift from a-biotic, sterile, chemically precipitated carbonates to reworked, brecciated and pedogenized microbial limestones reflects increasing continental influence, consistent with a regressive–arid trend during the late Messinian.

Figure 5. *Messinian (ca. 7-6 Ma) sedimentary succession with CLS displaying well-developed planar-like centimetric strata overlined by ooid-rich facies within the brecciated CTS limestones; colored line mark the boundaries between formations.*

Stop 3 – Mandriola

This stop shows the CM limestones (Calcari di Mandriola Formation) overlying the brecciated and karstified Messinian deposits and represents a transgressive-to-highstand phase of Pliocene age. Thus, this unconformity represents the post-Messinian flooding event and the re-establishment of coastal marine systems characterized by energetic wave-dominated sedimentation. These marine calcarenites were deposited in a high-energy shoreface setting and contain abundant marine shells, including echinoids and bivalves (including pectinids), as well as fragments of red algae. Occasional terrestrial input, including vertebrate remains and volcaniclastic clasts, is also recorded. The CMU deposits (Capo Mannu Formation) overlying CM marine unit, record a subsequent shift to continental conditions, expressed by large-scale aeolian dune systems alternated by reddish paleosols.

Figure 6. *Lower Pliocene (ca. 5-4 Ma) sedimentary successions, a) CM shoreface and b) basal CMU aeolian deposits; colored lines mark the boundaries between formations; colored lines mark the boundaries between formations.*

Stop 4 – Capo Mannu cliff (Sa Mesa Longa)

At this site, the Capo Mannu Formation unit reaches a thickness of about 50 m and comprises five majors high-angle, large-scale cross-bedded sandstone units. These represent large dune bodies migrating over reddish paleosols or interdune areas oriented according to prevailing NW winds. These aeolianites are locally well cemented and are made of reworked planktonic and benthic foraminifera sourced from older marine deposits. Interlayered within the aeolian units are four well-developed paleosol horizons—reddish-brown "red soils" characterized by clay illuviation, carbonate nodules, and mature pedogenic features.

Overall, the succession records cyclic alternations between phases of active dune deposition and periods of soil-forming under more humid climatic conditions. This alternation preserves a detailed Middle–Late Pliocene to Early Pleistocene climatic archive, highlighting climate-driven shifts between arid and wetter periods. The transition from Pliocene shoreface environments (CM limestones) to fully continental dune systems (Capo Mannu Formation) marks a long-term relative regression and continentalization of the Sinis Peninsula.

Figure 7. *Upper Pliocene to lower Pleistocene (ca. 3-2 Ma) regressive dune fields and paleosoils sedimentary succession.*

5. Core description of the Sal'e Porcus saline pond

A 30 m-long core was collected at the northern margin of the Sal'e Porcus saline pond with the aim of characterising the Holocene deposits and better understanding the origin of the saline crusts (Fig. 2, 8). The core did not reach the bedrock. The lower interval, between ~30 and 7 m depth, consists of alternating sandy silt and clayey silt and rare dark mottling locally rich in bivalves (large pectinid) and foraminiferal shells (benthic and planktonic), with rare plant-charcoal fragments. At ~25 and 11 m depth, two horizons rich in centimetric gypsum crystals occurred. An erosional surface at ~7 m depth occurred, overlaying around 2 m of clayey deposits, showing clear evidence of oxidation (reddish colour). The upper part of the succession, instead, consists of alternating medium- to coarse-grained bioclastic sands with variable silt content, orange and black mottling, and a single pebble horizon. Upward, the sediment passes from dark-grey, medium-grained silico-bioclastic sand to progressively more yellowish, bioclastic-sand-dominated deposits with recurrent red mottling. The uppermost metre is characterized by clayey silt with orange mottling and a few thin layers of fine bioclastic sand. At the top, the succession culminates in a few centimetres of clay, capped by the modern surface saline crust.

6. Development of the Sal'e Porcus saline pond

The 30 m-long core collected at the northern entrance of the Sal'e Porcus saline pond is dominated by ~23 m of grey muds rich in foraminifera, scattered bivalves, and rare plant-charcoal fragments. These deposits can be interpreted either as coastal lagoon system or as hypersaline, very shallow water inner shelf. Horizons of gypsum crystals indicate episodic evaporation or supersaturation of the basin. The presence of well-formed gypsum crystals, together with variations in the relative proportion of clay and sandy silt, may reflect alternating phases of more open versus more restricted connectivity with the sea. The redness of the fine-grained deposits, along with a pronounced erosional surface, most likely defined a prolonged phase of subaerial exposure. At ~7 m depth, the core records a more renewed coastal/marine condition of the area, expressed by the transgressive barrier-related sandy strata. Above this surface, the succession consists of alternating sandy strata and silty-sandy to silty-clayey deposits, interpreted as back-barrier, lagoonal, and coastal-pond environments (Fig. 9).

If the ~23 m lower muddy interval was related to a Plio-Pleistocene marine transgression, some evidence of proximal shallow-marine, inner-shelf, or shoreface conditions would likely be preserved. In this respect, the occurrence of well-formed centimetre-scale gypsum crystals is difficult to

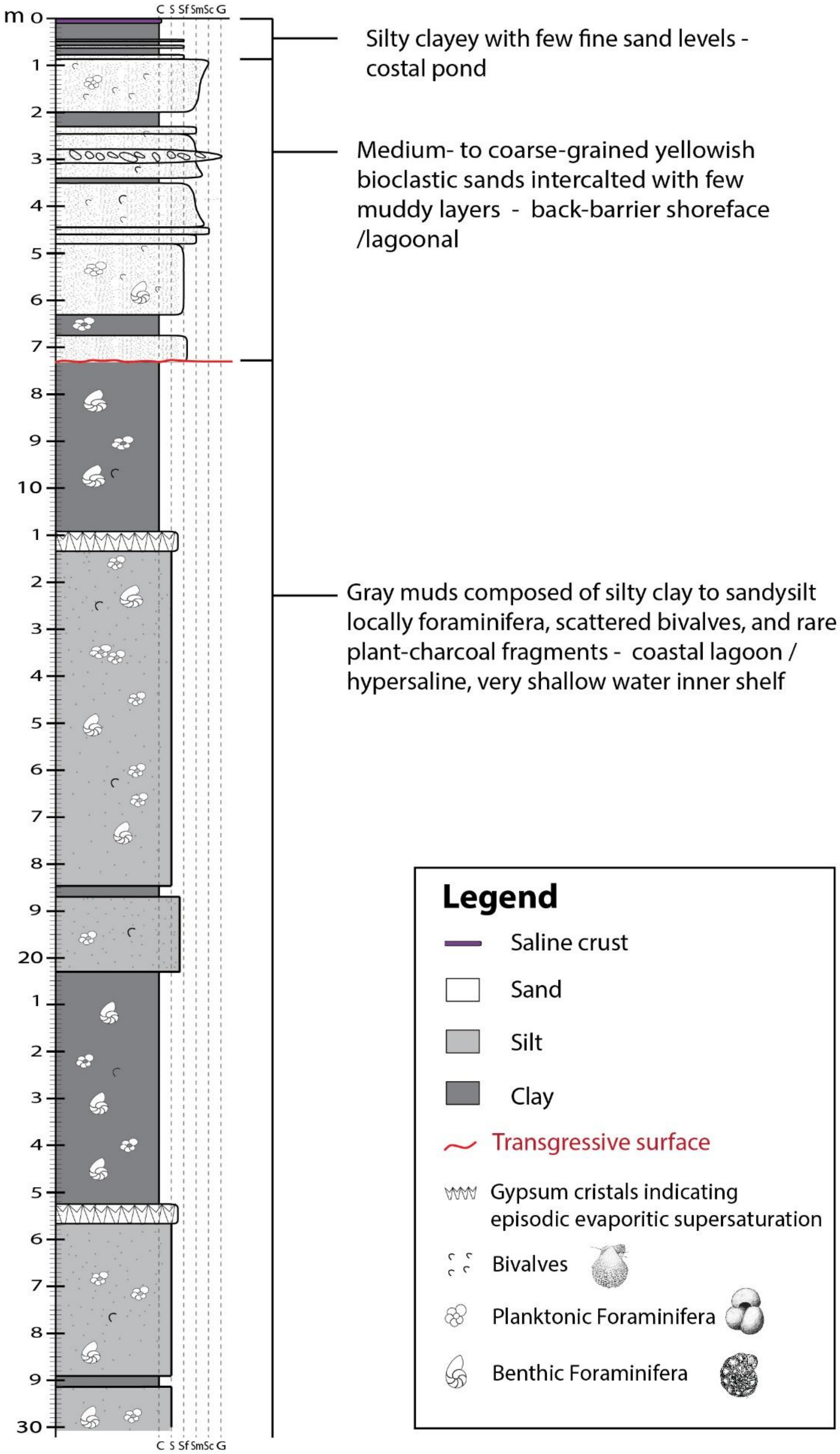

Figure 8. Log of the *30 m-long core collected at the northern entrance of the Sal'e Porcus pond.*

reconcile with such settings. Instead the clear evidence of prolonged subaerial exposure such as pedogenic alteration, oxidation, and erosional reworking can be referred to the Last Glacial Maximum phase, given that sea level was ~120 m lower than today.

Overall, the 30 m-thick core succession is more consistent with a late Quaternary history with its thickness reflecting the rapid infill of an accommodation-rich coastal basin. Accordingly, the transgressive barrier deposits may record a post glacial coastal evolution in which millennial- to centennial-scale sea level fluctuations dominate the Holocene evolution of the basin. The Sal’e Porcus pond likely formed during the Holocene rapid sea transgression as a lagoon backing a coastal cordon (beach-ridge system). Subsequently, during the highstand phase, coastal progradation shifted the coastal cordon to its present position, leading to the formation of the Is Benas lagoon and isolating the Sal’e Porcus pond.

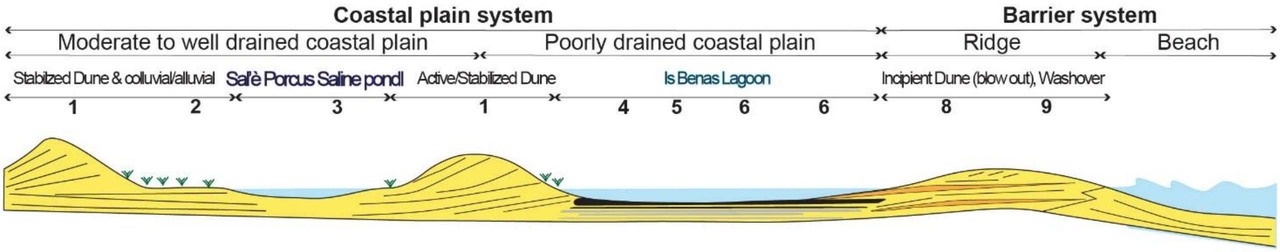

Figure 9. Sedimentological model of the studied core.

This Transgressive–Regressive (T–R) sequence is well documented in sedimentary wedges deposited of major Mediterranean coastal plains (e.g., Po, Tiber, and Ebro rivers). The transgressive phase persisted until the Holocene Climate Optimum (7–6.8 ka BP), followed by a highstand (normal regression) that continues to the present (e.g. Amorosi et al., 2017). Millennial-scale, low-rank T-R cycles (parasequences) marked by abrupt landward or seaward shoreline shifts and associated with metre-scale sea-level fluctuations, have been linked to middle- to late-Holocene ultra-high-frequency climatic events (e.g., Roman Warm Period, Medieval Warm Period, Little Ice Age). Accordingly, the alternations of back-barrier, lagoonal, and coastal-pond deposits recognised in the uppermost part of the core is interpreted to have developed during the last 6 ka, reflecting ultra-high-frequency climate variability. The saline deposits, most likely formed during the lagoonal phase are nowadays diluted and dissolved in freshwater during seasonal runoff events and precipitated as surface saline crusts during the hot Sardinian summer at the Sal’e Porcus pond.

Chapter 3

Relative sea-level fluctuations of the last millennium recorded by intertidal algal rims (NW Sardinia, Mediterranean Sea)

Giovanni Fantini[1], Daniele Sechi[1], Vincenzo Pascucci[2], Stefano Andreucci[1]

[1]Department of Chemical and Geological Sciences, University of Cagliari, 09042 Monserrato. Italy

[2]Department of Architecture, Design and Urban Planning, University of Sassari, 07041 Alghero. Italy

This manuscript was submitted to *The Holocene* on 15 September 2025, received a major revision decision on 12 December 2026, and was accepted for publication on 2 March 2026 (pre-proof stage).

Relative sea-level fluctuations of the last millennium recorded by intertidal algal rims (NW Sardinia, Mediterranean Sea)

Giovanni Fantini[1], Daniele Sechi[1], Vincenzo Pascucci[2], Stefano Andreucci[1]

[1]*Department of Chemical and Geological Sciences, University of Cagliari, 09042 Monserrato. Italy*

[2]*Department of Architecture, Design and Urban Planning, University of Sassari, 07041 Alghero. Italy*

Abstract

The Mediterranean calcareous red alga *Lithophyllum byssoides* forms thick bioconstructions in the intertidal zone, developing in a very narrow vertical range (ca. 20 cm), making it an exceptionally precise indicator of past sea-level positions. This high sensitivity to even minimal sea-level fluctuations enables the detection of high-frequency, low-amplitude changes that occurred over the last 1000 years. The Late Holocene relative sea-level curve presented here, is based on *L. byssoides* rims extensively encrusting the swell-exposed rocky shores of the Mesozoic limestone cliffs of northwestern Sardinia (NW Mediterranean). The rim accretion structures reveal the *in situ* superposition of multiple generations of *L. byssoides* thalli, which bind sand-sized clasts. Combined AMS radiocarbon dating identifies four main growth phases, each bounded by distinct erosional surfaces. These phases correlate with stages of relative sea-level rise and coincide with the warmest periods of the last millennium. In contrast, erosional surfaces frequently draped by a reddish muddy matrix indicate sea-level drops associated with the coldest phases of the Little Ice Age. Our findings indicate decimetric relative sea-level fluctuations on sub-centennial timescales, which significantly exceed the average magnitude of sea-level change documented over the last millennium, implying major shifts in coastal dynamics and ecosystems. These results support a strong link between sub-centennial climate variability and sea-level fluctuations and underscore the value of *L. byssoides* rims as high-resolution archives of past sea-level oscillations.

Keywords: Sea level changes, Sub-centennial fluctuations, Climate change, Late Holocene, Coralline algae, Algal rims, Mediterranean

1. Introduction

Future projections of ongoing global warming and sea-level rise forecast significant socio-economic impacts, particularly for populations living in low-lying coastal areas (e.g., Calvin et al., 2023). To better guide adaptation strategies, current trends must be placed within the context of high-resolution past variability. Reconstructing proxy-based sub-centennial sea-level fluctuations over the last millennium and into the current Industrial Era (IE) is therefore a key task for sea-level rise modeling efforts (e.g., Mariotti et al., 2002; Roberts et al., 2010; Onac et al., 2022; Blanfuné et al., 2023). The Holocene, the current interglacial (Marine Isotopic Stage 1, MIS 1), reached its climatic optimum, known as the Mid-Holocene Climatic Optimum (MHCO), around 6.8 ka ago, when global temperatures were similar to, or slightly higher than present levels (Mann, 2002; Davis et al., 2003; Perry & Hsu, 2000). During the early Holocene, global mean sea level rose at approximately 1 cm/year until the MHCO, after which slowed to a few millimeters per year. This reduced rate persisted until the onset of the Industrial Era (IE; post-1850 AD), when it began to accelerate again (Lambeck et al., 2004, 2011; Grant et al., 2012; Vacchi et al., 2021; Calvin et al., 2023). However, focusing on average rates can obscure rapid (sub-centennial) relative sea-level fluctuations linked to warm–cold and/or wet-dry climate oscillations. Over the last millennium, three main climatic periods with increasing human impacts over time have been recognized: i) the warm Medieval Climate Anomaly (MCA; AD 900–1250); ii) the Little Ice Age (LIA; AD 1250–1850), which encompasses four solar minima of sunspot activity—Wolf (AD 1275–1300), Spörer (AD 1460–1550), Maunder (AD 1645–1715), and Dalton (AD 1790–1830)—characterized by temperature drops of up to 1°C in the Northern Hemisphere (Perry & Hsu, 2000; Stranne et al., 2014; Wanner et al., 2022); and iii) the current warm phase known as the Industrial Era (IE) since AD 1860. Moreover, several oceanographic model- and proxy-based global sea-level reconstructions (Church et al., 2001; Gregory et al., 2006; Rahmstorf, 2007; Jevrejeva et al., 2008; Kemp et al., 2011; Kopp et al., 2016) suggest that short-term climatic warming and cooling phases can drive the thermal expansion and contraction of seawater, thereby contributing to sea-level changes, along with a smaller contribution from the loss of glacial and ice cap mass. These processes can produce rapid (sub-centennial-scale) and low-amplitude (decimeter-scale) fluctuations in sea level. However, such low-amplitude sea-level changes are often hidden in the Holocene sedimentary record and require extremely precise sea-level markers to detect them (Vacchi et al., 2016).

Among the most sensitive and reliable sea-level indicators are intertidal bioconstructions formed by the calcareous red alga *Lithophyllum byssoides* (Lamarck) Foslie (Corallinales, Rhodophyta). This species forms an algal rim-shaped structure that grows within a very narrow intertidal vertical range (~20 cm above mean sea level) and is widely recognized as a very precise sea-level marker in the Mediterranean region (Adey, 1986; Laborel et al., 1989, 1994; Morhange et al., 1992; Vacchi et al., 2016, 2021; Faivre et al., 2013, 2019a, 2023, 2024; Sechi et al., 2020).

This study documents sub-centennial relative sea-level fluctuations during the last millennium, as recorded by *L. byssoides* rims along the rocky coasts of northwestern Sardinia. Specific questions addressed include: (i) the amplitude of eustatic changes, (ii) the definition of algal rim accumulation rates, and (iii) comparison with available sea-level curves.

2. Geological setting and study area

Sardinia is the second-largest island in the western Mediterranean Sea, extending from 38° to 41° N and from 8° to 10° E (Fig. 1a). The Oligocene–early Miocene eastward migration of the Apennines subduction zone induced a major rifting phase in the Corsica–Sardinia lithospheric block, which drifted eastward from the Provençal–Catalan margin of Europe to its present position in the central western Mediterranean Sea, in conjunction with the opening of the Liguro-Provençal Basin (Fig. 1a; Doglioni et al., 1998). Following this tectonic phase, Sardinia experienced widespread volcanic activity, which ceased in the late Pleistocene (~140 ka). Today, the island is considered a semi-stable continental block, characterized by low seismicity and slow regional uplift (Carmignani et al., 2016). Nevertheless, geomorphic and structural evidence indicates late Pleistocene to Holocene tectonic activity, primarily linked to the reactivation of normal faults (e.g., Cocco et al., 2019; Casini et al., 2020; Sechi et al., 2023). The northwestern coast of Sardinia exposes a bedrock mainly composed of Mesozoic limestones and dolostones, locally underlain by Permo-Triassic quartz-rich sandstones and conglomerates ("red beds") and Oligo-Miocene volcanic bodies. These lithologies form the prominent coastal cliffs of the area.

Unconformably overlying them is a discontinuous Quaternary succession, ranging from shallow-marine to aeolian deposits spanning from MIS 5e (135–116 ka) to MIS 3 (57–29 ka) (Andreucci et al., 2010, 2012; Pascucci et al., 2014; Sechi et al., 2020; Zucca et al., 2014a, b). Notably, Sechi et al. (2020) documented a meter-thick *Lithophyllum byssoides* algal ridge bioconstruction within the Late Pleistocene marine sequence along the Northwest coast of the island. This feature, developed directly on pre-Quaternary bedrock and dated to the Last Interglacial (MIS 5e), represents the first known evidence of thick bioconstruction formation during this interval on the Sardinian coast. In addition, extensive coastal quarries carved into Pleistocene aeolianites during the Spanish colonial period (15^{th}–17^{th} centuries) provide further stratigraphic exposures and sea-level constraints during the last millennium (Pascucci et al., 2019; Fig. 1b). The Mediterranean Sea is microtidal, with an average tidal range of approximately 35 cm (Longhitano, 2011; Pascucci et al., 2019). A wave buoy located just north of Capo Caccia (ISPRA; Mareografo.it), records dominant winds from the northwest (called Mistral in Sardinia).

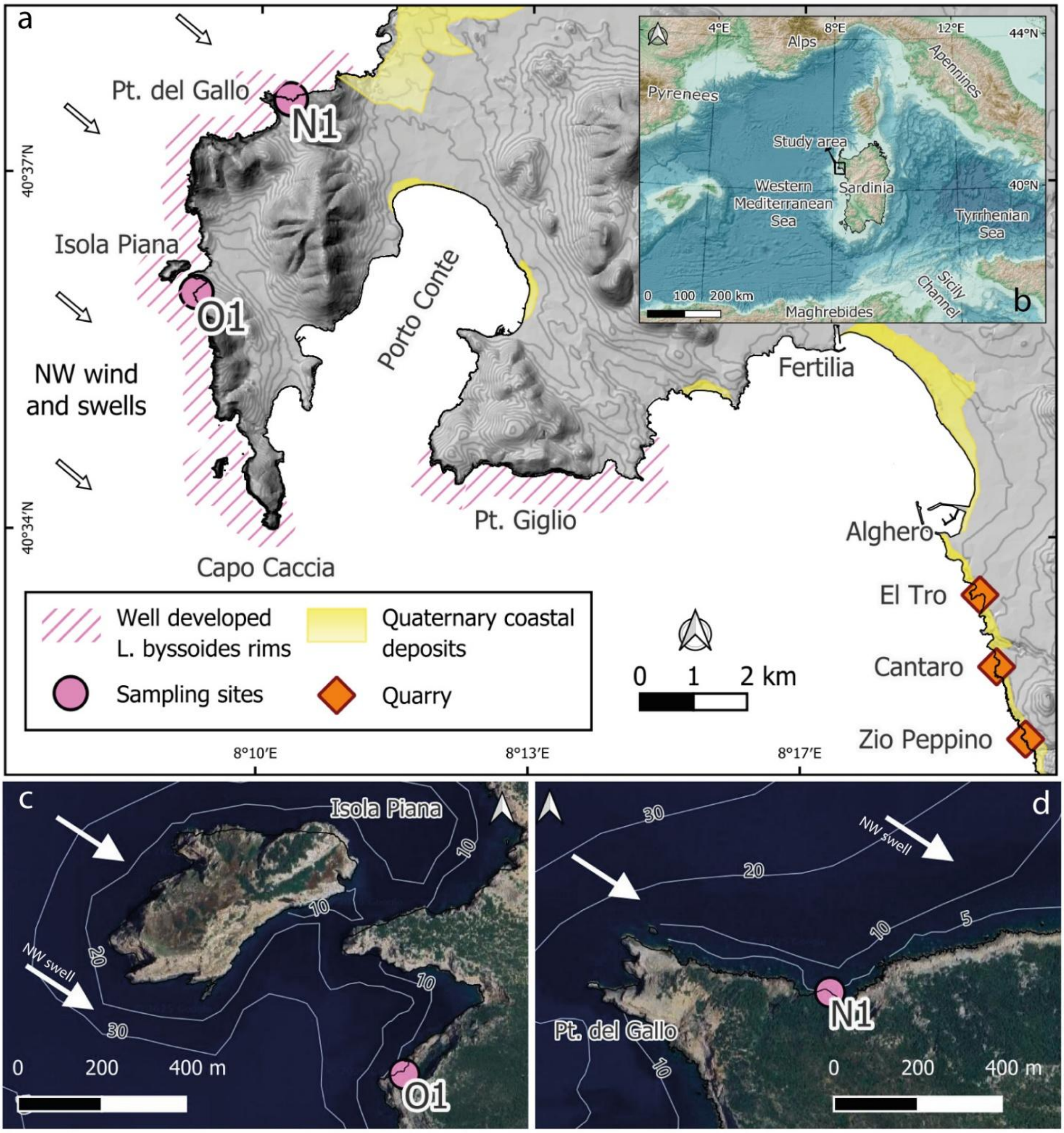

Figure 1. *Capo Caccia study area**: a)** Geomorphological map of the area of Capo Caccia, maps report the areal distribution of L. Byssoide rims along the coast, mainly encrusting sea-facing plunging cliff. The Quaternary deposits mantle the low-elevation area. N1 and O1 highlight the sampling area. Diamond symbol reports the location of the main Spanish quarries.* ***b)*** *Location of Sardinia in the western Mediterranean area.* ***c) - d)*** *Detail of the coast morphology for the two sampling areas (N1, O1) and bathymetric contour lines. Arrows highlight the direction of the main blowing wind, Mistral (NW), and sea swell.*

These winds can exceed 80 km/h during storm events, generating wave heights of up to ~7 m and mean wave periods ranging from 2 to 13 s. The main study area, the peninsula of Capo Caccia (northwestern Sardinia, Italy) is characterized by high, steep Mesozoic limestone cliffs plunging into the sea (Fig. 1b). These cliffs delimit small embayments and pocket beaches, which are primarily fed by bioclastic sediments derived from nearby *Posidonia oceanica* meadows (Andreucci et al., 2023).

3. Materials and methods

3.1 Sampling, structure analysis and dating

The areal distribution of *Lithophyllum byssoides* rims was surveyed by kayak between March and October 2023 along approximately 24 km of coastline around the Capo Caccia peninsula (Fig. 1, 2a). Sampling focused on two main sites, O1 and N1, which are located in areas less exposed to hydrodynamic effects caused by the interaction between wave action and cliff morphology (Fig. 1b, 2b-c). To minimize vertical uncertainty, sampling was avoided in areas near cave entrances, narrow inlets, or major rock fractures, where local hydrodynamics could affect the vertical growth of the algal rims (Fig. 2d). Rims were sampled with a hammer and chisel during calm sea conditions. Their elevation measured using a metric rope and GPS, is expressed relative to Biological Mean Sea Level (BMSL) defined as the lowest elevation of the presence of living *L. byssoides* thalli at each site. The nearest Porto Torres tide-gauge record, the global EGM96 geoid and the Italian national vertical datum (Genova 1942) were used only as auxiliary references for measurement consistency checks and were not adopted as reference datums for RSL index-point calculations.

A total of two samples were collected (O1: 24.2 × 20.1 cm; N1: 23.8 × 16.1 cm; dimensions measured along the longest vertical and horizontal axes, respectively). The algal rim samples were longitudinally sliced following their natural growth direction, and a total of 35 standard petrographic thin sections were prepared (14 from N1; 21 from O1; Figs. 3, 4, 5, SM1). Investigation of algal builders, analysis of rim inner structures and growth pattern along with identification of sediment clasts, matrix and cement compositions were carried out on petrographic thin sections using transmitted optical microscope and Scanning Electron Microscope (SEM; JEOL JCM-700; Fig. 3). A morphometric analysis was conducted to quantitatively measure conceptacle chamber dimensions and to qualitatively observe algal thalli cell morphology, following standard taxonomic criteria (Woelkerling, 1983; Chamberlain, 1997). The description of algal macro- and microstructures followed the taxonomy and methodology of Woelkerling et al. (1993) and Di Geronimo et al., (2002). Distinct growth phases were identified based on: (i) erosional or growth discontinuities, (ii) sandy drapes or silica-rich muddy matrix intercalations, and (iii) differences in cementation degree.

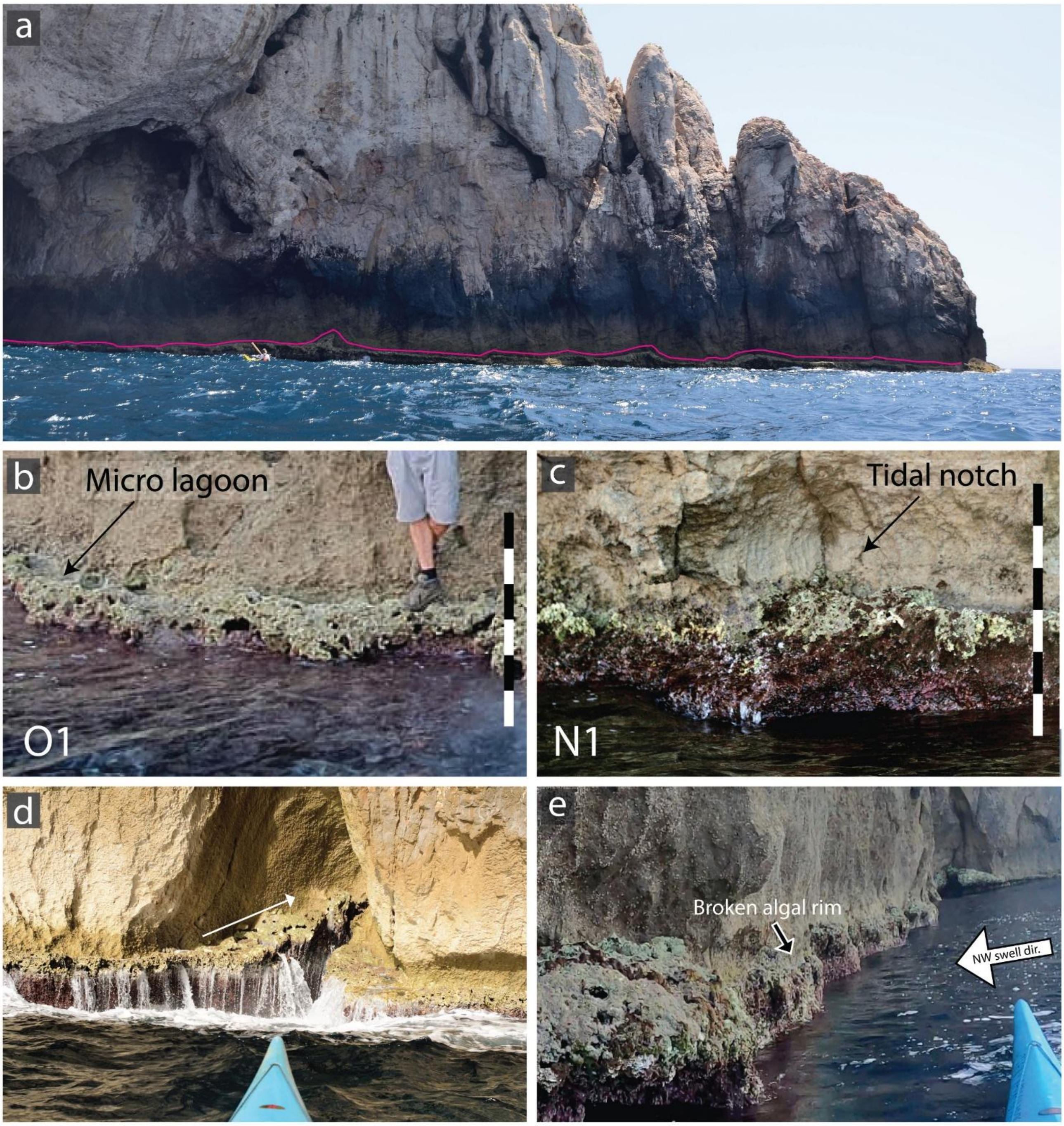

Figure 2. *Bio-geomorphological survey* ***a)*** *Panoramic view of Liyhophyllum byssoides rim around Capo Caccia cliffs (person on kayak for scale is ca. 1 m);* ***b)*** *Detail view acquired during sampling of O1 rim growing on a small wave-cut platform. Note a well-developed micro lagoon on the left. Scale bar = 10 cm;* ***c)*** *Detail view acquired during sampling of N1 rim growing within a well-developed tidal notch. Scale bar = 10 cm;* ***d)*** *Detail view of a Liyhophyllum byssoides rim growing around large rock fracture. Note the hydrodynamic effects on rim highlighted by the sea water cascade.* ***e)*** *Panoramic view of a cliff fully exposed to major storms. Note the rim ruptures and multiple interruptions.*

Six algal thalli from each sample were selected for radiocarbon dating (^{14}C), sampled along the growth direction (Tab. 1; Fig. 4-5). Dating has been performed by the Beta Analytic laboratory (Miami, USA), before the measurement, the micritic matrix and bioclastic-rich sand were removed from the chosen thalli. Radiocarbon ages were calibrated using the MARINE20 curve (Heaton et al., 2020) and corrected for the western Mediterranean marine reservoir effect ($\Delta R = -184 \pm 22$; Faivre et al., 2019b).

Sample ID	Lab. No.	Selected Material	cal ^{14}C age AD (median)	Cal age range (68.2%, cal AD)
N1	Beta-669808	*L. byssoides* thallus	1701	1613–1790
N3	Beta-669809	*L. byssoides* thallus	1713	1626–1800
N9	Beta- 669812	*L. byssoides* thallus	1740	1660–1820
N10	Beta-705827	*L. byssoides* thallus	1909	1896–1939
N13	Beta-705829	*L. byssoides* thallus	1920	1890–post 1950
N14	Beta-669813	*L. byssoides* thallus	1924	1898–post 1950
O1	Beta-705029	*L. byssoides* thallus	1050	972–1128
O2	Beta-705034	*L. byssoides* thallus	1062	984–1141
O7	Beta-705030	*L. byssoides* thallus	1630	1549–1714
O11	Beta-705031	*L. byssoides* thallus	1631	1548–1715
O16	Beta-705032	*L. byssoides* thallus	1720	1637–1804
O20	Beta-705033	*L. byssoides* thallus	1881	1818–post 1950

Table 1. *Calibrated radiocarbon ages of Lithophyllum byssoides samples; Calibrated calendar ages obtained from AMS radiocarbon dating of Lithophyllum byssoides samples analysed in this study. Radiocarbon measurements were performed by Beta Analytic. Calibration was carried out using the MARINE20 calibration curve, applying the appropriate regional marine reservoir correction (ΔR) and the High Probability Density (HPD) method. Ages are reported as median calibrated values together with the corresponding 68.2% probability intervals. Additional details on calibration procedures are provided in the Supplementary Material.*

Following the conceptual approach proposed by Basso et al. (2022), vertical accumulation was quantified where continuous rim growth could be demonstrated within a single growth phase. This approach was applied only to the lower zone of N1 rim (see chapter 4.5 and figure 5) where no evidence of erosional truncation or growth hiatuses was observed. In this case, rims accumulation rate was therefore calculated using the vertical distance between dated samples belonging to the same growth phase and progressing toward the top living surface of the bioconstruction.

3.2 Analysis of relative sea-level index points

The Relative Sea-level (RSL) was calculated for all the ^{14}C dated thalli (12 in total) and estimated using the following equation (Shennan and Horton, 2002; subsequently modify by Vacchi et al., 2016):

$$RSL_i = A_i - RWL_i$$

Where A_i is the altitude; RWL_i is the Reference Water Level of sample i; Both expressed relative to Biological mean sea level BMSL of O1 and N1 study sites (Tab. 2). As an example, a dated thallus at site N1 has a measured elevation of 7 cm below the N1 BMSL, thus, A is −7 cm. For *Lithophyllum byssoides,* the indicative range (IR) yields a Reference Water Level (RWL) of 25 cm relative to BMSL (midpoint of the IR; Fig. 4). The relative sea-level position is therefore calculated as: RSL = A − RWL = −7 − 25 = −32 cm. Following Vacchi et al. (2016), the Reference Water Level (RWL) represents the midpoint of the indicative range (IR) of a given sea-level indicator and reflects its indicative meaning rather than a measured elevation. For *Lithophyllum byssoides* bioconstructions, the indicative range is biologically defined and spans the intertidal zone between the Highest Astronomical Tide (HAT) and the Biological Mean Sea Level (BMSL; Fig. 4, 5). Along Capo Caccia limestone cliffs, observations of rim position indicate a typical vertical dispersion of approximately 20 cm, consistent with previous studies, and this range is conservatively expressed as an uncertainty of ±10 cm around the RWL. Within this uncertainty, BMSL is assumed to approximate present-day mean sea level, thereby minimizing site-specific hydrodynamic conditions (Laborel et al., 1994; Vacchi et al., 2016; Rovere et al., 2016, 2022; Faivre et al., 2019a, 2021, 2023, 2024). Unlike biological or sedimentary index points, terrestrial limiting points (TLP) do not require the definition of a full indicative range and provide only a unidirectional constraint on past sea level. Therefore, the coastal quarry surfaces south of Capo Caccia (Fig. 1; Pascucci et al., 2019) are treated here as terrestrial limiting points providing an upper limit to relative sea level, indicating that sea level could not have exceeded the quarry working surface elevation during their period of use (Vacchi et al.,

Sample ID	A (cm)	RWL (cm)	RSL index point (cm)	GIA (cm) adjustment	Adjusted RSL index point (cm)	Age cal AD (median)
N1	−7	25	−32 ± 10	13 ± 5	−19 ± 10	1701
N3	8	25	−17± 10	12 ± 5	−5 ± 10	1713
N9	11	25	−14 ± 10	11± 4	−3 ± 10	1740
N10	12	25	−13 ± 10	5 ± 2	−8 ± 10	1909
N13	14	25	−11 ± 10	4 ± 2	−7 ± 10	1920
N14	16	25	−9 ± 10	4 ± 1	−5 ± 10	1924
O1	4	25	−21 ± 10	39 ± 15	18 ± 15	1050
O2	5	25	−20 ± 10	38 ± 15	18 ± 15	1062
O7	7	25	−18 ± 10	16 ± 6	−2 ± 10	1630
O11	8	25	−17 ± 10	16 ± 6	−1 ± 10	1631
O16	10	25	−15 ± 10	12 ± 5	−3 ± 10	1720
O20	11	25	−14 ± 10	6 ± 2	−8 ± 10	1881
Quarries	/	/	−35 to −45	16 ± 4	−19 to − 29 (TLP)	1500 - 1600

Table 2. *Relative sea-level (RSL) index points; relative sea-level (RSL) index points derived from Lithophyllum byssoides bioconstructions at Capo Caccia and Terrestrial Limiting Points (TLPs) from coastal quarries south of Alghero. Sample elevation (A) is measured relative to Biological Mean Sea Level (BMSL). The Reference Water Level (RWL) represents the midpoint of the indicative range of the sea-level indicator type, following Vacchi et al. (2016). RSL index points are calculated as RSL = A − RWL. GIA adjustment values correspond to the glacial isostatic adjustment correction applied to each index point. Ages are reported as median calibrated ages (see Table 1 for radiocarbon details).*

2016; Pascucci et al., 2019). A vertical uncertainty of ±10 cm was adopted, reflecting the limited functional tolerance of quarry working surfaces and the good preservation state of the structures, in line with previous archaeological sea-level studies in the Mediterranean (e.g., Antonioli et al., 2007). In addition, all the markers were adjusted for glacial isostatic adjustment (GIA) using a constant isostatic vertical rate of -0.4 ± 0.15 mm/yr, as suggested by Spada and Melini (2022), based on an ensemble of ANU S4 (E1) and ICE-6G C (VM5a) Earth models (Lambeck & Purcell 2005; Peltier et al., 2015, respectively).

4. Results

4.1 Bio-geomorphological survey

Results of the kayak survey show an almost continuous intertidal algal rim around the main promontories of the study area (Figs. 1b, 2a). Prominent and well-developed bioconstructions occur along the northern and western coasts of Capo Caccia (Fig. 1), where they are subject to consistent wave action due to direct exposure to the prevailing Mistral winds (NW) and associated swells. This observation aligns with previous studies, which indicate that the growth, thickness, and morphology of *L. byssoides* rims are strongly influenced by local wave energy exposure (Laborel et al., 1994; Faivre et al., 2013; Sechi et al., 2020). The thickest and largest rims develop at cave entrances and within large rock fractures, where non-breaking wave run-up causes an increase in water level against the cliff face (Fig. 2d). Nevertheless, bioconstructions growing on cliffs fully exposed to severe swells tend to be thinner and show signs of breakage and discontinuity (Fig. 2e). Rim thickness and lateral continuity increase in particular geomorphic settings, such as rocky inlets with partial protection and a deeper seabed in front. These conditions promote stable environments that favor both vertical and seaward lateral accretion of the rim structure.

4.2 Rim inner structure and builder

Thin section and SEM analyses reveal that both the O1 and N1 rims consist of several generations of anastomosing algal thalli with characteristic upward-facing, fan-shaped branches that define the predominant upward and seaward growth directions of the rim (Fig. 3a; Woelkerling et al., 1983, 1993; Mannino, 2003; dryades.units.it). These bioconstructions are formed by a continuous superposition of new thalli above the dead ones following a slow-rising sea level (keep-up like model), as generally proposed by Pérès and Picard (1964) and (Adey, 1986; Laborel et al., 1994). Based on these structural features, the bioconstructions are classified as framestones, as the in-situ fossil Crustose Coralline Algae (CCA) thalli form a rigid framework, with bio-siliciclastic sandy sediments trapped between different algal generations (Fig. 3b). Conceptacle chambers morphometry (typically ~100–160 µm in average width; Pezzolesi et al., 2017) led to the taxonomic identification of *L. byssoides* as the dominant framework builder of the studied bioconstructions (Figs. 3c–d). The trapped sediment is composed of fine-grained bioclastic sand, including fragments of coralline algae, bivalves, gastropods, bryozoans, foraminifera, and serpulids, along with minor quartz and feldspar grains. In some areas of the O1 and N1 inner rims, a silica-rich, reddish terrigenous muddy matrix is abundant (Fig. 3e).

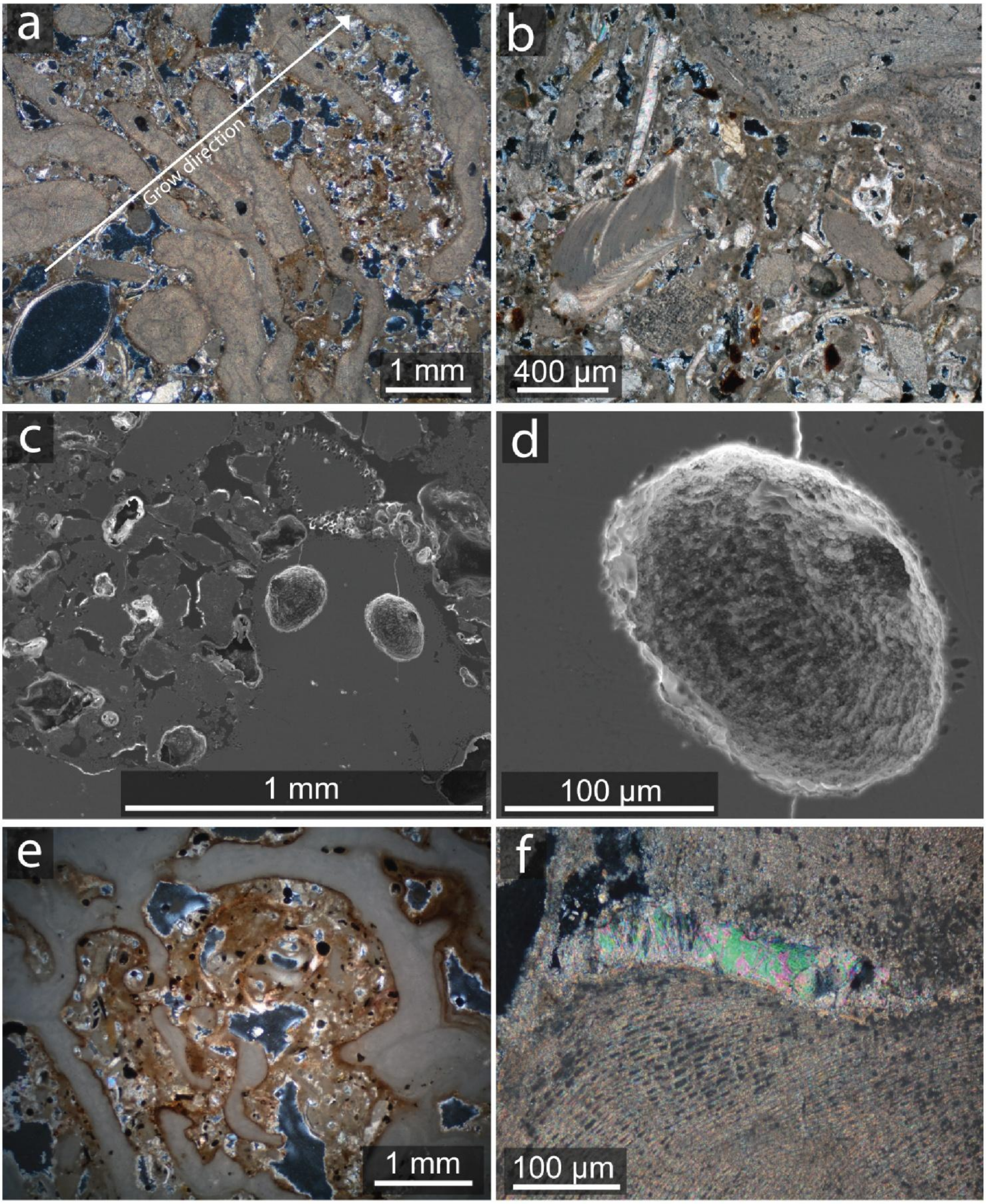

Figure 3. *Thin section:* ***a)*** *general overview with growth directions arrow;* ***b)*** *bio-siliciclastic trapped sediment details;* ***c)*** *Secondary electron image of L. byssoides thallus and sediment;* ***d)*** *Detail of L. byssoides conceptacle;* ***e)*** *reddish fine matrix in the trapped sediment, right below the N1 erosional surface;* ***f)*** *Intra-thallus cement details with L. byssoides thalli cells*

Typical intertidal calcite spar cement, with inter- and intraparticle equant crystals, welds the sediment to the algal thalli, partially filling the voids and consolidating the rim framework (Fig. 3f). The high complexity of the rim inner structure is primarily due to algal growth and infilling within cavities produced by bioeroders (e.g *Lithophaga lithophaga)*. The identification of conceptacle chamber orientation (Woelkerling, W.J. 1983; Chamberlain, Y.M. 1997), along with the morphometric analysis of algal thalli, has proven essential for interpreting bioconstruction with stratigraphic coherence. Site-specific inner structures reveal multiple growth phases and shifts in sediment infill and cementation, as outlined below.

4.3 Study site O1

Site O1 is located on the west coast of the Capo Caccia peninsula near Isola Piana, in a rocky embayment that is open to the west but partly sheltered from NW-incoming Mistral winds. The seafloor here reaches approximately 7 m depth (Figs. 1a, 1d). tab, a few decimeters wide, forming a micro-lagoon on its upper surface near the cliff (Figs. 2b, 4). It is attached to the vertical substrate through the land-facing side and the sea-facing side featured by a protuberance in its upper part. The most abundant top side coverage consisted of living individuals of *Lithophyllum byssoides* surrounded by few other Crustose Coralline Algae (CCA; i. e. *Lithophyllum incrustans*, *Lithophyllum papillonis)*. The sea side of the rim, immediately below the lower limit of living *Lithophyllum byssoides* individuals (BMSL), is characterized by a typically subtidal assemblage dominated by *Ceramium* and *Corallina elongata* and exhibits particularly intense bioerosion compared to the upper surface, with cavities mostly occupied by *Lithophaga lithophaga* and *Patella caerulea*.

A general fruticulose aspect with a multi-layered structure and the branch shaped thalli has been observed from the polished rim slice (Fig. 4). O1 shows three barely developed erosional surfaces, delineating four different inner zones (Fig. 4). Furthermore, a millimeters-thick white crust of closely patched laminar sets of other CCA developed inside the micro lagoon on the top of the land side of the rim. The lower unconformity is highlighted by a higher degree of cementation and a diffuse silty-clay reddish matrix in the rim below the surface (Figs. 3e; 4). In the inner zone above the latter surface, cementation is markedly lower and the reddish muddy matrix is absent. The middle and upper unconformities are dominated by rough surfaces with several cavities filled by biogenic and siliciclastic sediments (Fig. 4). The inner zone between these unconformities is rich in sediments and muddy reddish matrix, whereas the outermost part shows a well-developed sediment drape lying on the upper surface.

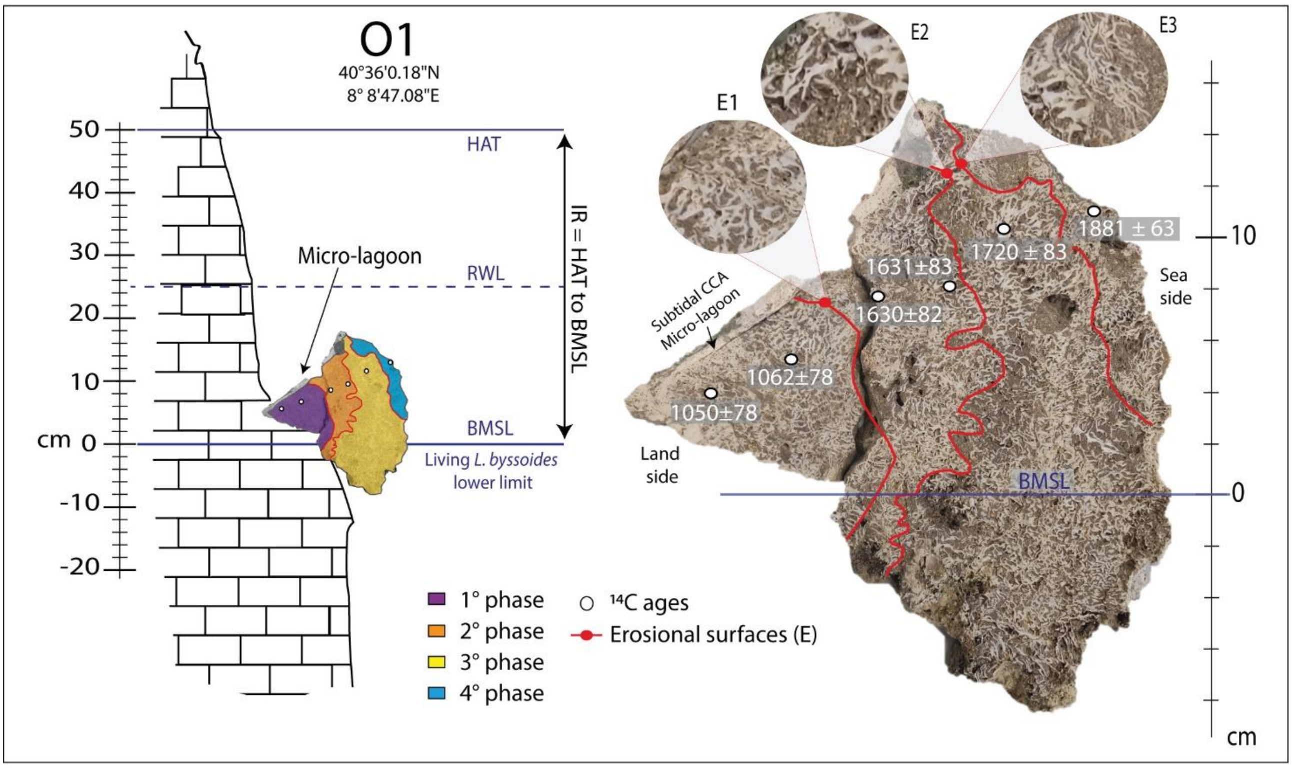

Figure 4. *O1 site. Geometry, vertical position and internal structure of the Lithophyllum byssoides algal rim, measured relative to the local Biological Mean Sea Level (BMSL), independently defined at the site from the lower living limit of L. byssoides. The rim position at the time of sampling is shown with respect to the Highest Astronomical Tide (HAT), with the Reference Water Level (RWL) indicated as the midpoint of the biologically defined indicative range (IR = HAT to BMSL). Rim thickness, internal pattern of growth and erosional surface dividing the rim growth phases (1st to 4th phase). Note erosional surfaces zooms (E1–E3), together with the position of radiocarbon-dated samples.*

4.4 Study site N1

Site N1, located on the north coast near Punta del Gallo, lies within a northwest-facing rocky cove that is slightly exposed to Mistral winds and characterized by a shallow seafloor, approximately 3 m deep (Figs. 1a, 1c). It exhibits a 24 cm thick rim that stands at the base of a well-developed tidal notch (Figs. 2c, 5). The land-facing side is attached to the vertical substrate, while the sea-facing side features an upper protuberance and a highly porous surface, with millimeter- to centimeter-sized cavities, many of which are occupied by *Lithophaga lithophaga*. Externally, the rim is predominantly covered by subtidal Crustose Coralline Algae (e.g., *Lithophyllum incrustans*, Fig. 2b), and is generally sparsely colonized by living *Lithophyllum byssoides*, which occurs only with a few individuals above the top surface.

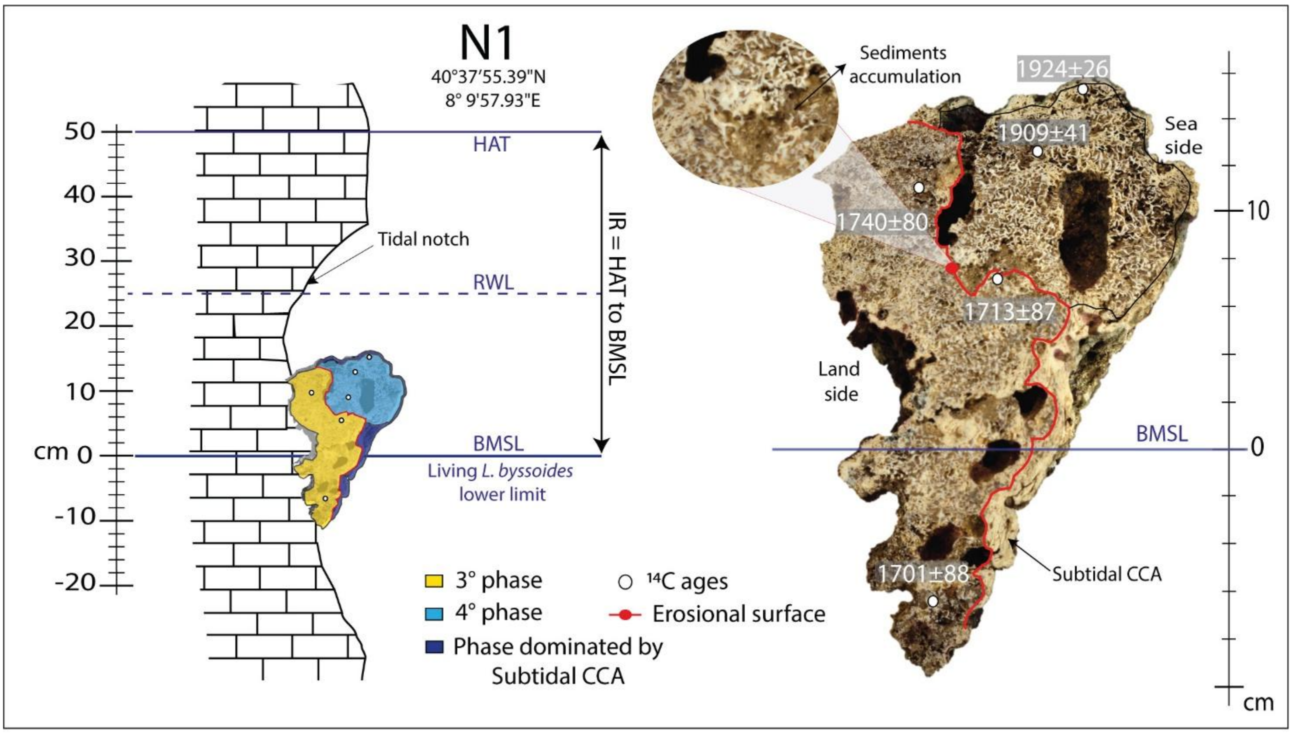

Figure 5. *N1 site. Geometry, vertical position and internal structure of the Lithophyllum byssoides algal rim relative to the local Biological Mean Sea Level (BMSL). The rim position at the time of sampling is shown with respect to the Highest Astronomical Tide (HAT), with the Reference Water Level (RWL) defined as the midpoint of the biologically constrained indicative range. Note rim thickness, internal pattern of growth and erosional surface dividing the rim growth phases (3rd–4th phase), including portions dominated by subtidal coralline crustose algae (CCA). Erosional surfaces zoom (E), together with the position of radiocarbon-dated samples.*

From the polished rim slice, the multi-layered structure and the branch shaped thalli give a general fruticulose aspect to the inner pattern (Fig. 5). The presence of a well-developed erosional surface draped by a centimeter thick sandy accumulation, allows us to subdivide the N1 slice into two inner zones (Fig. 5). Below the erosional surface, sample N1 shows well-formed cement crystals, with algal skeleton cells mostly filled, reducing the porosity, along with a higher concentration of silty-clay reddish matrix (Fig. 3e). Above the erosional surface, there are more interspaces between the thalli, and the trapped sediments are generally less cemented with conceptacle chambers often empty. Moreover, a distinctive white crust, ranging from a few millimeters to one centimeter in thickness, has developed on the seaward side of the rim (Fig. 5). This encrustation is composed of tightly packed thalli of subtidal Crustose Coralline Algae (CCA), forming a continuous and visually striking white layer. Its presence indicates a shift from intertidal to subtidal assemblages, as the crust is composed of CCA species typically found in deeper, permanently submerged environments.

4.5 Chronology of rim growth

To reconstruct the chronological framework of rim accretion, a total of twelve *Lithophyllum byssoides* thalli fragments were collected from the O1 and N1 sites for radiocarbon dating (Figs. 4, 5; Tab. 1). For O1, six samples were extracted from distinct inner zone of the rim (Fig. 4). Two fragments, from the innermost land-side portion, yielding calibrated radiocarbon ages of 1050 ± 78 and 1060 ± 78 cal AD, respectively. Two additional samples, taken from the mid-zone between the lower and middle erosional surfaces, returned ages of 1630 ± 82 and 1631 ± 82 cal AD. Two thalli collected from just below and above the uppermost erosional surface were dated to 1720 ± 83 and 1881 ± 63 cal AD, respectively.

Six thalli fragments were dated to constrain the accretional history of the N1 rim (Fig. 5). Three samples collected from the lower zone, beneath the erosional surface, yielded ages of 1701 ± 88, 1713 ± 87, and 1740 ± 80 cal AD. The lower zone of N1 rim segment shows continuous accretion between 1701 and 1740 AD with no evidence of erosional truncation or growth hiatuses. Over this interval, the bioconstruction records a vertical accretion of 16 cm, corresponding to an average accumulation rate of ~4 mm yr^{-1} (16 cm over ~40 years). This value represents a phase-specific bioconstruction accumulation rate, applicable only to this sample and to this time span due to the consistent succession of the dated thalli. This value is reported as an indicative mean accumulation rate, given that radiocarbon age uncertainties. In contrast, three samples retrieved from above the erosional surface yielded younger ages of 1909 ± 41, 1920 ± 30, and 1924 ± 26 cal AD.

The stratigraphic distribution shows O1 ages gathering into four coherent growth phases (Fig. 4), with each age group falling within the 68.2% probability intervals and showing no overlap between age clusters (Tab. 1). The N1 rim also displays two distinct age clusters (Fig. 5), with no overlap in their calibrated age probability distributions (68.2% probability intervals; Tab. 1). This chronological separation mirrors the observed sedimentological discontinuity, suggesting a pause or shift in rim growth, followed by renewed accretion in subsequent, progressively younger phases. The vertical and lateral arrangement of the dated material—from older layers at the base to younger ones toward the seaward margin—confirms a preferential accretional growth trajectory oriented seaward and upward, from the substrate toward the outer surface of the rims.

5. Discussion

On a sub-centennial time scale, Mediterranean Sea-level response to air temperature warming and cooling is mainly driven by the rate of seawater thermal expansion (Church et al., 2001; Gregory et al., 2006; Rahmstorf, 2007; Jevrejeva et al., 2008; Kemp et al., 2011; Kopp et al., 2016). To isolate the climate-driven component of relative sea-level change, RSL index points derived from the studied *Lithophyllum byssoides* rims were adjusted for glacial isostatic adjustment (GIA) and evaluated in relation to the terrestrial limiting point (TLP) provided by the Alghero coastal quarries (Pascucci et al., 2019). Spada and Melini (2022) report an ongoing GIA of - 0.4 ± 0.15 mm/yr (total vertical displacement), for the NW Sardinia coast. For the period considered, applying a constant GIA rate is appropriate, given the timescale of Earth's viscoelastic response (Peltier, 1996, 2004). Applying GIA corrections shifted the amplitude of the observed fluctuations, along with the associated uncertainties, particularly affecting the oldest samples (Table 2).The distribution of the GIA-adjusted RSL index points reveals that the main phases of rim growth correspond to periods during which relative sea level was rising and coincide with the warmest stages of the last millennium (Fig. 6). In contrast, the erosional surfaces observed within the rim structure point to phases of sea-level fall, which correlate well with the coldest stages of the Little Ice Age (Fig. 4, 5, 6). Within this framework, it is important to consider the growth behaviour of *Lithophyllum byssoides* as a sea-level proxy. Rim accretion preferentially occurs under slowly rising sea-level conditions (Laborel et al., 1994; Faivre et al., 2013; Sechi et al 2020). Excessively rapid sea-level rise inhibits vertical rim development (Faivre et al., 2013), whereas sea-level fall and the resulting permanent subaerial exposure primarily stop rim growth and intertidal cementation processes, potentially leading to breakage of the bioconstruction (erosional surfaces) and subsequently to the deposition in cavities on the erosive surface of sandy-muddy drapes. Consequently, algal rims provide an informative record of relative sea-level behavior, from which average RSL rise rates can be inferred, albeit with significant uncertainty. This approach allows the identification of successive phases of relative sea-level rise associated with rim development. By doing so, sub-centennial-scale relative sea-level change can be distinguished, which would otherwise be obscured by a single long-term trend in the RSL index point.

5.1 Climate control on algal rim evolution over the last 1000 years

The intertidal algal rims studied at Capo Caccia (Sardinia, Mediterranean Sea) clearly display four distinct phases of *Lithophyllum byssoides* growth, each separated by marked erosional surfaces. These growth phases correspond to periods of relative sea-level rise, whereas the erosional surfaces—draped in bio-siliciclastic sand-sized sediments and reddish muddy matrix—point to prolonged (multi-decadal) episodes of subaerial exposure and relative sea-level fall. Together with AMS radiocarbon ages, these features indicate four sub-centennial phases of sea-level rise and three sea-level falls over the last millennium, which can be tied to European summer temperature anomaly reconstructions (Luterbacher et al., 2016; Wanner et al., 2022; Fig. 6). The first growth phase, observed in the O1 rim and dated to around 1050 AD, developed during the Medieval Climate Anomaly (900–1225 AD), a prolonged warm period preceding the cold Little Ice Age (Wanner et al., 2022).

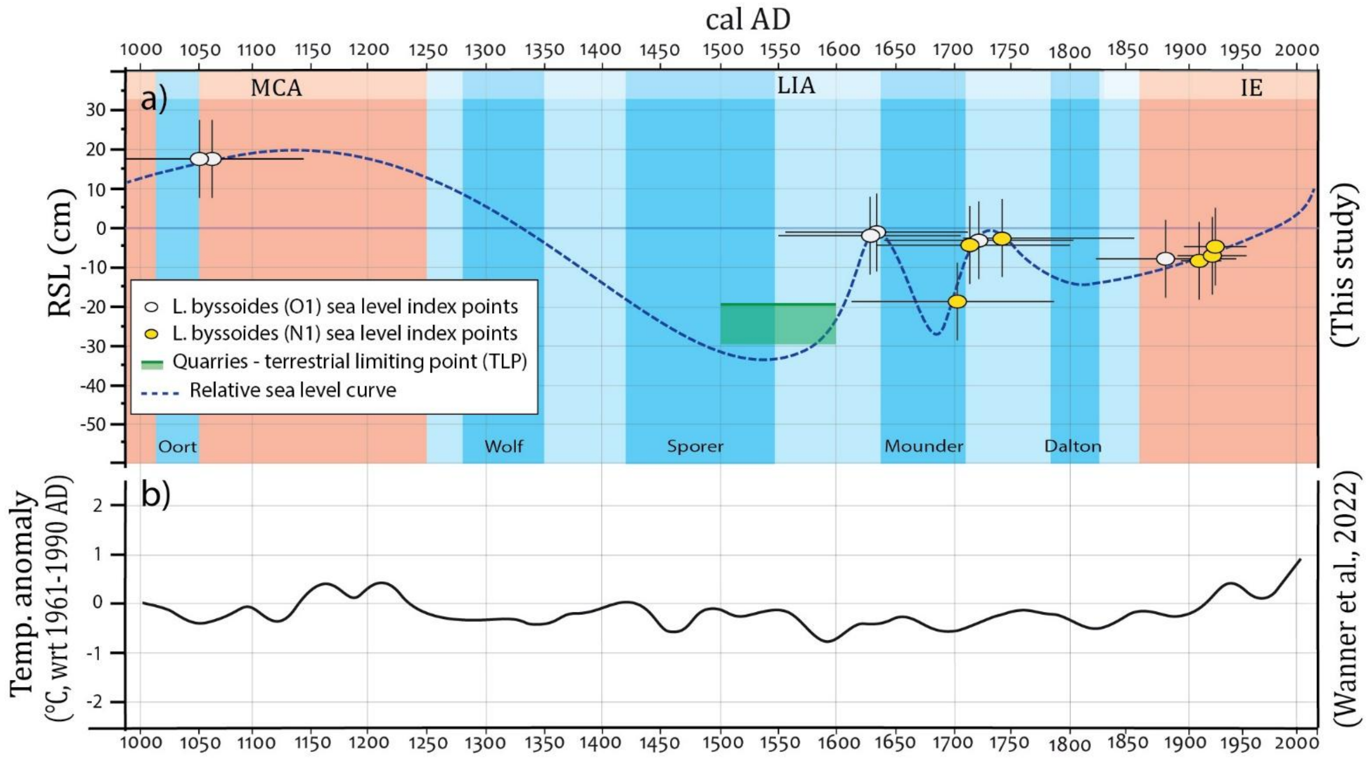

Figure 6. *Relative sea-level (RSL) reconstruction from Capo Caccia Lithophyllum byssoides algal rims, compared with European summer temperature anomalies over the last millennium. (a) GIA adjusted RSL curve constrained by algal-rim sea-level index points from the O1 (white circles) and N1 (yellow circles) sites, and by an archaeological terrestrial limiting point (TLP) derived from submerged coastal quarries (green box). The RSL curve is tracked considering rim internal structure, including erosional surfaces and the distribution of red muddy matrix, which indicate phases of growth interruption and relative sea-level lowering. Shaded vertical bands indicate major climatic phases (MCA, LIA, IE) and solar minima (Oort, Wolf, Spörer, Maunder, Dalton). (b) Reconstructions of European summer temperature anomalies relative to the 1961–1990 AD mean, illustrating centennial-scale climate variability over the last 1000 years (after Luterbacher et al., 2016; Wanner et al., 2022).*

The available data are insufficient to precisely constrain the entire duration of this growth phase. Furthermore, regional to global reconstructions highlight pronounced spatial and temporal variability in global mean sea level (GMSL) and regional relative sea level during the MCA. These records indicate a relative lowstand around ~1000–1050 AD (Oort Minimum), followed by a relative sea-level rise between ~1100 and 1200 AD (e.g. Kopp et al., 2016; Vacchi et al., 2021; Faivre et al., 2023), occurring during a period when mean air temperatures were comparable to or slightly lower than present-day values (Fig. 6; Wanner et al., 2022).Subsequently, a period of both arrested *L. byssoides* growth and partial erosion of the rim occurred, likely driven by a relative sea-level fall associated with the onset of the Little Ice Age (LIA). Notably, phases of reduced solar activity during the Common Era have been associated with global mean sea level lowering (e.g. Kopp et al., 2016; Faivre et al., 2023), providing a broader climatic context for the observed local RSL behaviour. The definitive transition to the European LIA took place with the Wolf and Spörer Grand Solar Minima (GSM; periods of markedly reduced solar activity), each accompanied by clusters of volcanic eruptions (Wanner et al., 2022). The longer LIA cooling phases were typically triggered by such eruptions, which coincided with Grand Solar Minima (Bradley et al., 2016) and were further intensified by internal feedback involving the atmosphere, oceans, and sea ice. Around 1575 AD, temperatures dropped to –2 °C compared to present (Luterbacher et al., 2016), marking one of the coldest intervals of the LIA. The second growth phase took place in the first half of the 17th century during a relatively warm period (–0.3 °C below present) between the Spörer and Maunder solar minima (Warren et al., 2022). Subsequently, a relative sea-level drop frames the Maunder Minimum (air temperature –0.5 °C below present), and during the first half of the 18th century, rim accretion resumed with a pronounced relative sea-level rise. This period was characterized by a positive European summer temperature anomaly, with temperatures reaching 1990s levels (Fig. 6). This warming was driven by increased solar irradiance (marking the end of the Maunder Minimum) and a reduced incidence of volcanic eruptions (Perry & Hsu, 2000; Warren et al., 2022), creating favorable conditions for the algal rim development. The sampled rims also show evidence of a third severe erosion (Fig. 3, 5), linked to a relative sea-level drop driven by the last cold pulse (Dalton Minimum) of the LIA, occurring between 1800 and 1860 AD (Wanner et al., 2022). In the early 19th century, European summer temperatures fell to –3 °C compared to present (Luterbacher et al., 2016; Fig. 7), influenced by the Dalton GSM and at least four major volcanic eruptions between 1808 and 1835 AD. The 1815 Tambora eruption, in particular, played a decisive role in this cooling climate (Sigl et al., 2015). This cooling is also reflected in the third and most pronounced advance of the Great Aletsch and Gorner Alpine glaciers in 1860 AD (Holzhauser et al., 2005). With the onset of the Industrial Era after 1860 AD, gradual warming began, likely driven by reduced volcanic activity and increased solar irradiance (Wanner et al., 2022; Calvin et al., 2023; Fig. 6). This natural warming set the stage for modern sea-level rise and triggered the fourth phase of rim accretion at Capo Caccia. In the 20th century, greenhouse gas concentrations increased exponentially, and after 1988 AD, the transition to rapid warming accelerated global sea-level rise consistently (Luterbacher et al., 2016; Vacchi et al., 2021; Wanner et al., 2022; Calvin et al., 2023). This phenomenon has led to the ongoing submergence of the N1 rim and the formation of a white crust made by other subtidal Crustose Coralline Algae, clearly visible on its seaward side (Fig. 2c, 5). In contrast, the O1 rim appears to have maintained active vertical accretion, likely supported by site-specific exposure conditions that promote frequent water renewal within the intertidal zone (Fig. 2b, 4). Currently, the surface of the N1 rim shows a marked reduction in *Lithophyllum byssoides* and a profuse presence of other CCA species, typically thriving in subtidal environments (e.g., *L. incrustans*). This shift in CCA assemblage is consistent with a partial drowning of the N1 rim and thus reflects a biological response to the recent acceleration in relative sea-level rise.

5.2 Relative Sea-Level Changes and Comparison with Proxy-Based Reconstructions

Sub-centennial sea-level fluctuations during the Late Holocene remain poorly constrained in the proxy record. To evaluate the broader significance of the four rim growth phases and associated sea-level rises and drops observed at Capo Caccia, these findings are cautiously compared with established Mediterranean and global sea-level reconstructions (Gregory et al., 2006; Gehrels et al., 2006; Goodwin and Harvey, 2008; Leorri et al., 2008; Garcia-Artola et al., 2009; Kemp et al., 2011; Kopp et al., 2016; Faivre et al., 2019a, 2023; Vacchi et al., 2021), as well as with millennial-scale climate variability and solar insolation trends (Fig. 6; Perry and Hsu, 2000; Luterbacher et al., 2016; Wanner et al., 2022). At Capo Caccia, the Medieval Climate Anomaly is recorded in the early phase of O1 rim development (ca. 1050–1060 AD). The associated relative sea level index points are positioned above present sea level and, following the Oort Minimum, likely reflects environmental conditions favorable to algal rim accretion (Fig. 4, 6). This interpretation is consistent with previously reported RSL rise rates, ranging between 0.5 and 0.7 mm/yr from algal rim records in the Adriatic Sea (Faivre et al., 2019a, 2023, 2024), as well as comparable rising rates inferred from North Atlantic salt-marsh sedimentary records between ~850 and 1250 AD (Kemp et al., 2011). A more prolonged RSL fall followed between 1200 and 1600 AD, which corresponds to the development of a well-defined lower erosional surface in the O1 rim. During the ca. 1500–1600 AD interval, terrestrial limiting points from the Alghero coastal quarries constrain the local RSL to have remained at least 35 cm below present mean sea level (Pascucci et al., 2019). After correction for glacial isostatic adjustment and considering 10 cm of uncertainty, this constraint corresponds to a terrestrial limiting elevation ranging between 19 and 29 cm, below present mean sea level (Fig. 6). This terrestrial limiting point indicates that relative sea level could not have exceeded the elevation of the quarry working surfaces during their period of use (Pascucci et al., 2019). In addition, the occurrence of a reddish matrix within the studied O1 algal rim further suggests extended periods of subaerial exposure, implying that sea level may have dropped by over half a meter during the onset of the Little Ice Age as firstly assumed by Pascucci et al, (2018) working on the sedimentary sequence of Mistral beach-ridge system (W Sardinia). This lowstand aligns with near-stable or slightly negative trends recorded in various Mediterranean and global sea-level reconstructions (Kemp et al., 2011; Faivre et al., 2019a, 2023; Vacchi et al., 2021), reinforcing the climatic significance of this period. A renewed phase of relative sea-level rise is identified between ~1600 and 1630 AD. The onset of this phase is constrained by a terrestrial limiting point (TLP) from the Alghero coastal quarries, while its upper termination is defined by two RSL index points from the O1 rim. This phase records a RSL rise occurred within a relatively warm interval between the Spörer and Maunder solar minima (Fig. 6). This phase was short-lived, as growth ceased again in the latter half of the 17th century—coincident with the Maunder Minimum—when a relative sea-level drop of at least 20 ±10 cm, producing erosion and subsequent increments of sediment accumulation, likely interrupted and slowed the O1 rim accretion (Fig. 4, 6). Growth resumed during the following warm period (ca. 1700 and 1740 AD), between the Maunder and Dalton minima, indicating a phase of sustained relative sea level rise. While these growth-related relative sea-level rises exceed the frequency and amplitude typically reported for the Late Holocene, they may reflect brief warm oscillations that are not clearly resolved in the proxy record. In contrast, during this time interval, several studies document a lack of rim formation (Faivre et al., 2019a) or stable to slightly negative sea-level behavior (Kemp et al., 2011). Following 1740 AD, both rims display evidence of a marked depositional hiatus and erosional truncation, suggesting a relative sea-level fall of at least 20 ±10 cm. Coastal stratigraphy from western Sardinia further supports this interpretation, with records of beach progradation linked to falling sea level and increased sediment supply (Pascucci et al., 2018). This lowstand coincides with the final cold stage of the Little Ice Age, associated with the Dalton Grand Solar Minimum (ca. 1800–1860 AD), and aligns with global reconstructions indicating a significant sea-level drop during this time (Gregory et al., 2006; Kopp et al., 2016). These parallels suggest that the sea-level trend observed at Capo Caccia likely fits within a broader regional, northern hemispheric, pattern. At Capo Caccia the algal rims record a renewed relative sea-level rise between 1881 and 1909 AD, increasing progressively by 1924 AD. These interpretations are in agreement with regional observations from the northeastern Adriatic (Faivre et al., 2019a) and with records from the North Atlantic, where rates of up to 2.1 mm/yr were documented between 1865 and 1892 (Kemp et al., 2011). A broader global acceleration in sea-level rise around 1863 AD is also supported by proxy database analyses (Walker et al., 2022). This early phase of modern sea-level rise likely reflects a combination of reduced volcanic activity and modest increases in solar irradiance following the end of the Little Ice Age. However, these natural forcings remained relatively stable or declined in the following decades, indicating that they cannot account for the pronounced acceleration observed after the mid-20th century (IPCC, 2021; Haigh et al., 2019). According to a growing number of global and relative sea-level reconstructions (Gregory et al., 2006; Kemp et al., 2011; Kopp et al., 2016; Faivre et al., 2019a, 2023; Vacchi et al., 2021), the increase in greenhouse gas concentrations during the industrial era—particularly from the second half of the 20th century—has led to a marked warming of global temperatures. This, in turn, triggered a progressive and widespread acceleration of global sea-level rise through thermal expansion of seawater and increased melting of land-based ice. In this context, Mediterranean Sea-level curves show rates ranging between 1 and 3 mm/yr (Faivre et al., 2019; Vacchi et al., 2021), which are consistent with the presence of well-developed subtidal external white crusts in the N1 rim (Fig. 5, 6). These findings confirm that the growth phases of the algal rims capture the transition from "natural" Holocene sea-level variability to modern, anthropogenically driven sub-centennial sea-level trends.

6. Conclusions

The intertidal red algal rims of Capo Caccia have recorded sub-centennial relative sea-level fluctuations over the last millennium. At this timescale, sea level shows great variability, with high-frequency and low-amplitude oscillations. These are controlled by the differential response of Mediterranean Sea level to cooling and warming episodes, as demonstrated by the related sea-level fluctuation recorded in the algal rims. The amplitude of the detected fluctuations is on the order of tens of centimeters, leading to important changes in coastal dynamics. Overall, rim growth phases document periods of relative sea-level rise during the warmest intervals of the last millennium, whereas erosional surfaces reflect phases of sea-level fall associated with the coldest stages of the Little Ice Age. The first growth phase developed during the first half of the 11th century and is associated with the warm Medieval Climate Anomaly (MCA). It, is followed by a period of sea level fall of at least half of a meter that persisted until 1600 AD. At Capo Caccia, relative sea level then increased during the second and third growth phases (~1600-1630 AD and ~1701-1740 AD, respectively), separated by a sea-level drop of at least 20 cm coinciding with the Maunder Minimum. The third growth phase is followed by another drop of about 10 cm, corresponding to the final cold phase of the LIA (first half of the 19th century, Dalton GSM). The subsequent modern sea-level rise (post-1860 AD) began driven by natural factors. During the second half of the 20th century, it underwent a speed-up triggered by greenhouse gas-induced global warming. This phenomenon has caused the ongoing submergence of the N1 rim and the formation of a white crust of subtidal Crustose Coralline Algae, clearly visible on its seaward side. N1 rim surface now shows a marked decline in *Lithophyllum byssoides* and an abundance of other CCA species (e.g., *L. incrustans*) typical of subtidal conditions. These features indicate a partial drowning of the rim, most likely driven by the recent acceleration in sea-level rise. Between 1701–1740 AD, under favorable environmental conditions, the mean accumulation rate of the N1 rim is estimated approximately 3–4 mm yr^{-1} (16 cm over ~40 years), acknowledging the associated chronological uncertainty. This suggests that Lithophyllum byssoides can build up and keep pace with relative sea-level rise of comparable magnitude. However, excessively rapid sea-level rise—such as the current trend—promotes the colonization of subtidal species, increasing competition and inhibiting the development of *L. byssoides* rims. Over the last millennium, these findings reveal four main sub-centennial phases of relative sea-level rise that promoted rim growth, separated by three sea-level drops, resulting in prolonged subaerial exposure of the rims. Our observations confirm the close link between climate and sea-level change and highlight the ability of coralligenous intertidal bioconstructions as sensitive paleoenvironmental archives, particularly useful for reconstructing sea-level dynamics during the transition from the pre-industrial to the industrial era.

Acknowledgements

The authors thank Dario Fancello and the CeSAR (Centro Servizi d'Ateneo per la Ricerca) of the University of Cagliari, Italy, for the SEM analyses; Alberto Ruiu of the Marine protected area Capo Caccia, Isola Piana, Alghero, Italy; Salvatore Noli for the production of thin sections; Alessia Fronteddu and Gianluca Loi for their contributions to sample preparation within the framework of their bachelor theses in Geology.

Author contributions

Conceptualization, GF, DS and SA; methodology, GF and SA; investigation, GF and SA; formal analysis, GF and SA; writing—original draft preparation, GF; data curation, GF; fieldwork, GF, VP and SA; writing—review and editing, GF, DS, SA and VP; supervision, SA; project administration, SA; funding acquisition, SA. All authors have read and agreed to the published version of the manuscript.

Statements and Declarations

The authors declare that they have no known competing financial interests or personal relationships that could have appeared to influence the work reported in this paper.

Funding statement

We acknowledge financial support under the National Recovery and Resilience Plan (NRRP), Mission 4, Component 2, Investment 1.1, Call for tender No. 1409 published on 14.9.2022 by the Italian Ministry of University and Research (MUR), funded by the European Union – NextGenerationEU– Project Title WaCoMed – CUP P2022EPCJS- Grant Assignment Decree No. 1388 adopted on 01/09/2023 by the Italian Ministry of University and Research (MUR; Resp. prof. Andreucci Stefano). This article was produced by GF while attending the PhD programme in Earth and Environmental Sciences and Technologies at the University of Cagliari, Cycle XXXVIII, with the support of a scholarship financed by NRRP, funded by the European Union - NextGenerationEU - Mission 4 "Education and Research", Component 2 “From Research to Business” – Investment 1.3 “Creation of “enlarged partnerships between universities, research centres, businesses and funding of basic research projects”.

Data availability

The dataset includes geochronological results (radiocarbon), field data (GPS coordinates, elevations), and processed files used to generate the figures and tables of the manuscript. Data are available at Mendeley Data: Fantini, Giovanni; Andreucci, Stefano; Sechi, Daniele; Pascucci, Vincenzo (2026), “Fantini et al., 2026”, Mendeley Data, V2, doi: 10.17632/8jwfmfp2cy.2

Discussion

Climate change, sea-level fluctuations, and tectonic control on coastal evolution across different timescales

This thesis provides an integrated, multi-archive reconstruction of coastal sedimentary sequences in Sardinia, spanning the Middle–Late Pleistocene to historical timescales, and addressing the gap between long-term sea-level trends and high-frequency coastal responses. Comparing different sedimentary archives within a single regional framework offers new insights into the controls governing coastal system variability under changing climatic conditions. In particular, the thesis explores how coastal sequences respond to interactions among tectonics, climate, and eustatic fluctuations over timescales ranging from hundreds to thousands of years, focusing on successions from different areas of Sardinia (southern, western, and northwestern sectors).

The coastal successions of southern Sardinia record repeated phases of marine transgression, shoreline progradation, and regression within unconformity-bounded units correlated with MIS 7, MIS 5e, and MIS 5c highstands. The study sites display contrasting stacking patterns, with composite terrace sequences preserving either MIS 7–MIS 5e or MIS 5e–MIS 5c marine units. These results indicate that composite marine terraces are a recurrent feature along the southern Sardinian coast. Moreover, the distribution of marine terrace sequences cannot be explained solely by glacio-eustatic sea-level fluctuations; instead, it reflects dominant tectonic control. The data support segmentation of southern Sardinia into crustal blocks affected by spatially and temporally variable uplift since at least the Middle–Late Pleistocene, where even modest uplift generates complex depositional architectures characterized by unconformities and re-occupation processes rather than simple staircase sequences. These sequences therefore record the interplay among variable uplift rates, climate change, and eustatic fluctuations at Milankovitch-frequency cyclicities (e.g., ~100 and ~20 ka). In this context, composite marine terraces, when integrated with stratigraphic and chronological data, enable reconstruction of sea-level–tectonic interactions and reveal subtle tectonic signals in regions traditionally considered stable.

The combined effects of regional-scale tectonic activity and Holocene sea-level rise governed the infill of the Sal'e Porcus coastal pond on the Sinis Peninsula (western Sardinia). The Sal'e Porcus pond formed during rapid Holocene sea-level rise as a lagoon behind a coastal barrier (beach-ridge system), and was subsequently isolated by coastal progradation, punctuated by millennial- to centennial-scale sea-level fluctuations that led to the establishment of the present-day barrier and the Is Benas lagoon. In particular, the alternation of back-barrier, lagoonal, and coastal-pond deposits developed over the last ~6 ka in response to this variability, likely linked to high-frequency climatic variability (e.g., Roman Warm Period, Medieval Climate Anomaly, Little Ice Age). Finally, saline surface crusts at Sal'e Porcus are currently reworked by seasonal processes, dissolving during runoff events and precipitating during the dry summer period.

Intertidal algal rims at Capo Caccia record sub-centennial relative sea-level fluctuations over the last millennium, characterized by high-frequency, low-amplitude (decimetre-scale) oscillations linked to climatic variability. Growth phases correspond to relative sea-level rise during warm periods (e.g., Medieval Climate Anomaly), whereas erosional surfaces reflect sea-level fall during colder intervals, including the Little Ice Age. Four main phases of sea-level rise promoted rim growth, separated by three drops that caused subaerial exposure. Relative sea level fell by ≥ 0.5 m until ~1600 AD, followed by renewed rises (~1600–1630 and ~1701–1740 AD), interrupted by minor drops (e.g., Maunder Minimum) and a final decrease during the Dalton Minimum. Since ~1860 AD, sea level has risen, with acceleration in the late 20th century driven by anthropogenic warming, leading to partial drowning of the rims and replacement of Lithophyllum byssoides by subtidal coralline algae. Although rim growth can keep pace with moderate sea-level rise (~4 mm yr^{-1}), rapid modern rise inhibits its development. These results highlight the sensitivity of coralligenous intertidal bioconstructions to climate-driven sea-level variability and their value as high-resolution paleoenvironmental archives.

The integration of these depositional archives demonstrates how climatic processes influence coastal evolution across different timescales and how larger-scale processes, such as tectonics, can complicate the stratigraphic record. These findings highlight the need for detailed, multi-archive and multi-timescale approaches to better understand natural coastal variability. Future projections of ongoing global warming and sea-level rise indicate significant socio-economic impacts, particularly for populations in low-lying coastal areas (e.g., Calvin et al., 2023). Placing current trends in the context of high-resolution past variability is therefore essential for informing effective adaptation strategies.

References

Adey, W.H. (1986). Coralline algae as indicators of sea level. In O. Van de Plassche (Ed.), Sea Level Research: A Manual for the Collection and Evaluation of Data (pp. 229–280). Springer Netherlands, Dordrecht. https://doi.org/10.1007/978940094215014

Amorosi, A., Bruno, L., Campo, B., Morelli, A., Rossi, V., Scarponi, D., Hong, W., Bohacs, K.M. and Drexler, T.M., 2017. Global sea-level control on local parasequence architecture from the Holocene record of the Po Plain, Italy. *Marine and Petroleum Geology*, *87*, pp.99-111.

Andreucci, S., Pascucci, V., Murray, A. S., & Clemmensen, L. B. (2009). Late Pleistocene coastal evolution of San Giovanni di Sinis, west Sardinia (Western Mediterranean). Sedimentary Geology, 216(3-4), 104-116. https://doi.org/10.1016/j.sedgeo.2009.03.001

Andreucci, S., Clemmensen, L. B., Murray, A. S., & Pascucci, V. (2010). Middle to late Pleistocene coastal deposits of Alghero, northwest Sardinia (Italy): Chronology and evolution. Quaternary International, 222(1-2), 3-16. https://doi.org/10.1016/j.quaint.2009.07.025

Andreucci, S., Clemmensen, L.B., & Pascucci, V. (2010). Transgressive dune formation along a cliffed coast at 75 ka in Sardinia, Western Mediterranean: a record of sea level fall and increased windiness. Terra Nova, 22(6), 424–433.

Andreucci, S., Panzeri, L., Martini, I. P., Maspero, F., Martini, M., & Pascucci, V. (2014). Evolution and architecture of a West Mediterranean Upper Pleistocene to Holocene coastal apron-fan system. Sedimentology, 61(2), 333-361. https://doi.org/10.1111/sed.12058

Andreucci, S., Sechi, D., Buylaert, J. P., Sanna, L., & Pascucci, V. (2017). Post-IR IRSL290 dating of K-rich feldspar sand grains in a wind-dominated system on Sardinia. Marine and Petroleum Geology, 87, 91-98. https://doi.org/10.1016/j.marpetgeo.2017.03.025

Andreucci, S., Santonastaso, A., De Luca, M., Cappucci, S., Cucco, A., Quattrocchi, G., & Pascucci, V. (2023). A shallow-water dunefield in a microtidal, wind-dominated strait (Stintino, NW Sardinia, Italy). Straits and Seaways: Controls, Processes and Implications in Modern and Ancient Systems, V.M. Rossi, S.G. Longhitano, C. Olariu, F.L. Chiocci. https://doi.org/10.1144/SP523-2021-188

Antonioli, F., Ferranti, L., Lambeck, K., Kershaw, S., Verrubbi, V., & Dai Pra, G. (2006). Late Pleistocene to Holocene record of changing uplift rates in southern Calabria and northeastern Sicily (southern Italy, Central Mediterranean Sea). Tectonophysics, 422(1-4), 23-40. https://doi.org/10.1016/j.tecto.2006.05.003

Antonioli, F., Anzidei, M., Amorosi, A., Presti, V. L., Mastronuzzi, G., Deiana, G., ... & Vecchio, A. (2017). Sea-level rise and potential drowning of the Italian coastal plains: Flooding risk scenarios for 2100. Quaternary Science Reviews, 158, 29-43. https://doi.org/10.1016/j.quascirev.2016.12.021

Auclair, M., Lamothe, M. and Huot, S., 2003. Measurement of anomalous fading for feldspar IRSL using SAR. Radiation measurements, 37(4-5), pp.487-492. https://doi.org/10.1016/S1350-4487(03)00018-0

Basso, D., Nalin, R. and Nelson, C.S., 2009. Shallow-water Sporolithon rhodoliths from North Island (New Zealand). Palaios, 24(2), pp.92-103. https://doi.org/10.2110/palo.2008.p08-048r

Basso, D., Bracchi, V.A., Bazzicalupo, P., Martini, M., Maspero, F., & Bavestrello, G. (2022). Living coralligenous as geo historical structure built by coralline algae. Frontiers in Earth Science, 10, 961632. https://doi.org/10.3389/feart.2022.961632

Blanfuné, A., Boudouresque, C.F., Verlaque, M., Minne, A., Noisette, F., & Thibaut, T. (2023). Impact of sea level rise on the Mediterranean Lithophyllum byssoides rims. Scientific Reports, 13, 10577. https://doi.org/10.1038/s41598 023 37737 2

Bøtter-Jensen, L. and Mejdahl, V., 1988. Assessment of beta dose-rate using a GM multicounter system. International Journal of Radiation Applications and Instrumentation. Part D. Nuclear Tracks and Radiation Measurements, 14(1-2), pp.187-191. https://doi.org/10.1016/1359-0189(88)90062-3

Bu, M., Murray, A.S., Kook, M., Buylaert, J.P. and Thomsen, K.J., 2021. The application of full spectrum analysis to NaI (Tl) gamma spectrometry for the determination of burial dose rates. Geochronometria, 48(1), pp.161-170. DOI 10.2478/geochr-2020-0009

Buylaert, J.P., Murray, A.S., Thomsen, K.J. and Jain, M., 2009. Testing the potential of an elevated temperature IRSL signal from K-feldspar. Radiation measurements, 44(5-6), pp.560-565. https://doi.org/10.1016/j.radmeas.2009.02.007

Calvin, K., Dasgupta, D., Krinner, G., Mukherji, A., Thorne, P.W., Trisos, C., … & Hauser, M. (2023). Climate Change 2023: Synthesis Report. Summary for policymakers. Contribution of Working Groups I, II & III to the Sixth Assessment Report of the Intergovernmental Panel on Climate Change. IPCC, Geneva. https://doi.org/10.1017/9781009157896

Camoin, G.F. and Webster, J.M., 2015. Coral reef response to Quaternary sea-level and environmental changes: State of the science. Sedimentology, 62(2), pp.401-428. https://doi.org/10.1111/sed.12184

Cantalamessa, G. and Di Celma, C., 2004. Sequence response to syndepositional regional uplift: insights from high-resolution sequence stratigraphy of late Early Pleistocene strata, Periadriatic Basin, central Italy. Sedimentary Geology, 164(3-4), pp.283-309. https://doi.org/10.1016/j.sedgeo.2003.11.003

Carboni, S., Nicolò, C., Pala, A. & Pili, S.L. (2002). Hydrogeological study of the deep aquifers of Sinis (Central-Western Sardinia). Rendiconti Seminario Facoltà Scienze Università Cagliari, 72(1).

Carmignani, L., Oggiano, G., Funedda, A., Conti, P. and Pasci, S., 2016. The geological map of Sardinia (Italy) at 1: 250,000 scale. Journal of Maps, 12(5), pp.826-835. https://doi.org/10.1080/17445647.2015.1084544

Casini, L., Andreucci, S., Sechi, D., Huang, C.Y., Shen, C.C. and Pascucci, V., 2020. Luminescence dating of Late Pleistocene faults as evidence of uplift and active tectonics in Sardinia, W Mediterranean. Terra Nova, 32(4), pp.261-271. https://doi.org/10.1111/ter.12458

Casula, G., Cherchi, A., Montadert, L., Murru, M. and Sarria, E., 2001. The Cenozoic graben system of Sardinia (Italy): geodynamic evolution from new seismic and field data. Marine and Petroleum Geology, 18(7), pp.863-888. https://doi.org/10.1016/S0264-8172(01)00023-X

Cherchi, A., Marini, A., Murru, M., & Ulzega, A. (1978a). Movimenti neotettonici nella Sardegna meridionale.

Cherchi, A., Marini, A., Murru, M., & Robba, E. (1978b). Stratigrafia e paleoecologia del Miocene superiore della penisola del Sinis (Sardegna occidentale). Rivista Italiana di Paleontologia e Stratigrafia, 84, 973–1036.

Cherchi, A. & Martini, E. (1981). Calcareous nannoplankton and planktonic foraminifera of the Messinian and basal Pliocene from Capo S. Marco (W. Sardinia). Géologie Méditerranéenne, 8, 109-120.

Cherchi, A., & Montadert, L. (1982). Oligo-Miocene rift of Sardinia and the early history of the western Mediterranean basin. Nature, 298(5876), 736-739.

Cherchi, A., Mancin, N., Montadert, L., Murru, M., Putzu, M.T., Schiavinotto, F. and Verrubbi, V., 2008. The stratigraphic response to the Oligo-Miocene extension in the western Mediterranean from observations on the Sardinia graben system (Italy). Bulletin de la Société géologique de France, 179(3), pp.267-287. https://doi.org/10.2113/gssgfbull.179.3.267

Cocco, F., Funedda, A., Patacca, E., & Scandone, P. (2013). Plio-Pleistocene extensional tectonics in the Campidano graben (SW Sardinia, Italy): Preliminary note. Rendiconti Online della Società Geologica Italiana, 29, 31–34.

Cocco, F., Funedda, A., Patacca, E., Scandone, P., 2013. The Campidano graben: an inherited Palaeogene rift in southern Sardinia (Italy). Rend. Online Soc. Geol. Ital. 24, 81–83.

Cocco, F., Andreucci, S., Sechi, D., Cossu, G., & Funedda, A. (2019). Upper Pleistocene tectonics in western Sardinia (Italy): Insights from the Sinis peninsula structural high. Terra Nova, 31(5), 485-493.

Cocco, F., Casini, L. and Funedda, A., 2024. Gravity field and geothermal structure of the Corsica-Sardinia Block. Terra Nova, 36(6), pp.506-515. https://doi.org/10.1111/ter.12738

Cornée, J. J., Maillard, A., Conesa, G., Garcia, F., Saint Martin, J. P., Sage, F., & Münch, P. (2008). Onshore to offshore reconstruction of the Messinian erosion surface in Western Sardinia, Italy: Implications for the Messinian salinity crisis. Sedimentary Geology, 210(1-2), 48-60.

Cresswell, A.J., Carter, J., Sanderson, D.C.W., 2018. Dose rate conversion parameters: Assessment of nuclear data. Radiat. Meas. 120, 195–201. https://doi.org/10.1016/j.radmeas.2018.02.007

Creveling, J.R., Mitrovica, J.X., Clark, P.U., Waelbroeck, C. and Pico, T., 2017. Predicted bounds on peak global mean sea level during marine isotope stages 5a and 5c. Quaternary Science Reviews, 163, pp.193-208. https://doi.org/10.1016/j.quascirev.2017.03.003

Crosetto, S., de Montserrat, A. and Oncken, O., 2024. Uplifted Pleistocene marine terraces at active margins: Modeling reveals the effects of sea reoccupation and coseismic uplift on uplift rate calculation. Geochemistry, Geophysics, Geosystems, 25(4), p.e2023GC011036. https://doi.org/10.1029/2023GC011036

Cunningham, A.C., Murray, A.S., Armitage, S.J., Autzen, M., 2018. High-precision natural dose rate estimates through beta counting. Radiat. Meas. 120. https://doi.org/10.1016/j.radmeas.2018.04.008

Davis, B. A., Brewer, S., Stevenson, A. C., Guiot, J., & Contributors, D. (2003). The temperature of Europe during the Holocene reconstructed from pollen data. Quaternary Science Reviews, 22(15-17), 1701-1716. https://doi.org/10.1016/S0277-3791(03)00173-2

Delitala, A.M., Cesari, D., Chessa, P.A., & Ward, M.N. (2000). Precipitation over Sardinia (Italy) during the 1946–1993 rainy seasons and associated large scale climate variations. International Journal of Climatology, 20(5), 519–541. https://doi.org/10.1002/(SICI)1097 0088(20000330)20:5<519::AID JOC471>3.0.CO;2 N

Di Geronimo, I., Di Geronimo, R., Rosso, A., & Sanfilippo, R. (2002). Structural and taphonomic analysis of a columnar coralline algal build up from SE Sicily. Geobios, 35, 86–95. https://doi.org/10.1016/S0016 6995(02)80009 9

Doglioni, C., Dagostino, N. and Mariotti, G., 1998. Normal faulting vs regional subsidence and sedimentation rate. Marine and Petroleum Geology, 15(8), pp.737-750. https://doi.org/10.1016/S0264-8172(98)00052-X

Dorsey, R.J., Di Vincenzo, G., Meschis, M., Longhitano, S.G., Cavazza, W. and Chiarella, D., 2026. Revised history of Pleistocene vertical motions in NE Sicily and southern Calabria, Italy, from 40Ar/39Ar dating and fault zone morphology. Tectonics, 45(2), p.e2025TC009008. https://doi.org/10.1029/2025TC009008

Dutton, A. and Lambeck, K., 2012. Ice volume and sea level during the last interglacial. Science, 337(6091), pp.216-219. DOI: 10.1126/science.1205749

Faccenna, C., Becker, T.W., Lucente, F.P., Jolivet, L. and Rossetti, F., 2001. History of subduction and back arc extension in the Central Mediterranean. Geophysical Journal International, 145(3), pp.809-820. https://doi.org/10.1046/j.0956-540x.2001.01435.x

Faivre, S., Bakran Petricioli, T., Horvatinčić, N., & Sironić, A. (2013). Distinct phases of relative sea level changes in the central Adriatic during the last 1500 years—influence of climatic variations? Palaeogeography, Palaeoclimatology, Palaeoecology, 369, 163–174. https://doi.org/10.1016/j.palaeo.2012.10.014

Faivre, S., Bakran-Petricioli, T., Barešić, J., Horvatić, D., & Macario, K. (2019). Relative sea-level change and climate change in the Northeastern Adriatic during the last 1.5 ka (Istria, Croatia). Quaternary Science Reviews, 222, 105909.

Faivre, S., Bakran-Petricioli, T., Barešić, J., Morhange, C., & Borković, D. (2019). Marine radiocarbon reservoir age of the coralline intertidal alga Lithophyllum byssoides in the Mediterranean. Quaternary Geochronology, 51, 15-23.

Faivre, S., Bakran Petricioli, T., Barešić, J., & Horvatić, D. (2021). Lithophyllum rims as biological markers for constraining palaeoseismic events and relative sea level variations during the last 3.3 ka on Lopud Island, southern Adriatic, Croatia. Global and Planetary Change, 202, 103517. https://doi.org/10.1016/j.gloplacha.2021.103517

Faivre, S., Bakran-Petricioli, T., Kaniewski, D., Marriner, N., Tomljenović, B., Sečanj, M., ... & Drysdale, R. N. (2023). Driving processes of relative sea-level change in the Adriatic during the past two millennia: From local tectonic movements in the Dubrovnik archipelago (Jakljan and Šipan islands) to global mean sea level contributions (Central Mediterranean). Global and Planetary Change, 227, 104158.

Faivre, S., Lončar, N., Tomljenović, B., Sečanj, M., Herak, M., & Barešić, J. (2024). High-resolution reconstruction of 4.5 ka relative sea-level changes and coseismic uplifts using algal rims and tidal notches from Dubrovnik epicentral area. In 7th Regional Scientific Meeting on Quaternary Geology November 14th–15th 2024, Zagreb, Croatia. Karst research and the 100th anniversary of the birth of Mirko Malez (pp. 79-80). Zagreb: Croatian Academy of Sciences and Arts.

Fais, S., Klingele, E. E., & Lecca, L. (1996). Oligo-Miocene half graben structure in Western Sardinian Shelf (western Mediterranean): Reflection seismic and aeromagnetic data comparison. Marine Geology, 133, 203–222. https://doi.org/10.1016/0025 3227(96)00030-8

Ferranti, L., Antonioli, F., Mauz, B., Amorosi, A., Dai Pra, G., Mastronuzzi, G., … Verrubbi, V. (2006). Markers of the last interglacial sea-level high stand along the coast of Italy: tectonic implications. Quaternary International, 145, 30–54.

García Artola, A., Cearreta, A., Leorri, E., Irabien, M.J., & Blake, W.H. (2009). Las marismas costeras como archivos geológicos de las variaciones recientes en el nivel marino. Geogaceta, 47(3–4), 109–112.

Gehrels, W.R., Marshall, W.A., Gehrels, M.J., Larsen, G., Kirby, J.R., Eiríksson, J., … Shimmield, T. (2006). Rapid sea-level rise in the North Atlantic Ocean since the first half of the nineteenth century. The Holocene, 16(7), 949–965. https://doi.org/10.1191/0959683606hl977rp

Goodwin, I.D., & Harvey, N. (2008). Subtropical sea-level history from coral microatolls in the Southern Cook Islands, since 300 AD. Marine Geology, 253(1–2), 14–25. https://doi.org/10.1016/j.margeo.2008.04.006

Grant, K.M., Rohling, E.J., Bar-Matthews, M., Ayalon, A., Medina-Elizalde, M., Ramsey, C.B., … Roberts, A.P. (2012). Rapid coupling between ice volume and polar temperature over the past 150,000 years. Nature, 491(7426), 744–747. https://doi.org/10.1038/nature11593

Gregory, J.M., Lowe, J.A., & Tett, S.F.B. (2006). Simulated global mean sea level changes over the last half millennium. Journal of Climate, 19(18), 4576–4591. https://doi.org/10.1175/JCLI3891.1

Guérin, G., Mercier, N. and Adamiec, G., 2011. Dose-rate conversion factors: update. Ancient TL, 29(1), pp.5-8. https://doi.org/10.26034/la.atl.2011.443

Gueguen, E., Doglioni, C. and Fernandez, M., 1998. On the post-25 Ma geodynamic evolution of the western Mediterranean. *Tectonophysics*, *298*(1-3), pp.259-269.

Heaton, T.J., Köhler, P., Butzin, M., Bard, E., Reimer, R.W., Austin, W.E., … Skinner, L.C. (2020). Marine20—The marine radiocarbon age calibration curve (0–55,000 cal BP). Radiocarbon, 62(4), 779–820. https://doi.org/10.1017/RDC.2020.68

Holzhauser, H., Magny, M., & Zumbühl, H.J. (2005). Glacier and lake level variations in west central Europe over the last 3500 years. The Holocene, 15(6), 789–801. https://doi.org/10.1191/0959683605hl853ra

Huntley, D.J. and Baril, M.R., 1997. The K content of the K-feldspars being measured in optical dating or in thermoluminescence dating. Ancient TL, 15(1), pp.11-13. https://doi.org/10.26034/la.atl.1997.271

Isla, M.F., Coronel, M.D., Schwarz, E. and Veiga, G.D., 2020. Depositional architecture of a wave-dominated clastic shoreline (Pilmatué Member, Argentina): Linking dynamics and stratigraphic record of bar-trough systems. Marine and Petroleum Geology, 118, p.104417. https://doi.org/10.1016/j.marpetgeo.2020.104417

Jevrejeva, S., Moore, J.C., Grinsted, A., & Woodworth, P.L. (2008). Recent global sea-level acceleration started over 200 years ago? Geophysical Research Letters, 35(8), L08715. https://doi.org/10.1029/2008GL033611

Kemp, A.C., Horton, B.P., Donnelly, J.P., Mann, M.E., Vermeer, M., & Rahmstorf, S. (2011). Climate related sea-level variations over the past two millennia. PNAS, 108(27), 11017–11022. https://doi.org/10.1073/pnas.1015619108

Kopp, R.E., Simons, F.J., Mitrovica, J.X., Maloof, A.C. and Oppenheimer, M., 2009. Probabilistic assessment of sea level during the last interglacial stage. Nature, 462(7275), pp.863-867. https://doi.org/10.1038/nature08686

Kopp, R.E., Kemp, A.C., Bittermann, K., Horton, B.P., Donnelly, J.P., Gehrels, W.R., … Rahmstorf, S. (2016). Temperature driven global sea level variability in the Common Era. PNAS, 113(11), E1434–E1441. https://doi.org/10.1073/pnas.1517056113

Laborel, J. (1983). Variations récentes du niveau marin à Port Cros (Var, France), mises en évidence par l'étude de la corniche littorale à Lithophyllum tortuosum. Comptes Rendus de l'Académie des Sciences, Série 2, 297, 157–160.

Laborel, J. (1987). Marine biogenic constructions in the Mediterranean. Scientific Reports, Port Cros National Park, 13, 97–126.

Laborel, J., & Laborel-Deguen, F. (1994). Biological indicators of relative sea level variations and of co-seismic displacements in the Mediterranean region. Journal of Coastal Research, pp. 395–415. https://www.jstor.org/stable/4298515

Laborel, J., & Laborel-Deguen, F. (1996). Biological indicators of Holocene sea level and climatic variations on rocky coasts of tropical and subtropical regions. Quaternary International, 31, 53–60.

Lambeck, K. (2004). Sea level change through the last glacial cycle: geophysical, glaciological and palaeogeographic consequences. Comptes Rendus Geoscience, 336(7–8), 677–689. https://doi.org/10.1016/j.crte.2004.05.001

Lambeck, K., Antonioli, F., Purcell, A. and Silenzi, S., 2004. Sea-level change along the Italian coast for the past 10,000 yr. Quaternary Science Reviews, 23(14-15), pp.1567-1598. https://doi.org/10.1016/j.quascirev.2004.02.009

Lambeck, K. and Purcell, A., 2005. Sea-level change in the Mediterranean Sea since the LGM: model predictions for tectonically stable areas. Quaternary Science Reviews, 24(18-19), pp.1969-1988. https://doi.org/10.1016/j.quascirev.2004.06.025

Lambeck, K., Antonioli, F., Anzidei, M., Ferranti, L., Leoni, G., Scicchitano, G., & Silenzi, S. (2011). Sea level change along the Italian coast during the Holocene and projections for the future. Quaternary International, 232(1–2), 250–257.

Leorri, E., Horton, B.P., & Cearreta, A. (2008). Development of a foraminifera based transfer function in the Basque marshes, N. Spain: implications for sea level studies in the Bay of Biscay. Marine Geology, 251(1–2), 60–74. https://doi.org/10.1016/j.margeo.2008.01.010

Lecca, L., 2000. La piattaforma continentale miocenico-quaternaria del margine occidentale sardo: blocco diagramma sezionato., 1, 70, 18 pp, 4 tavv.. Bologna. *Rendiconti Del Seminario Della Facoltà Di Scienze Dell'università Di Cagliari*, *70*, pp.49-70.

Longhitano, S.G. (2011). The record of tidal cycles in mixed silici-bioclastic deposits: examples from small Plio–Pleistocene peripheral basins of the microtidal Central Mediterranean Sea. Sedimentology, 58(3), 691–719. https://doi.org/10.1111/j.1365 3091.2010.01157.x

Lucchi, F., 2009. Late-Quaternary terraced marine deposits as tools for wide-scale correlation of unconformity-bounded units in the volcanic Aeolian archipelago (southern Italy). Sedimentary Geology, 216(3-4), pp.158-178. https://doi.org/10.1016/j.sedgeo.2009.03.003

Luterbacher, J., Werner, J.P., Smerdon, J.E., Fernández-Donado, L., González-Rouco, F.J., Barriopedro, D., … & Zerefos, C. (2016). European summer temperatures since Roman times. Environmental Research Letters, 11(2), 024001. https://doi.org/10.1088/1748 9326/11/2/024001

Malatesta, L.C., Finnegan, N.J., Huppert, K.L. and Carreño, E.I., 2022. The influence of rock uplift rate on the formation and preservation of individual marine terraces during multiple sea-level stands. Geology, 50(1), pp.101-105. https://doi.org/10.1130/G49245.1

Mann, M.E. (2002). Little Ice Age. In MacCracken, M.C., & Perry, J.S. (Eds.), The Earth System: Physical and Chemical Dimensions of Global Environmental Change, Vol. 1, pp. 504–509. Wiley, Chichester, UK.

Mannino, A.M. (2003). Morphology and composition of mineral deposits of Lithophyllum byssoides (Lamarck) Foslie (Corallinales, Rhodophyta) from the Island of Ustica. Plant Biosystems, 137(2), 203–213. https://doi.org/10.1080/11263500312331293817

Mariotti, A., Struglia, M.V., Zeng, N., & Lau, K.M. (2002). The hydrological cycle in the Mediterranean region and implications for the water budget of the Mediterranean Sea. Journal of Climate, 15(13), 1674–1690. https://doi.org/10.1175/1520 0442

Massari, F. and Parea, G.C., 1988. Progradational gravel beach sequences in a moderate-to high-energy, microtidal marine environment. Sedimentology, 35(6), pp.881-913. https://doi.org/10.1111/j.1365-3091.1988.tb01737.x

Morhange, C., Laborel-Deguen, F., Sartoretto, S., & Laborel, J. (1992). Recherches sur les bio-constructions à Lithophyllum lichenoides en Méditerranée occidentale. Méditerranée, 3(4), 67–71.

Muhs, D.R., Simmons, K.R., Schumann, R.R. and Halley, R.B., 2011. Sea-level history of the past two interglacial periods: new evidence from U-series dating of reef corals from south Florida. Quaternary Science Reviews, 30(5-6), pp.570-590. https://doi.org/10.1016/j.quascirev.2010.12.019

Muhs, D.R., 2022. MIS 5e sea-level history along the Pacific coast of North America. Earth System Science Data, 14(3), pp.1271-1330. https://doi.org/10.5194/essd-14-1271-2022

Murray, A.S., Helsted, L.M., Autzen, M., Jain, M. and Buylaert, J.P., 2018. Measurement of natural radioactivity: calibration and performance of a high-resolution gamma spectrometry facility. Radiation Measurements, 120, pp.215-220. https://doi.org/10.1016/j.radmeas.2018.04.006

Nalin, R., Massari, F., Zecchin, M., 2007. Superimposed Cycles of Composite Marine Terraces: The Example of Cutro Terrace (Calabria, Southern Italy). Journal of Sedimentary Research, 77(4), 340–354. https://doi.org/10.2110/jsr.2007.030

Nalin, R., Nelson, C.S., Basso, D. and Massari, F., 2008. Rhodolith-bearing limestones as transgressive marker beds: fossil and modern examples from North Island, New Zealand. Sedimentology, 55, 249-274. https://doi.org/10.1111/j.1365-3091.2007.00898.x

Nalin, R. and Massari, F., 2009. Facies and stratigraphic anatomy of a temperate carbonate sequence (Capo Colonna terrace, Late Pleistocene, southern Italy). Journal of Sedimentary Research, 79(4), pp.210-225.

Onac, B. P., Mitrovica, J. X., Ginés, J., Asmerom, Y., Polyak, V. J., Tuccimei, P., ... & Villa, I. M. (2022). Exceptionally stable preindustrial sea level inferred from the western Mediterranean Sea. Science Advances, 8(26), eabm6185.

Ortlieb, L., Zazo, C., Goy, J.L., Dabrio, C. and Macharé, J., 1996. Pampa del Palo: an anomalous composite marine terrace on the uprising coast of southern Peru. Journal of South American Earth Sciences, 9(5-6), pp.367-379. https://doi.org/10.1016/S0895-9811(96)00020-X

Pascucci, V., Martini, I.P. and Endres, A.L., 2009. Facies and ground-penetrating radar characteristics of coarse-grained beach deposits of the uppermost Pleistocene glacial lake Algonquin, Ontario, Canada. Sedimentology, 56(2), pp.529-545.

Pascucci, V., Sechi, D. and Andreucci, S., 2014. Middle Pleistocene to Holocene coastal evolution of NW Sardinia (Mediterranean Sea, Italy). Quaternary International, 328, pp.3-20.

Pascucci, V., De Falco, G., Del Vais, C., Melis, R.T., Sanna, I., & Andreucci, S. (2018). Climate changes and human impact on the Mistras coastal barrier system (W Sardinia, Italy). Marine Geology, 395, 271–284. https://doi.org/10.1016/j.margeo.2017.12.005

Pascucci, V., Frulio, G., & Andreucci, S. (2019). New estimation of the post Little Ice Age relative sea level rise. Geosciences, 9(8), 348. https://doi.org/10.3390/geosciences9080348

Peltier, W.R. (1996). Mantle viscosity and ice age ice sheet topography. Science, 273(5280), 1359–1364. https://doi.org/10.1126/science.273.5280.1359

Peltier, W.R. (2004). Global glacial isostasy and the surface of the ice age Earth: the ICE-5G (VM2) model and GRACE. Annual Review of Earth and Planetary Sciences, 32, 111–149. https://doi.org/10.1146/annurev.earth.32.082503.144359

Peltier, W.R., Argus, D.F., & Drummond, R. (2015). Space geodesy constrains ice age terminal deglaciation: The global ICE-6G_C (VM5a) model. Journal of Geophysical Research: Solid Earth, 120(1), 450–487. https://doi.org/10.1002/2014JB011176

Pérez, J.M., & Picard, J. (1964). Nouveau manuel de bionomie benthique. Recueil des Travaux de la Station Marine d'Endoume, 31(47), 5–137.

Perry, C.A., & Hsu, K.J. (2000). Geophysical, archaeological, and historical evidence support a solar output model for climate change. Proceedings of the National Academy of Sciences USA, 97(23), 12433–12438. https://doi.org/10.1073/pnas.220450497

Postma, G. and Nemec, W., 1990. Regressive and transgressive sequences in a raised Holocene gravelly beach, southwestern Crete. Sedimentology, 37(5), pp.907-920. https://doi.org/10.1111/j.1365-3091.1990.tb01833.x

Pourmand, A. and Dauphas, N., 2010. Distribution coefficients of 60 elements on TODGA resin: application to Ca, Lu, Hf, U and Th isotope geochemistry. Talanta, 81(3), pp.741-753. https://doi.org/10.1016/j.talanta.2010.01.008

Pourmand, A., Prospero, J.M. and Sharifi, A., 2014. Geochemical fingerprinting of trans-Atlantic African dust based on radiogenic Sr-Nd-Hf isotopes and rare earth element anomalies. Geology, 42(8), pp.675-678. https://doi.org/10.1130/G35624.1

Prescott, J.R. and Hutton, J.T., 1994. Cosmic ray contributions to dose rates for luminescence and ESR dating: large depths and long-term time variations. Radiation Measurements, 23(2-3), pp.497-500. https://doi.org/10.1016/1350-4487(94)90086-8

Rahmstorf, S. (2007). A semi-empirical approach to projecting future sea level rise. Science, 315(5810), 368–370. https://doi.org/10.1126/science.1135456

Reimann, T. and Tsukamoto, S., 2012. Dating the recent past (< 500 years) by post-IR IRSL feldspar–Examples from the North Sea and Baltic Sea coast. Quaternary Geochronology, 10, pp.180-187. https://doi.org/10.1016/j.quageo.2012.04.011

Roberts, K.G., Gloy, B.A., Joseph, S., Scott, N.R., & Lehmann, J. (2010). Life cycle assessment of biochar systems: estimating the energetic, economic, and climate change potential. Environmental Science & Technology, 44(2), 827–833. https://doi.org/10.1021/es902728z

Robertson, J., 2021. Investigation of the deformation rates implied by marine terraces to determine fault slip rates over multiple seismic cycles (Doctoral dissertation, Birkbeck, University of London). https://doi.org/10.18743/PUB.00045972

Rovere, A., Raymo, M.E., Vacchi, M., Lorscheid, T., Stocchi, P., Gomez-Pujol, L., Harris, D.L., Casella, E., O'Leary, M.J. and Hearty, P.J., 2016. The analysis of Last Interglacial (MIS 5e) relative sea-level indicators: Reconstructing sea-level in a warmer world. Earth-Science Reviews, 159, pp.404-427. https://doi.org/10.1016/j.earscirev.2016.06.006

Rovere, A., Stocchi, P. and Vacchi, M., 2016. Eustatic and relative sea level changes. Current Climate Change Reports, 2(4), pp.221-231. DOI 10.1007/s40641-016-0045-7

Rovida, A., Antonucci, A. and Locati, M., 2022. The European preinstrumental earthquake catalogue EPICA, the 1000–1899 catalogue for the European Seismic Hazard Model 2020. Earth System Science Data, 14(12), pp.5213-5231. https://doi.org/10.5194/essd-14-5213-2022

Sechi, D., Andreucci, S. and Pascucci, V., 2013. High energy beaches system developing during MIS 5c high sea-stand (100 Ka), north-west Sardinia, Italy. Journal of Mediterranean Earth Sciences, 5, pp.133-136. https://doi.org/10.1111/j.1365-3091.2008.00984.x

Sechi, D., Andreucci, S. and Pascucci, V., 2018. Intertidal Upper Pleistocene algal build-ups (Trottoir) of NW Sardinia (Italy): A tool for past sea level reconstruction. Journal of Mediterranean Earth Sciences, 10, pp.167-171. doi: 10.3304/JMES.2018.009

Sechi, D., Andreucci, S., Stevens, T. and Pascucci, V., 2020. Age and significance of late Pleistocene Lithophyllum byssoides intertidal algal ridge, NW Sardinia, Italy. Sedimentary Geology, 400, p.105618. https://doi.org/10.1016/j.sedgeo.2020.105618

Sechi, D., Andreucci, S., Cocco, F. and Pascucci, V., 2023. Stratigraphy and chronology of the Cala Mosca site, SW Sardinia (Italy). Quaternary Research, 112, pp.160-179. https://doi.org/10.1017/qua.2022.45

Serpelloni, E., Vannucci, G., Pondrelli, S., Argnani, A., Casula, G., Anzidei, M., Baldi, P. and Gasperini, P., 2007. Kinematics of the Western Africa-Eurasia plate boundary from focal mechanisms and GPS data. Geophysical Journal International, 169(3), pp.1180-1200. https://doi.org/10.1111/j.1365-246X.2007.03367.x

Shennan, I., & Horton, B.P. (2002). Holocene land and sea level changes in Great Britain. Journal of Quaternary Science, 17(5–6), 511–526. https://doi.org/10.1002/jqs.698

Sigl, M., Winstrup, M., McConnell, J.R., Welten, K.C., Plunkett, G., Ludlow, F., … & Woodruff, T.E. (2015). Timing and climate forcing of volcanic eruptions for the past 2,500 years. Nature, 523(7562), 543–549. https://doi.org/10.1038/nature14565

Spada, G., & Melini, D. (2022). New estimates of ongoing sea level change and land movements caused by Glacial Isostatic Adjustment in the Mediterranean region. Geophysical Journal International, 229(2), 984–998. https://doi.org/10.1093/gji/ggac325

Spratt, R.M. and Lisiecki, L.E., 2016. A Late Pleistocene sea level stack. Climate of the Past, 12(4), pp.1079-1092. https://doi.org/10.5194/cp-12-1079-2016

Stocchi, P., Vacchi, M., Lorscheid, T., De Boer, B., Simms, A.R., Van De Wal, R.S., Vermeersen, B.L., Pappalardo, M. and Rovere, A., 2018. MIS 5e relative sea-level changes in the Mediterranean Sea: Contribution of isostatic disequilibrium. Quaternary Science Reviews, 185, pp.122-134. https://doi.org/10.1016/j.quascirev.2018.01.004

Stranne, C., Jakobsson, M., & Björk, G. (2014). Arctic Ocean perennial sea ice breakdown during the Early Holocene Insolation Maximum. Quaternary Science Reviews, 92, 123–132. https://doi.org/10.1016/j.quascirev.2014.04.013

Tamura, T., Okazaki, H., Naya, T., Nakashima, R., Nakazato, H., Seike, K. and Okuno, J., 2022. Luminescence chronology for identifying depositional sequences in an uplifted coast since the Middle Pleistocene, eastern Japan. Frontiers in Earth Science, 10, p.967572. https://doi.org/10.3389/feart.2022.967572

Thiel, C., Buylaert, J.P., Murray, A., Terhorst, B., Hofer, I., Tsukamoto, S. and Frechen, M., 2011. Luminescence dating of the Stratzing loess profile (Austria)–Testing the potential of an elevated temperature post-IR IRSL protocol. Quaternary International, 234(1-2), pp.23-31. https://doi.org/10.1016/j.quaint.2010.05.018

Thiel, C., Tsukamoto, S., Tokuyasu, K., Buylaert, J.P., Murray, A.S., Tanaka, K. and Shirai, M., 2015. Testing the application of quartz and feldspar luminescence dating to MIS 5 Japanese marine deposits. Quaternary Geochronology, 29, pp.16-29. https://doi.org/10.1016/j.quageo.2015.05.008

Thomsen, K.J., Murray, A.S., Jain, M. and Bøtter-Jensen, L., 2008. Laboratory fading rates of various luminescence signals from feldspar-rich sediment extracts. Radiation Measurements, 43(9-10), pp.1474-1486. https://doi.org/10.1016/j.radmeas.2008.06.002

Vacchi, M., Marriner, N., Morhange, C., Spada, G., Fontana, A. and Rovere, A., 2016. Multiproxy assessment of Holocene relative sea-level changes in the western Mediterranean: Sea-level variability and improvements in the definition of the isostatic signal. Earth-Science Reviews, 155, pp.172-197.

Vacchi, M., Ghilardi, M., Melis, R.T., Spada, G., Giaime, M., Marriner, N., Lorscheid, T., Morhange, C., Burjachs, F. and Rovere, A., 2018. New relative sea-level insights into the isostatic history of the Western Mediterranean. Quaternary Science Reviews, 201, pp.396-408. https://doi.org/10.1016/j.quascirev.2018.10.025

Vacchi, M., Joyse, K.M., Kopp, R.E., Marriner, N., Kaniewski, D., & Rovere, A. (2021). Climate pacing of millennial sea level change variability in the central and western Mediterranean. Nature Communications, 12, 4013. https://doi.org/10.1038/s41467-021-24392-1

Vacchi, M., Gatti, G., Kulling, B., Morhange, C., & Marriner, N. (2022). Climatic control on the formation of marine notches in microtidal settings: new data from the northwestern Mediterranean Sea. Marine Geology, 453, 106929. https://doi.org/10.1016/j.margeo.2022.106929

Vasiliev, I., Jiménez-Moreno, G., Sierro, F.J. & Andrič, M. (2017). Timing of the Mediterranean isolation and the Messinian salinity crisis onset constrained by multiple geochemical proxies. Earth-Science Reviews, 172, 1–18.

Waelbroeck, C., Labeyrie, L., Michel, E., Duplessy, J.C., McManus, J.F., Lambeck, K., Balbon, E. and Labracherie, M., 2002. Sea-level and deep water temperature changes derived from benthic foraminifera isotopic records. Quaternary Science Reviews, 21(1-3), pp.295-305. https://doi.org/10.1016/S0277-3791(01)00101-9

Walker, J.S., Kopp, R.E., Little, C.M., & Horton, B.P. (2022). Timing of emergence of modern rates of sea level rise by 1863. Nature Communications, 13, 28564. https://doi.org/10.1038/s41467-022-28564-6

Wanner, H., Pfister, C., & Neukom, R. (2022). The variable European Little Ice Age. Quaternary Science Reviews, 287, 107531. https://doi.org/10.1016/j.quascirev.2022.107531

Woelkerling, W.J. (1983). A taxonomic reassessment of Lithophyllum (Corallinaceae, Rhodophyta) based on studies of R.A. Philippi's original collections. British Phycological Journal, 18(3), 299–327. https://doi.org/10.1080/00071618300650341

Woelkerling, W.J., Irvine, L.M., & Harvey, A.S. (1993). Growth-forms in nongeniculate coralline red algae (Corallinales, Rhodophyta). Australian Systematic Botany, 6, 277–293. https://doi.org/10.1071/SB9930277

Zecchin, M., Nalin, R. and Roda, C., 2004. Raised Pleistocene marine terraces of the Crotone peninsula (Calabria, southern Italy): facies analysis and organization of their deposits. Sedimentary Geology, 172(1-2), pp.165-185. https://doi.org/10.1016/j.sedgeo.2004.08.003

Zecchin, M., Ceramicola, S., Gordini, E., Deponte, M. and Critelli, S., 2011. Cliff overstep model and variability in the geometry of transgressive erosional surfaces in high-gradient shelves: the case of the Ionian-Calabrian margin (southern Italy). Marine Geology, 281(1-4), pp.43-58. https://doi.org/10.1016/j.margeo.2011.02.003

Zecchin, M., Catuneanu, O. and Caffau, M., 2019. Wave-ravinement surfaces: Classification and key characteristics. Earth-Science Reviews, 188, pp.210-239. https://doi.org/10.1016/j.earscirev.2018.11.011

Zucca, C., Andreucci, S., Akşit, I., Koca, Y.K., Madrau, S., Pascucci, V., Previtali, F., Shaddad, S.M., & Kapur, S. (2014). Buried palaeosols of NW Sardinia (Italy) as archives of Late Quaternary climatic fluctuations. Catena, 122, 72–90. https://doi.org/10.1016/j.catena.2014.06.005

Zucca, C., Sechi, D., Andreucci, S., Shaddad, S.M., Deroma, M., Madrau, S., Previtali, F., Pascucci, V. and Kapur, S., 2014. Pedogenic and palaeoclimatic evidence from an Eemian calcrete in north-western Sardinia (Italy). European Journal of Soil Science, 65(4), pp.420-435. https://doi.org/10.1111/ejss.12144

Appendices

Appendix A – Supplementary material for chapter 1

Sample	GS	Depth	WC	U	Th	K	α-Dr*	β-Dr*	γ-Dr*	k-int Dr	Cosmic Dr	Total Dr
	µm	(cm)	(%)	(ppm)	(ppm)	(%)	(Gy/ka)	(Gy/ka)	(Gy/ka)	(Gy/ka)	(Gy/ka)	(Gy/ka)
PX1	212-250	280	6.7 ± 0.3	1.0 ± 0.06	0.7 ± 0.13	1.2 ± 0.07	0.15 ± 0.05	0.50 ± 0.02	0.36 ± 0.00	0.95 ± 0.12	0.14 ± 0.01	2.07 ± 0.06
PX2	212-250	180	11.9 ± 0.5	0.8 ± 0.05	#NUM!	0.8 ± 0.07	0.15 ± 0.05	0.26 ± 0.02	0.23 ± 0.00	0.95 ± 0.12	0.16 ± 0.02	1.71 ± 0.08
NOR1	90-180	200	5.6 ± 0.2	1.7 ± 0.16	1.3 ± 0.20	3.6 ± 0.12	0.15 ± 0.05	2.10 ± 0.02	0.95 ± 0.01	0.56 ± 0.08	0.15 ± 0.02	3.86 ± 0.03
NOR3	125-180	2	6.6 ± 0.3	1.4 ± 0.11	0.9 ± 0.17	2.4 ± 0.10	0.15 ± 0.05	1.23 ± 0.02	0.67 ± 0.00	0.63 ± 0.09	0.21 ± 0.02	2.83 ± 0.04
TFX1	212-250	40	6.5 ± 0.3	2.5 ± 0.34	1.9 ± 0.30	3.2 ± 0.18	0.15 ± 0.05	1.65 ± 0.02	0.96 ± 0.01	0.95 ± 0.12	0.20 ± 0.02	3.84 ± 0.03
TFX2	212-250	90	10.0 ± 0.4	2.3 ± 0.29	2.1 ± 0.28	5.9 ± 0.19	0.15 ± 0.05	3.32 ± 0.02	1.53 ± 0.01	0.95 ± 0.12	0.18 ± 0.02	5.96 ± 0.02

Table SM1. Summary of dry and total dose rate. The concentration of Uranium (U) and Thorium (Th) Potassium (K) estimated using different methods high-resolution gamma spectrometer (HRGS), beta counter (GMBC) and ICP-MS. Grainsize of the measured sample (GS), estimated water content (WC) uncertainty of 4% is considered, estimated dry dose rate (*), averaged concentration of element used to estimate dry dose rate with GMBC (avg). In line with the text in bold, the element concentrations used, and the final dose rate used for dating.

Representative pIRIR225 decay signal and dose–response growth curve used for equivalent dose (De) determination in sample PX1 and PX2 (Piscinnì area).

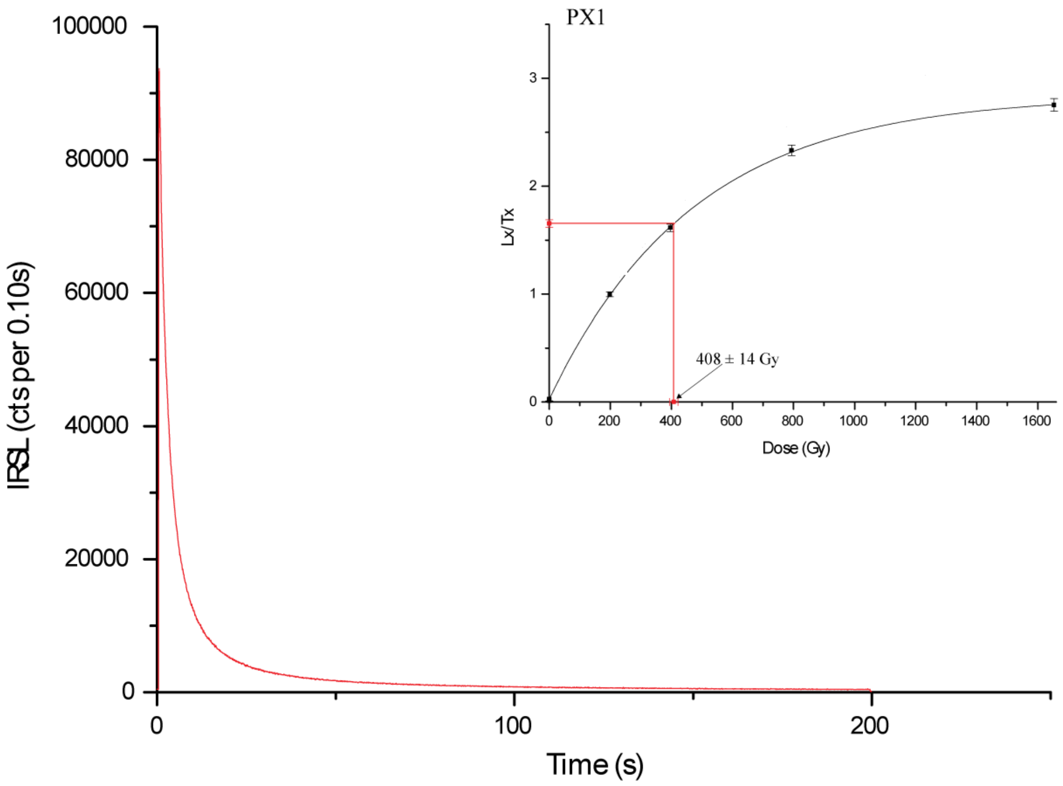

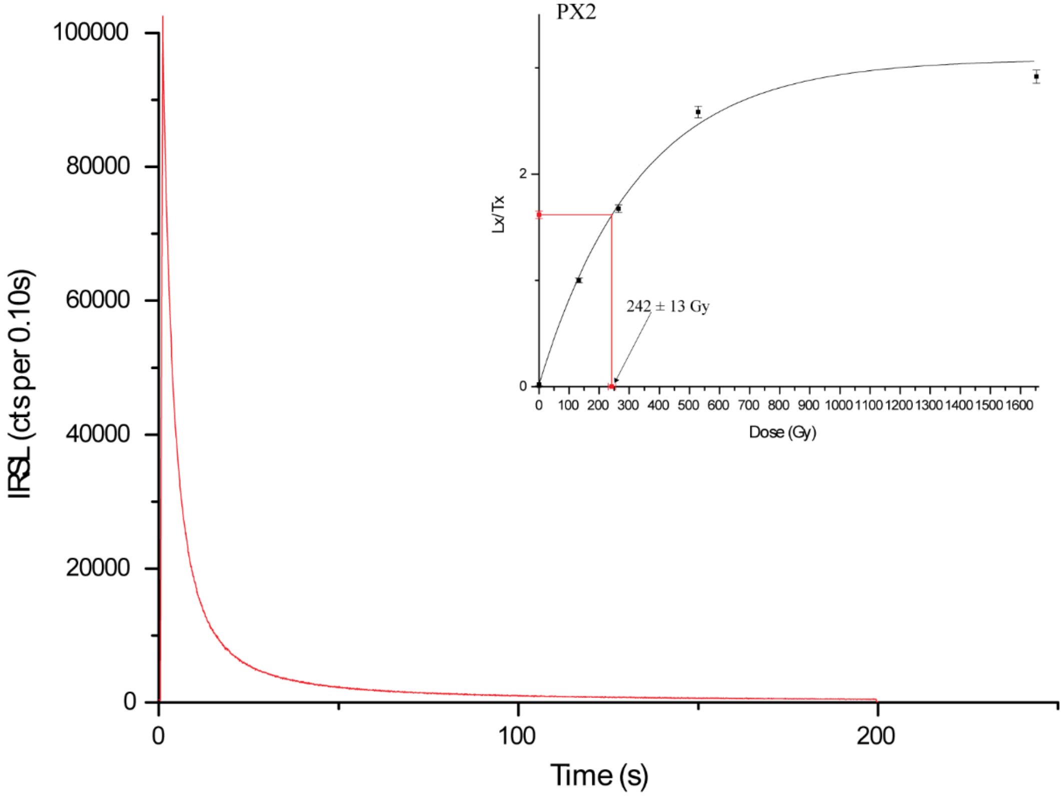

Representative pIRIR225 decay signal and dose–response growth curve used for equivalent dose (De) determination in sample NOR1 and NOR3 (Nora area).

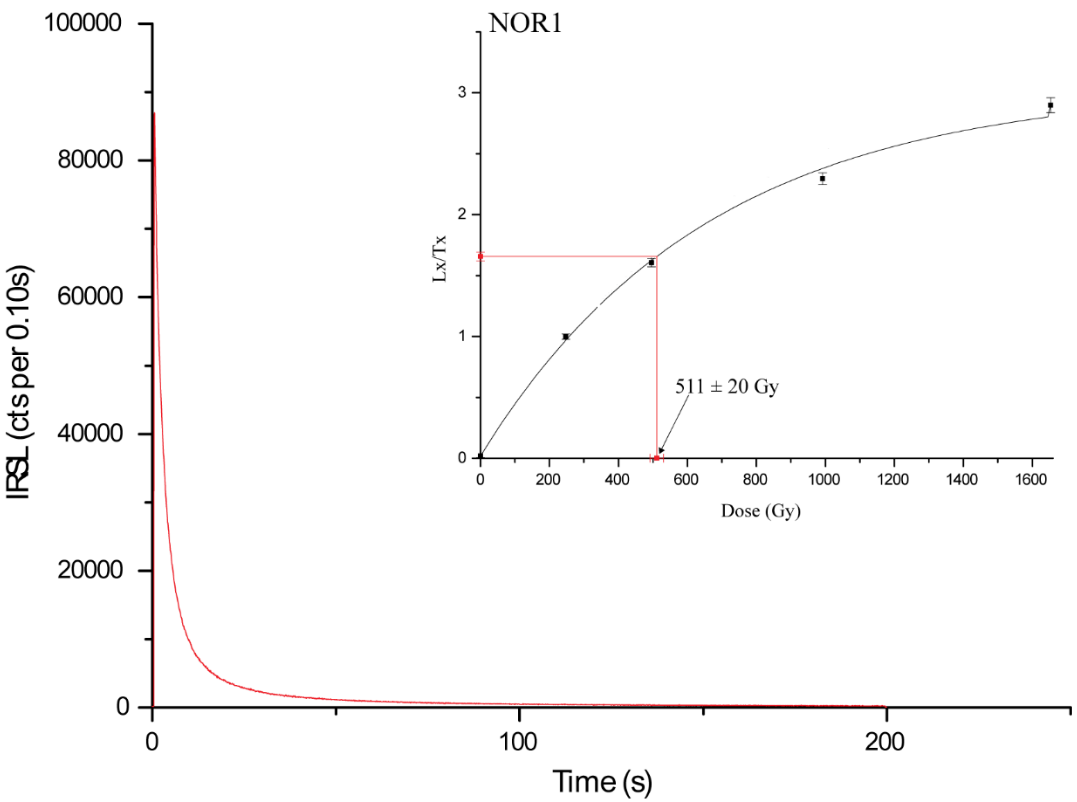

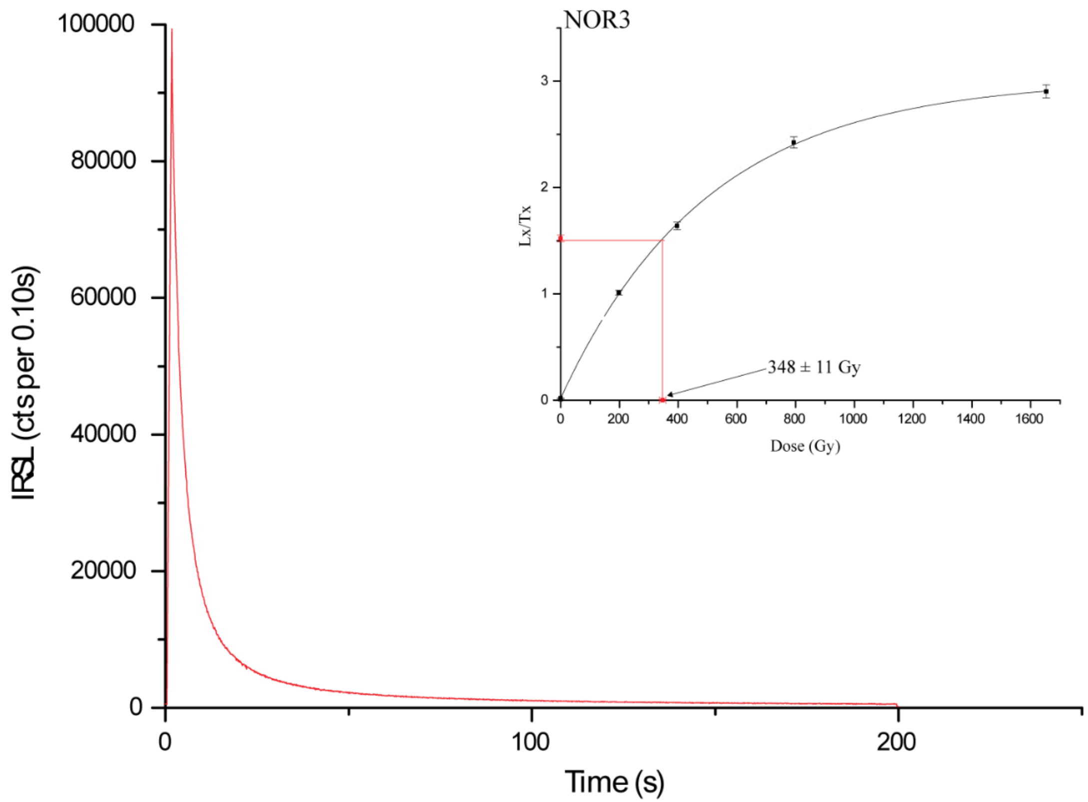

Representative pIRIR225 decay signal and dose–response growth curve used for equivalent dose (De) determination in sample TFX1 and TFX2 (Torre Foxi area).

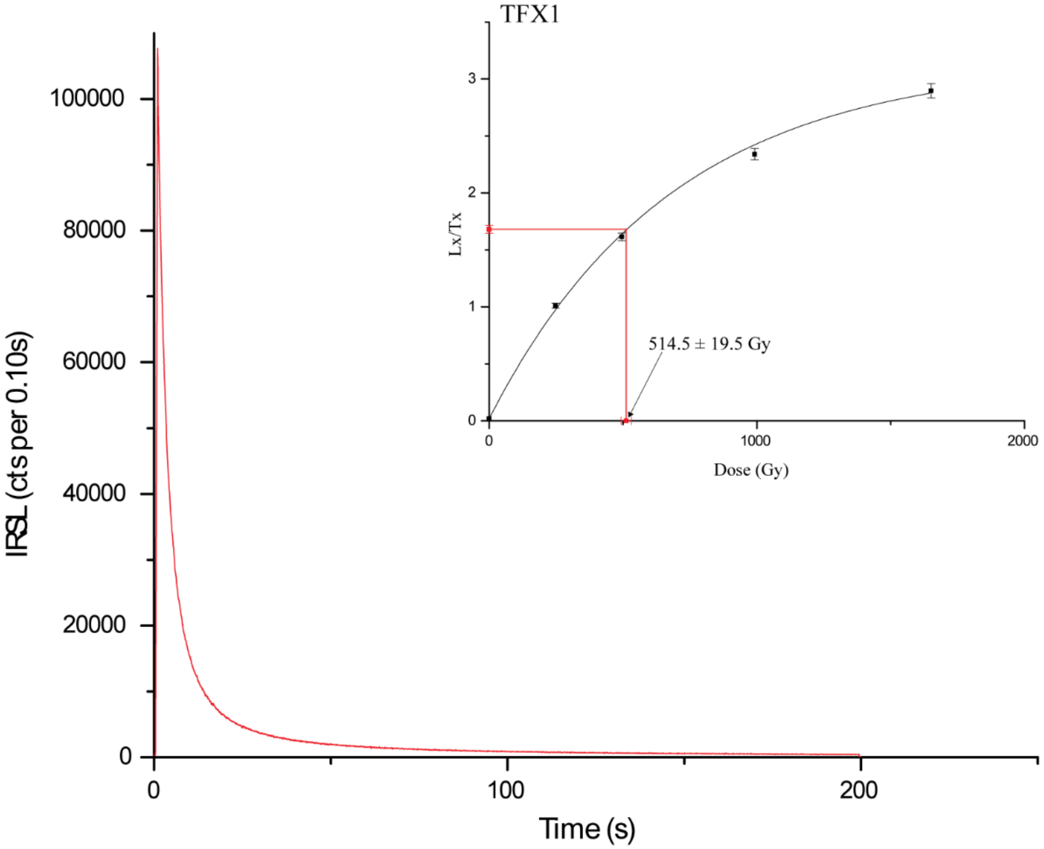

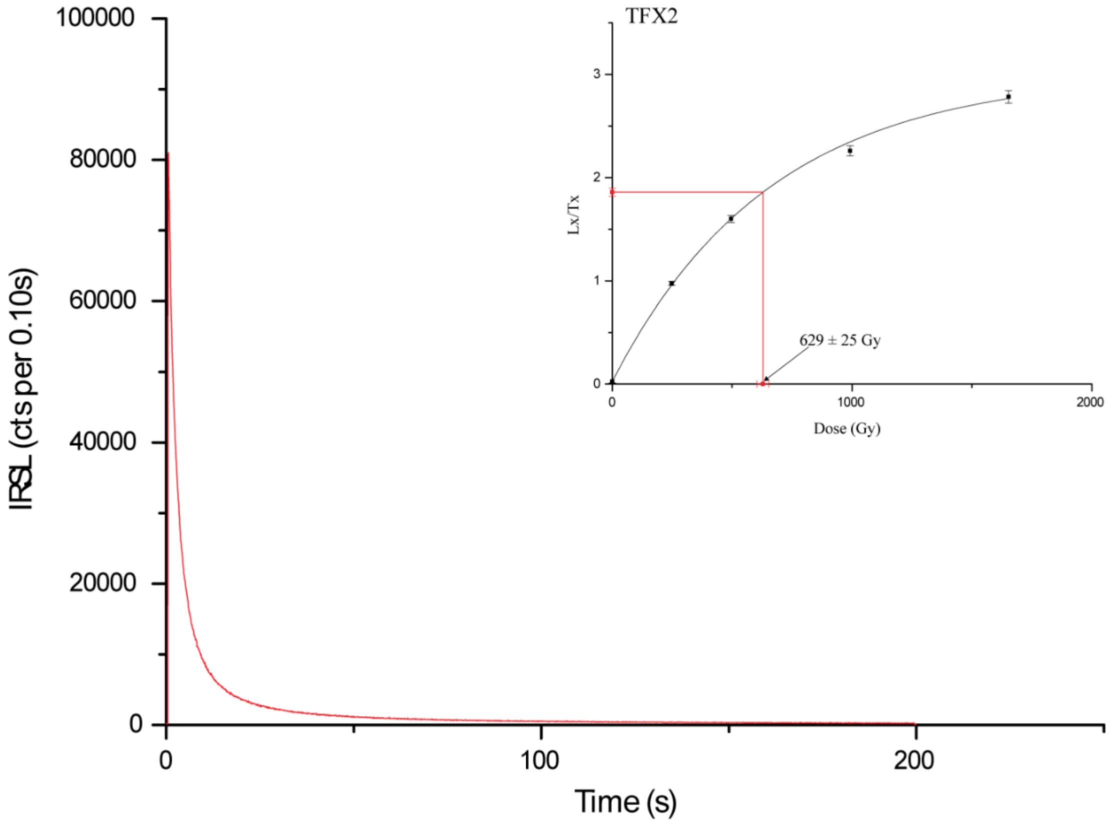

Table SM2. Indicative range parameters of the identified facies and corresponding relative sea-level (RSL) estimates for the dated samples

Site	Unit	Facies code	Environment (marker type)	E_m	Ee_m	Ul_m	Ll_m	RWL_m	IR_m	RSL_m	dRSL_m	GIA_m	dGIA_m	ESL_m	dESL_m	PD_m	dPD_m	Age_ka	dAge_ka	PDr_mm_per_yr	dPDr_mm_per_yr	MIS
Piscinnì	U1	Sdt	Upper-shoreface (sand, gravel)	1	0.2	-1	-4	-2.5	3	3.5	1.513275	0	2	-10	7	13.5	7.435725	193	14	6.99482E-05	3.88598E-05	7a
Piscinnì	U3a	Seu	Foreshore (Sandstone)	1.4	0.2	2	-0.5	0.75	2.5	0.65	1.265899	0	2	6	3	-5.35	3.821322	135	11	-3.96296E-05	2.84897E-05	5e
Nora	U3a	Sdt	Upper-shoreface (sand, gravel)	0.8	0.2	-1	-6	-3.5	5	4.3	2.507987	0	2	6	3	-1.7	4.392038	127	5	-1.33858E-05	3.4587E-05	5e
Nora	U3a	Sdt	Upper-shoreface (sand, gravel)	1.5	0.2	-1	-6	-3.5	5	5	2.507987	0	2	6	3	-1	4.392038	143	7	-6.99301E-06	3.07155E-05	5e
Torre Foxi	U3a	Bef	Upper-shoreface / reef-proximal	1	0.2	-2	-6	-4	4	5	2.009975	0	2	6	3	-1	4.127953	135	5	-7.40741E-06	3.05787E-05	5e
Torre Foxi	U3a	Bef	Upper-shoreface / reef-proximal	0.4	0.2	-2	-6	-4	4	4.4	2.009975	0	2	6	3	-1.6	4.127953	135	6	-1.18519E-05	3.0582E-05	5e
Torre Foxi	U3b	Gci	Foreshore (gravel, sand)	2	0.2	2	-0.5	0.75	2.5	1.25	1.265899	0	2	-9	6	10.25	6.45	103	3	9.95146E-05	6.26884E-05	5c

Appendix B – Supplementary material for chapter 3

Sample	Lab code	Selected Material	Conventional ^{14}C age (BP)	±1σ (BP)	Calibrated age (68.2%) cal AD	Calibrated age (95.4%) cal AD
N1	Beta-669808	*L. byssoides* thallus	620	30	1613-1790	1520 - 1851
N3	Beta-669809	*L. byssoides* thallus	610	30	1626-1800	1527 - 1864
N9	Beta-669812	*L. byssoides* thallus	570	30	1660-1820	1570 - 1916
N10	Beta-705827	*L. byssoides* thallus	360	30	1896-1939	1862 - post 1950
N13	Beta-705829	*L. byssoides* thallus	280	30	1890-post 1950	1824 - post 1950
N14	Beta-669813	*L. byssoides* thallus	220	30	1898-post 1950	1836-post 1950
O1	Beta-705029	*L. byssoides* thallus	1340	30	972-1128	891 - 1197
O2	Beta-705034	*L. byssoides* thallus	1330	30	984-1141	900 - 1208
O7	Beta-705030	*L. byssoides* thallus	650	30	1549-1714	1499 - 1815
O11	Beta-705031	*L. byssoides* thallus	650	30	1548-1715	1499 - 1815
O16	Beta-705032	*L. byssoides* thallus	600	30	1637-1804	1537 - 1874
O20	Beta-705033	*L. byssoides* thallus	440	30	1818-post 1950	1715 - post 1950

Table SM1. *Radiocarbon dating results obtained from Beta Analytic for samples used to derive sea-level index points (SLIPs). Conventional radiocarbon ages are reported with analytical uncertainty (±1σ). Calibration was performed using the MARINE20 calibration curve with local ΔR correction, applying the High Probability Density (HPD) method. Calibrated ages are reported as 68.2% and 95.4% probability ranges.*

The dataset includes field data (GPS coordinates and elevations), thin-section positions and images, photographs of the complete samples, and the processed files used to generate the figures and tables presented in the manuscript. **These data are available at Mendeley Data: Fantini, Giovanni; Andreucci, Stefano; Sechi, Daniele; Pascucci, Vincenzo (2026), "Fantini et al., 2026", Mendeley Data, V2, doi:10.17632/8jwfmfp2cy.2.**

Logos for NRRP scholarship under Mission 4 “Education and Research” - Component 2 “From Research to Business” - Investments 1.3, 1.4, 1.5, 3.1:

PhD students receiving a NRRP scholarship under Mission 4 “Education and Research” - Component 2 “From Research to Business” - Investments 1.3, 1.4, 1.5, 3.1. This thesis was produced by GF while attending the PhD programme in Earth and Environmental Sciences and Technologies at the University of Cagliari, Cycle XXXVIII, with the support of a scholarship financed by NRRP, funded by the European Union - NextGenerationEU - Mission 4 "Education and Research", Component 2 “From Research to Business” – Investment 1.3 “Creation of “enlarged partnerships between universities, research centres, businesses and funding of basic research projects”.